FRACTURE ANALYSIS OF SPUN-CAST CONCRETE POLES USING THE PHASE-FIELD METHOD

A THESIS SUBMITTED TO
THE GRADUATE SCHOOL OF NATURAL AND APPLIED SCIENCES
OF
MIDDLE EAST TECHNICAL UNIVERSITY

BY

ALI AZIM AZARY

IN PARTIAL FULFILLMENT OF THE REQUIREMENTS
FOR
THE DEGREE OF MASTER OF SCIENCE
IN
CIVIL ENGINEERING

SEPTEMBER 2017

Approval of the thesis:

FRACTURE ANALYSIS OF SPUN-CAST CONCRETE POLES USING THE PHASE-FIELD METHOD

submitted by **ALI AZIM AZARY** in partial fulfillment of the requirements for the degree of **Master of Science in Civil Engineering Department, Middle East Technical University** by,

Prof. Dr. Gülbin Dural Ünver
Dean, Graduate School of **Natural and Applied Sciences** ________________

Prof. Dr. İsmail Özgür Yaman
Head of Department, **Civil Engineering** ________________

Assoc. Prof. Dr. Serdar Göktepe
Supervisor, **Civil Engineering Department, METU** ________________

Examining Committee Members:

Assoc. Prof. Dr. Ercan Gürses
Aerospace Engineering Department, METU ________________

Assoc. Prof. Dr. Serdar Göktepe
Civil Engineering Department, METU ________________

Assist. Prof. Dr. Onur Pekcan
Civil Engineering Department, METU ________________

Assist. Prof. Dr. Hüsnü Dal
Mechanical Engineering Department, METU ________________

Assist. Prof. Dr. Ali Javili
Mechanical Engineering Department, Bilkent University ________________

Date: ________________

I hereby declare that all information in this document has been obtained and presented in accordance with academic rules and ethical conduct. I also declare that, as required by these rules and conduct, I have fully cited and referenced all material and results that are not original to this work.

Name, Last Name: ALI AZIM AZARY

Signature :

ABSTRACT

FRACTURE ANALYSIS OF SPUN-CAST CONCRETE POLES USING THE PHASE-FIELD METHOD

Azim Azary, Ali
M.S., Department of Civil Engineering
Supervisor : Assoc. Prof. Dr. Serdar Göktepe

September 2017, 88 pages

Shrinkage is an important type of deformation in hardening concrete, which happens mainly in the cement paste and may cause significant damage if restrained. Spun-cast concrete poles are among structural members that are prone to this type of damage if not fabricated properly. They are used extensively in structures such as columns, piles, and utility poles to name a few. In this thesis, we study the differential shrinkage-induced cracking in spun-cast members computationally using the Phase Field Method within the framework of the Finite Element Method. The Phase Field Method is a thermodynamically based method that is often used to model phase changes and evolving microstructures in materials. The Phase Field Models based on variational formulation for fracture has become popular recently, and proven capable of accurately predicting complex crack behavior in both two and three dimensions. The performance of the proposed approach to the differential shrinkage-induced cracking is demonstrated through the representative numerical examples.

Keywords: Phase-Field Method, Shrinkage-Induced Cracking, Spun-Cast Poles, Finite Element Method

ÖZ

FAZ ALANI YÖNTEMİ İLE MERKEZKAÇ DÖKÜMLÜ BETON DİREKLERDE ÇATLAK ANALİZİ

Azim Azary, Ali
Yüksek Lisans, İnşaat Mühendisliği Bölümü
Tez Yöneticisi : Doç. Dr. Serdar Göktepe

Eylül 2017 , 88 sayfa

Ağırlıklı olarak çimento hamurunda meydana gelen ve düzgün yayılı olmaması durumunda önemli hasara neden olabilen rötre, sertleşen betonda meydana gelen önemli bir şekil değiştirme türüdür. Merkezkaç dökümlü beton direkler uygun bir şekilde imal edilmedikleri takdirde bu tip hasara eğilimli yapısal üyeler arasında yer alabilirler. Merkezkaç döküm tekniği ile üretilen sütunlar, kazıklar enerji nakil ve aydınlatma direkleri yaygın olarak kullanılmaktadır. Bu tez çalışmasında merkezkaç dökümlü elemanlarda oluşan rötre çatlaklarının oluşumu ve yayılımı problemi Sonlu Elemanlar Yönteminin yapısı içerisinde Faz Alanı Yöntemi ile çalışılmıştır. Faz Alanı Yöntemi, faz değişimlerini ve malzemelerin mikroyapılarındaki kalıcı değişimleri modellemek için sıklıkla kullanılan termodinamik temelli bir yöntemdir. Varyasyonel formülasyona dayanan çatlak Faz Alanı Modelleri son zamanlarda kabul görmüş; bu yöntemlerin hem iki hem de üç boyutta karmaşık çatlama davranışlarının hassas benzeminde kullanılabilirliği kanıtlanmıştır. Bu çalışmada rötre çatlaklarının modellenmesi için geliştirilen yöntemin performansı ve uygulanabilirliği ilgili sayısal örneklerle gösterilmiştir.

Anahtar Kelimeler: Faz Alan Yöntemi, Rötre Çatlağı, Merkezkaç Dökümlü Direkler, Sonlu Elemanlar Yöntemi

ACKNOWLEDGMENTS

I would like to express my gratitude to my supervisor, Dr Göktepe, for his kind support, guidance, and also his patience during my studies at METU. I also thank the thesis committee members for taking the time to read my thesis, and for their constructive criticism and useful comments and suggestions.

TABLE OF CONTENTS

LIST OF TABLES

TABLES

LIST OF FIGURES

FIGURES

LIST OF SYMBOLS

$\boldsymbol{u}$	displacement vector
ε	strain tensor
$\boldsymbol{\sigma}$	stress tensor
$\boldsymbol{t}$	traction vector
ψ	free energy function
E	elasticity modulus
ν	Poisson's ratio
λ, μ	Lamé parameters
d	damage variable
l	length scale parameter
Γ	crack surface area
γ	crack surface density
∇	gradient operator
∇^2	Laplacian operator
ψ_0, ψ_0^+, ψ_0^-	free energy of intact material and its tensile and compressive parts
$g(d)$	degradation function
g_f	fracture energy
$\boldsymbol{b}$	body force vector
$\boldsymbol{n}$	unit normal on the boundary
a_1, a_2, a_3, p	degradation function parameters
w, w_c	crack opening and its ultimate value
k_0	initial slope of the softening law
f_c, f_t	compressive and tensile strengths
$\mathcal{H}$	energy history variable
χ	aging variable
ξ	degree of hydration
ε_{sh}	shrinkage strain

CHAPTER 1

INTRODUCTION

1.1 Motivation

Concrete is a widespread structural material that has diverse applications whether in residential and industrial buildings, or in infrastructures such as dams, pavements, bridges, and even in very sensitive structures like nuclear power plants. Therefore, a sound understanding of its behavior under different loading scenarios and conditions is of utmost importance. One critical stage for concrete is the early ages, which plays an important role in determining the performance of the structure for the rest of its service life. Early-age concrete undergoes hardening through the hydration of cement paste, which binds the aggregates together to make up a whole load-bearing structure. Many factors are involved in this process from the design phase like mix design, choice of aggregates and cement, to construction phase like pouring, compacting, and curing. These factors take part in the formation of microstructure and the deformations, stresses, and possible cracks that happen as a result. These can contribute negatively to later performance of concrete, especially the durability of concrete, which is of utmost importance. The durability can suffer from various causes of different nature. Instances of such causes can be the alkali-silica reaction, the frost action, the difference in thermal properties of aggregates and the cement paste, the chemical attack, the corrosion of reinforcement, and abrasion. One common critical factor is the permeability of concrete in most cases. Voids and cracks that give access to external agents and cause damage to concrete. One important phenomenon that characterizes concrete particularly at its early ages and hugely affects its durability is shrinkage. Shrinkage is one type of deformation that occurs in concrete over time, regardless of loading, temperature changes, or restraints. However the latter mentioned factors influence the shrinkage strains. It happens in the cement paste, and can be categorized in different types as plastic shrinkage, thermal shrinkage, chemical shrinkage, and drying shrinkage. Plastic shrinkage occurs in fresh concrete at very early ages if it is not cured properly. This results in plastic shrinkage of the surface layer due to loss of water leading to wrapping of the paste around reinforcing bars or aggregates in the surface layer, and can cause cracking. Thermal shrinkage happens as the heat of hydration dissipates and concrete starts to cool off. Chemical shrinkage or autogenous shrinkage is the shrinkage resulting from chemical reactions of hydration because of the volume difference of the products of the hydration. For practical reasons such as workability, usually more water is added to the mixture than the amount needed for the complete hydration of the cement. The excess water moves to the surface and evaporates later and as a result drying shrinkage happens [2, 3, 4, 5]. Since shrinkage strains are normally greater than failure strain of concrete in tension, it can result in cracking when the deformation is restrained. The restraints can be either external or internal. Internal restraint can be due to differential shrinkage, aggregates or reinforcement. Differential shrinkage, i.e. spatial gradients of shrinkage strains, can be due to the segregation of aggregates, or difference in the rate of drying or the dissipation of heat at different depths. The deformations and cracking due to shrinkage impact the function and durability of the structure and therefore are of great importance. There has been many works both experimental and computational on modeling shrinkage and cracking it may cause in the literature. However, due to complexity of the subject and the lack of reliable experimental and computational methods, each work tackled a specific problem and there exists a huge gap to be filled.

1.2 Shrinkage-Induced Cracking: Literature Overview

There exist both experimental and computational studies of cracking due to shrinkage in the literature. The studies are done usually with the aim of improving the standard test methods, enhancing the production methods, and finding the underlying reasons and phenomena that result in damage. Some works investigate the differential shrinkage and the possible damage it may cause. There can be various contributing factors to differential shrinkage. One such factor can be segregation, which can be due to improper compacting. Dilger et al. [1] studied segregation and differential shrinkage in utility poles from the field and also poles they produced in the laboratory and attempted to find a suitable mix design as well as a better production procedure so as to alleviate the problem. In a later study, Dilger and Rao [6] analyzed differential shrinkage in high-performance concrete mixtures to assess their strength, durability, and susceptibility to segregation. Another factor causing differential shrinkage can be moisture gradients due to nonuniform drying. Kim and Lee [7] studied this phenomenon and proposed an analytical method to predict the differential shrinkage due to moisture gradients in concrete. They showed that taking creep into account the predicted values using their proposed method demonstrates good agreement with experimental measurements. De Sa et al. [8] investigated the damage caused by differential drying shrinkage also taking into account the influence of time-dependent factors like creep. Idiart et al. [9] investigated the drying shrinkage and cracking by performing a coupled mechanical and diffusion analysis of mesoscale two-dimensional concrete models and analyzed the moisture distribution and the resulting damage. Briffaut and Benboudjema [10] conducted mesoscopic numerical analyses to study cracking due to differential drying. They also accounted for the effect of creep. Temperature gradients can be another factor that causes differential shrinkage, which becomes more pronounced in the case of massive concrete structures. To involve thermal shrinkage effects in large structures, Briffaut et al. [11] proposed a new ring test method in which the inside ring was heated to simulate the temperature rise. It can be said that the first and foremost important cause of differential shrinkage is external structural restraint in joints and supports. The restraints act along with other factors in intensifying the differential shrinkage. So, most studies are done on restrained shrinkage. Beushausen and Alexander [12] analyzed stress relaxation in concrete overlays undergoing shrinkage through different experiments with various substrate textures and overlay materials to analyze the differential shrinkage cause by restraining effect of the substrate. Ruiz-Ripoll [13] proposed an experimental methodology to evaluate cracking at early ages due to restrained shrinkage. They used square slabs restrained at four edges by a number of rods and put them in a wind tunnel for expediting moisture loss and then studied the cracking in the slabs. Korsun et al. [14] carried out experiments to analyze the size effect of large-scale concrete structures on differential shrinkage and stresses in high-strength concrete. Beushausen [15] investigated cracking of concrete overlays due to restrained shrinkage assessing different factors such as humidity, curing, strength, and thickness of the overlay layer. Tang et al. [16] studied cracking caused by shrinkage and its influence on moisture diffusion in concrete samples and concrete overlays using a coupled mechanical and diffusion analysis with mesoscopic models. Dey et al. [17] investigated the effect of wollastonite fibers in restrained cement paste on cracking and moisture loss and diffusion due to plastic shrinkage. In the study of restraint in cracking of concrete, ring tests are very common and many researches use ring tests or try to develop new ones for specific purposes. We mentioned before Briffaut et al. [11] developed a new ring test to take into account the thermal effects. Dong et al. [18] proposed a ring shrinkage test together with a numerical method to analyze the probability of cracking in restrained shrinkage. Bryne et al. [19] studied restrained shrinkage cracking of shotcrete linings using both ring and new slab tests, and analyzed the mitigating effect of glass fibers. Dong et al. [20] studied the effect of thickness of circular and elliptical concrete rings on cracking and the developed stresses. Differential shrinkage is not the only way in which shrinkage strains can cause damage. Local difference in strains caused due to restraining effect of aggregates also may result in cracking. This can be of critical importance if the difference between mechanical properties of aggregates and cement paste are large enough, or the distance between aggregates are significant due to poor aggregate gradation or insufficient aggregate content. The restraining effect of aggregates has also been studied extensively by various researchers. Liu et al. [21] studied shrinkage-induced cracking due to aggregate restraints numerically using Generalized Beam Lattice Model. Grassl et al. [22] studied the effect of aggregate size and content on shrinkage-induced microcracking due to aggregate restraints with two-dimentional mesoscale models using lattice-type modeling and the Finite Element Method. Idiart et al. [9] in a work mentioned before also investigated the effect of viscoelastic behavior of cement paste at early ages, and aggregate size and volume. Idiart et al. [23] performed a numerical analysis of microcracking in cementitious composites undergoing shrinkage due to aggregate restraint. Briffaut and Benboudjema [10] also studied the restraining effect of aggregates in their numerical mesoscale studies mentioned before. Maruyama and Sasano [24] studied cracking due to aggregate restraints as well as interface cracks due to stress arch formation.

They observed that the area of cracks increased with aggregate size and macroscopic strains. Malbois et al. [25] investigated the restraining effect of aggregates in cracking with experiments using samples of different aggregate sizes and volumes. Shin et al. [26] investigated the effect of aggregate stiffness and shrinkage on overall tensile behavior of concrete using mesoscale Finite Element Analyses. Lee et al. [27] studied drying shrinkage of concrete specimens using dune sand and crushed sand as fine aggregates. They tested different samples with changing water content, aggregate content and analyzed strength, cracking time, and shrinkage strains. Maruyama et al. [28] studied the effect of aggregate properties on shrinkage-induced cracking in specimens with different aggregates. They observed that the amount of strain incompatibility between the aggregates and paste, and also the strength of the Interfacial Transition Zone determine whether cracking is dominated by a more distributed microcracking or localized macro cracks. As it can be seen from the works listed here, shrinkage is an extremely complicated phenomenon with various aspects that usually act together with other phenomena rather than independently. Some aspects have been studied by far, some of which we tried to cover, however there are still many other aspects still remain untouched.

1.3 Computational Approaches to Fracture

In recent decades, the computational approaches to fracture have been a subject of great interest and a considerable progress has been made. The subject is covered in a quite comprehensive review article by Rabczuk [29]. The approach for modeling fracture can be broadly classified as either discrete or smeared. Discrete crack approaches need special techniques to incorporate sharp discontinuities into the Finite Element mesh. Earlier approaches were the so-called inter-element separation methods, in which the crack is supposed to grow along element edges [30, 31, 32]. A very popular method is the Extended Finite Element Method, which treats the discontinuity by adding the so-called enrichment functions to the existing finite element approximations with additional degrees of freedom. The enrichment functions include crack-tip asymptotic fields and a discontinuous function to account for the jump in the displacement field across the crack [33]. In general it can be said that discrete crack models incorporate the sharp discontinuities into the mesh either by remeshing or by using enrichment functions. However, these approaches have been proven to be cumbersome in complex crack patterns, especially in three-dimensional problems. On the other hand, the smeared crack models instead of treating cracks as sharp discontinuities, incorporate the effect of cracking, such as stress release or softening into the constitutive law. The softening behavior introduced into the model results in loss of well-posedness of the problem. In order to resolve this problem regularization techniques such as gradient-enhanced models [34] and nonlocal models [35] are used. Phase-Field fracture models can be considered as a subcategory of smeared models, however, they are based on the variational theory of fracture by Francfort and Marigo [36], which requires minimization of the energy. Classical fracture mechanics is generally based on the Griffith's theory [37]. It lacks the capability to model the crack initiation, curved crack paths, crack branching, and multiple crack patterns. On the other hand, the variational approach to fracture eliminates all the limitations that are encountered in the classical Griffith-type models.

One other approach that can be of interest in fracture is the meshless methods. Since these methods only have a distribution of nodes without element connectivity, it relieves the problem of incorporating cracks into the mesh to a degree, because there is almost no need for remeshing. There have been several works on application of meshless methods to fracture. Belytschko et al. [38] implemented the Element-Free Galerkin Method to both stationary and propagating crack problems. In a later work, Belytschko and Tabbara [39] extended the Element-Free Galerkin Method to dynamic fracture. Since the crack-tip fields showed oscillations due to singularity in an extension of the method Flemin et al. [40] added enrichment functions to interpolations. Rao and Rahman [41] proposed an efficient Element-Free Galerkin Method with new weight functions and accurate imposition of essential boundary conditions. In later works, they extended their model to nonlinear elastic fracture by adding enrichment functions [42, 43]. Brighenti [44] proposed an extension of the Element-Free Galerkin Method to three-dimensional fracture problems. Rabczuk et al. [45] proposed another extension for the method to three-dimensional nonlinear problems using local enrichments that is capable of predicting crack initiation and propagation for complex cracking with crack intersections. Hosseini-Toudeshky and

Musivand-Arzanfudi [46] proposed a modified Parametric Meshless Galerkin Method to improve efficiency and used it to calculate stress intensity factors. Liu et al. [47] proposed a new approach with the Meshless Local Petrov-Galerkin Method to model brittle fracture. With a continuum damage approach and treating the objects as rigid bodies, they modeled brittle fracture of objects into pieces without limitations like small time steps and a better resampling for high-stress regions that improves computational efficiency. Sagaresan [48] proposed a meshless discrete crack model with cracks as discrete segments. This allows for a simpler implementation that is capable of resolving multiple cracks. Using a Neo-Hookean constitutive model for the solid and a cohesive crack model they achieved results with good agreement with experimental ones. Yang et al. [49] proposed a Meshfree Adaptive Multiscale Method for Fracture. Using a Phantom Node Method for fracture at large scale and at fine scale a molecular approach, they implemented their model to two-dimensional problems and obtained good agreement with atomistic simulations.

Recently, the Phase-Field approach to fracture has gained considerable attention. It is a method to solve the problem of changing interfaces. It has been applied to many problems such as phase transition, microstructure evolution, solidification, and fracture. The boundary condition between phases is replaced with a partial differential equation for an order parameter. The value of the order parameter defines the state of the system. One formulation is achieved by writing the total free energy of the sytem in terms of the order parameter. Then, minimizing the energy, one obtains the evolution equation for the order parameter. Most phase-field models for fracture are obtained in this manner. Karma et al. [50] introduced a Phase-Field model for dynamic mode III fracture. Kuhn and Müller [51] proposed a Phase-Field model based on the variational approach to brittle fracture. Miehe et al. [52] introduced a thermodynamically consistent Phase-Field model for brittle fracturing in elastic solids. They formulated two models, one for rate-independent, and another for rate-dependent crack growth, which stabilizes the solution by adding a viscosity to the rate-independent model. They also proposed a method to split the energy into tensile and compressive parts, so as to let the material crack only in tension. In another work [53], they introduced a history into the model to ensure the irreversiblility of crack growth. This improvement also allowed for a staggered solution of the coupled equations that reduces the computational cost significantly. Kuhn and Müller [54] proposed new exponential shape functions for interpolation of the damage variable that allow for coarser finite element meshes and reduce the computational effort. However, since the proposed shapes functions fail to satisfy the partition of unity property the approach works only for some simple cases in which the crack path is known a priori and the domain is meshed in a way so that element edges are aligned with the crack path. Borden et al. [55] extended the model of Miehe et al. [53] to dynamic fracture. Hofacker and Miehe [56] extended the Phase-Field model for quasi-static fracture model by Miehe et al. [52, 53] to dynamic fracture. Verhoosel and de Borst [57] proposed a Phase-Field model for cohesive fracture, and in a later work, Vignollet et al. [58] revised the model and extended it particularly for propagative cracks. However, their model is incapable of solving arbitrary crack propagation. Borden et al. [59] extended the variational formulation further by introducing a fourth-order Phase-Field model.

The Phase-Field approach to fracture is advantageous in the sense that by modeling the cracks as a continuous smooth transition between phases eliminates the difficulties that arise in dealing with sharp discontinuities. It is also capable of modeling complex crack patterns, in contrast to traditional models. In this research we employed the Phase-Field Method to model the cracking of early-age concrete. We investigate the problem of differential shrinkage in spun-cast poles by numerical models involving segregation and shrinkage accounting for the heterogeneity of the material using different approaches, and evaluate and discuss the experimental observations and results provided by the research paper by Dilger et al. [1]. The only modeling study of this problem done by Tanfener [60] in his thesis using the Extended Finite Element Method and simple homogeneous models.

1.4 Scope and Aim of Thesis

As mentioned in previous sections, shrinkage is an important time-dependent phenomenon in concrete, since it may lead to damage that undermines the performance of the structure from the very beginning. We explained that shrinkage strains if restrained in any way cause stresses beyond the tensile strength of the concrete and thus resulting into cracks. In general the restraints can be categorized as internal, external. Internal restraints are due to presence of aggregates, or gradients in shrinkage strains due to differential drying or temperature gradients. External restraints are simply the structural restraints in connections and supports. An example of structures in which shrinkage can be detrimental are spun-cast concrete members, usually due to differential shrinkage strains that are a byproduct of segregation. These structures have diverse applications such as piles, columns, and utility poles to mention a few. Improper fabrication processes and/or inappropriate mix design can cause aggregate segregation that gives rise to a number of problems [1, 6, 61]. Inspection of spun-cast

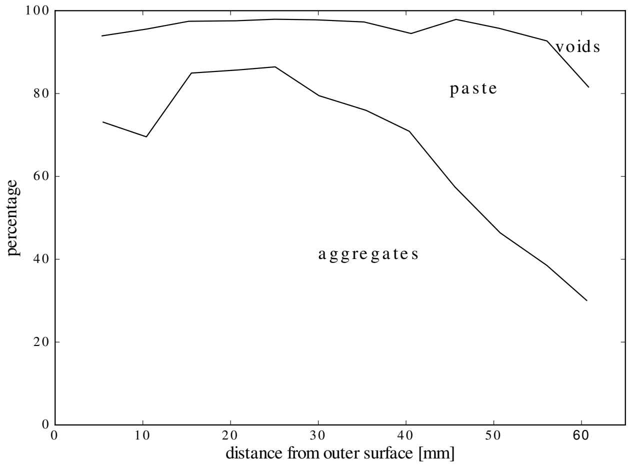

Figure 1.1: Distribution of aggregates, paste, and voids through the wall

poles in eastern Canada by utility companies unveiled that regardless of the overall good performance of the poles some of them had experienced some kind of damage that included horizontal and vertical cracking, rust stains, corrosion of reinforcement, and some spalling. In an effort to recognize the cause of damage and propose a remedy, Dilger et al. [1] examined a number of damaged poles, and designed a set of laboratory tests in an attempt to reproduce the observed damage in the field. The mostly observed kind of damage was vertical cracks. The cracks were initialized from the inside wall of the poles and extended either to the reinforcement bars or to the outer surface of the poles. The considerable segregation in the cross-sections seemed to be the main source of the problem, since it causes a differential shrinkage that can stress the sections to the point of cracking. The aim of their research was to identify the problem and propose appropriate mix design and casting process to eliminate cracking. Their study is perhaps the only experimental study of spun-cast concrete poles in the literature. First, they studied damaged poles in the field, and examined a severely

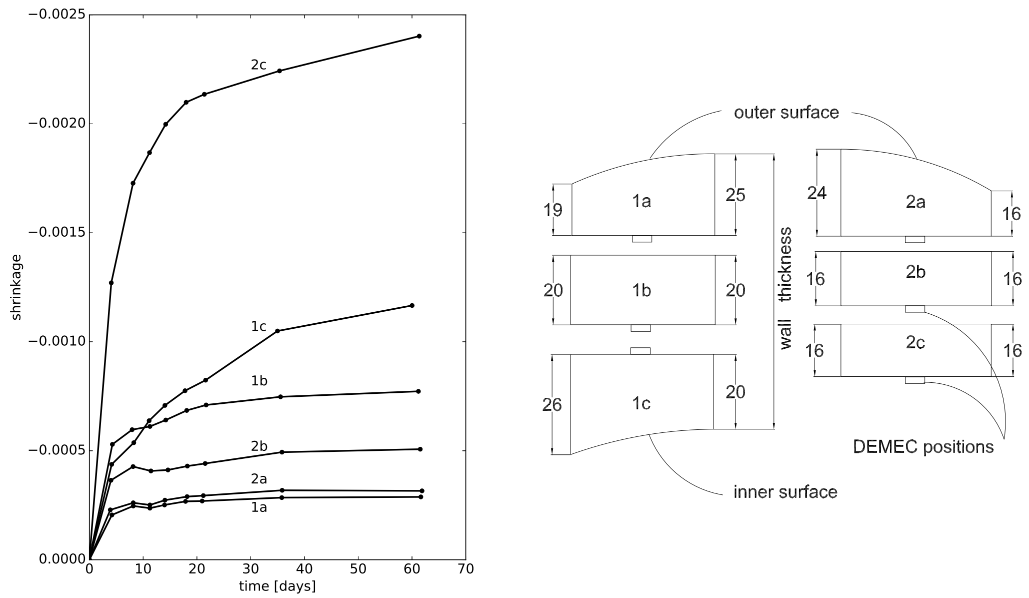

Figure 1.2: Evolution of shrinkage at different segments of the wall with time. (Shrinkage strains measured with Demountable Mechanical Strain Gages (DEMEC) at the points shown)

cracked pole in depth in the lab. Then, they produced new pole sections in the laboratory in order to reproduce the damage observed in the field, and analyze the probable causes. Finally, they investigated 67 trial specimens with different sets of mix design and various spinning speeds and durations in casting procedure in order to find a suitable mix design and production procedure. The most critical types of damage they observed were extensive deterioration and spalling in the zone near ground level and extensive radial cracking mostly passing reinforcement, which in return resulted in severe corrosion of the bars and spalling of the concrete cover. The section was segregated due to spinning during the production phase and they assumed it is the main cause for extensive cracking. Therefore, they produced a pole of 12 m in length using normal-weight concrete in the lab with similarly segregated sections. They made seven segments 1.2 m long and one 3.6 m by dividing the length using plywood disks. The longer segment was used for bending test. Five of the specimens were reinforced with no. 4 and 6 bars with different covers, and the remaining three had longitudinal slots. The slotted segments were used to observe shrinkage behavior by measuring the pole diameter and slot width. Some specimens were kept in the controlled laboratory environment, while others kept outside to assess the effect of environmental conditions on the behavior of the poles. In order to capture the variation of shrinkage strains, a segment was cut and sliced and stored in the laboratory and shrinkage measurements were conducted for about 18 months. Longitudinal strains, the relative humidity, and temperature were also measured. Similar crack patterns were observed

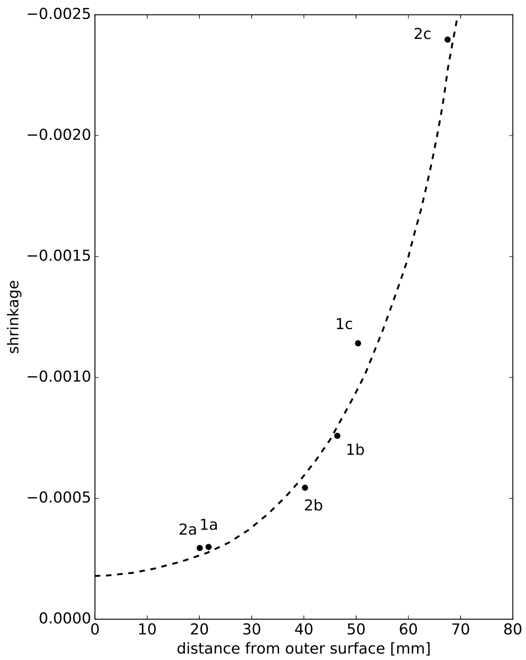

Figure 1.3: Approximate variation of shrinkage through the wall thickness

in the lab models. The only difference was that no crack has reached the outer surface. Cracks extended to the reinforcement, or in plain-concrete samples, stopped at a depth of 25 to 30 mm where the coarse aggregates existed, which can be seen in the photo they provided (see Figure 1.4). The shrinkage measurements at different layers, i.e. the differential shrinkage displayed a considerable difference through the wall thickness. The distribution of percentile amount of aggregates, paste, and voids through the wall thickness in the lab specimen is given in Figure 1.1. The aggregates are 0.35 parts fine and 0.65 parts coarse. The evolution of shrinkage strains at different radii with their respective segments are depicted in Figure 1.2 and the differential shrinkage across the pole wall is given in Figure 1.3. In this research we are going to study the shrinkage strains of the segregated pole numerically using both macro and meso models and also the resulting cracking using the Phase-Field Method implemented within the framework of the Coupled Finite Element Analyses.

The manuscript is organized as follows. Chapter 2 is devoted to the fundamentals of continuum thermomechanics within the geometrically linear setting. In chapter 3,

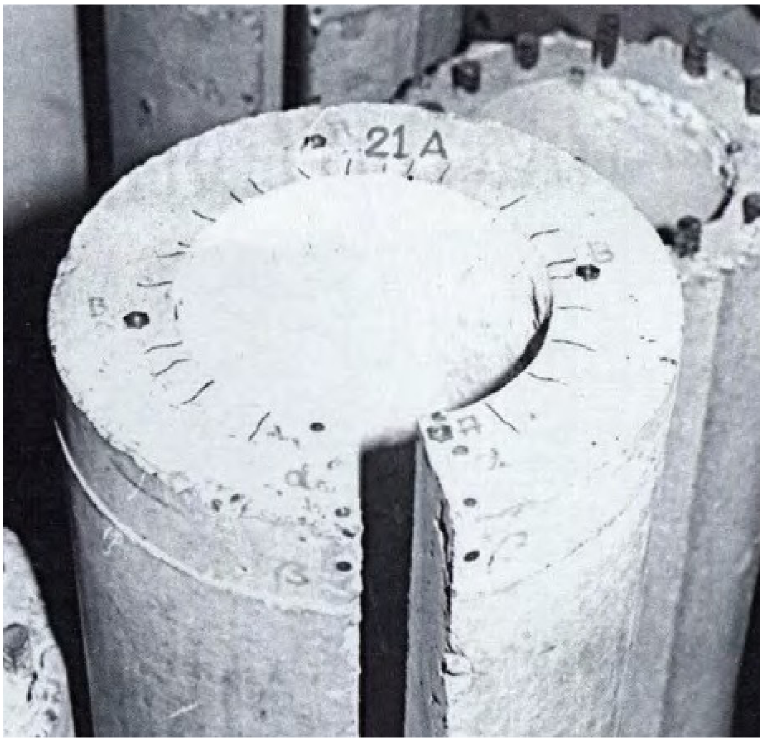

Figure 1.4: Typical cracking observed in laboratory specimens [1]

the fundamentals of linear elastic fracture mechanics is outlined briefly. Chapter 4 addresses the details of the Phase-Field formulation of differential-shrinkage-induced cracking in hardening concrete and provides the numerical and algorithmic treatment of the problem. Chapter 5 is concerned with the representative numerical examples that cover the convergence study, examples of brittle and quasi-brittle fracture, and the macroscopic and mesoscopic two-dimensional analyses of the pole section. Chapter 6 concludes the thesis by summarizing and critically assessing the work done. Moreover, possible extensions of the present work are outlined in the last chapter.

CHAPTER 2

FUNDAMENTALS OF CONTINUUM THERMODYNAMICS AT SMALL STRAINS

In this chapter some basic concepts and principles of geometrically linear continuum mechanics are presented. These concepts are needed for understanding the phase-field method for brittle fracture, and constitute a foundation for the later derivations and formulations of the method.
In reality material bodies are constituted by atoms and molecules, which may contain a considerable amount of empty space in between. This means that matter is in fact discontinuous. However, at macroscopic scale far beyond atomic and molecular dimensions, the assumption of the body as a continuum is reasonable and accurate enough for practical purposes. Fundamental principles of physics, i.e. conservation laws of mass, linear and angular momentum, energy and entropy are used along with some constitutive relations describing material behavior to formulate governing differential and integral equations of continuum mechanics. These equations are independent of coordinate systems that describe thermomechanical behavior of bodies of materials.

2.1 Kinematics

Kinematics deals with the motion of material particles or bodies regardless of the masses or the forces. The latter, i.e. study of motion taking into account the effect of forces and masses is within the realm of kinetics. Let's consider a material body

$\mathcal{B} \subset \mathbb{R}^D$ at time $t \in \mathbb{R}^+$, with D being the dimension of space. For a material point P at position $\boldsymbol{x} \in \mathcal{B}$, the displacement vector $\boldsymbol{u}(\boldsymbol{x}, t)$ as illustrated in Figure 2.1 is defined as

$$\boldsymbol{u}(\boldsymbol{x}, t) := \boldsymbol{x}(t) - \boldsymbol{x}(0). \tag{2.1}$$

Velocity $\boldsymbol{v}$ and $\boldsymbol{a}$ are defined as below

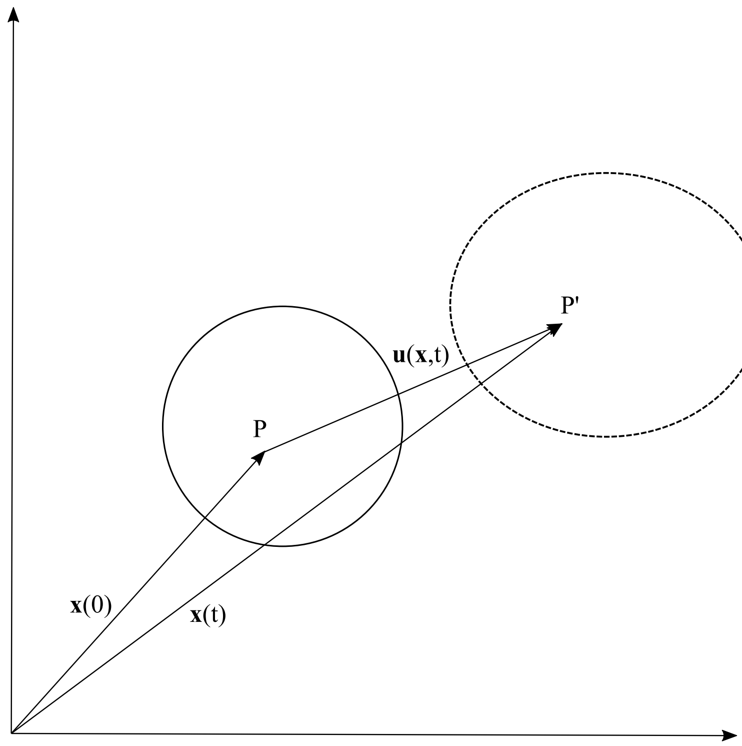

Figure 2.1: Reference and deformed configurations

$$\boldsymbol{v}(\boldsymbol{x}, t) := \frac{\partial \boldsymbol{u}(\boldsymbol{x}, t)}{\partial t}, \tag{2.2}$$

$$\boldsymbol{a}(\boldsymbol{x}, t) := \frac{\partial \boldsymbol{v}(\boldsymbol{x}, t)}{\partial t}. \tag{2.3}$$

The linearized strain tensor for infinitesimal deformations is defined as

$$\boldsymbol{\varepsilon}(\boldsymbol{x}, t) := \mathrm{sym}(\nabla \boldsymbol{u}) := \frac{1}{2}(\nabla \boldsymbol{u} + \nabla^T \boldsymbol{u}). \tag{2.4}$$

2.2 Cauchy Stress Tensor

The Cauchy stress tensor $\boldsymbol{\sigma}$ completely defines the state of stress at a material point inside the body. According to Cauchy's theorem, the traction vector $\boldsymbol{t}$ on a surface with the unit normal $\boldsymbol{n}$ is related to the stress tensor $\boldsymbol{\sigma}$ via the following relation

$$\boldsymbol{t} = \boldsymbol{\sigma}\boldsymbol{n} \tag{2.5}$$

2.3 Conservation Laws

Fundamental laws of physics used in continuum thermomechanics are presented here. First some basic physical quantities for a part $\mathcal{P}$ of the body $\mathcal{B}$ as illustrated in Figure 2.2 are defined

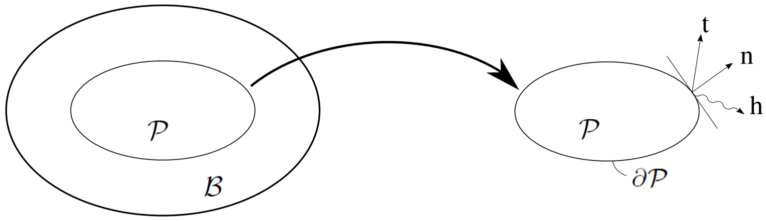

Figure 2.2: Part of a body subject to thermal and mechanical loads

$$\begin{array}{lll}
\bullet & \text{Mass:} & m = \int_{\mathcal{P}} \rho dV \\
\bullet & \text{Linear Momentum:} & \boldsymbol{I} = \int_{\mathcal{P}} \rho \boldsymbol{v} dV \\
\bullet & \text{Angular Momentum:} & \boldsymbol{D}_O = \int_{\mathcal{P}} \boldsymbol{x} \times \rho \boldsymbol{v} dV \\
\bullet & \text{Kinetic Energy:} & K = \int_{\mathcal{P}} \frac{1}{2}\rho |\boldsymbol{v}|^2 dV \\
\bullet & \text{Internal Energy:} & E = \int_{\mathcal{P}} \rho e dV \\
\bullet & \text{Entropy:} & H = \int_{\mathcal{P}} \rho \eta dV \\
\bullet & \text{Entropy Production Rate:} & \Gamma = \int_{\mathcal{P}} \rho \gamma dV
\end{array} \tag{2.6}$$

where $\rho(\boldsymbol{x}, t)$, $e(\boldsymbol{x}, t)$, $\eta(\boldsymbol{x}, t)$, and $\gamma(\boldsymbol{x}, t)$ are mass density, internal energy density, entropy density, and entropy production density, respectively.

The body is subjected to surface and volume loads. The thermomechanical quantities associated with these loads are

$$\begin{array}{lll}
\bullet & \text{Mechanical Force:} & \boldsymbol{F} = \int_{\mathcal{P}} \rho \boldsymbol{b} dV + \int_{\partial\mathcal{P}} \boldsymbol{t} dA \\
\bullet & \text{Mechanical Couple:} & \boldsymbol{M}_O = \int_{\mathcal{P}} \boldsymbol{x} \times \rho \boldsymbol{b} dV + \int_{\partial\mathcal{P}} \boldsymbol{x} \times \boldsymbol{t} dA \\
\bullet & \text{Mechanical Power:} & P = \int_{\mathcal{P}} \rho \boldsymbol{b} \cdot \boldsymbol{v} dV + \int_{\partial\mathcal{P}} \boldsymbol{t} \cdot \boldsymbol{v} dA \\
\bullet & \text{Thermal Power:} & Q = \int_{\mathcal{P}} \rho r dV - \int_{\partial\mathcal{P}} h dA \\
\bullet & \text{Entropy Power:} & S = \int_{\mathcal{P}} \rho \frac{r}{T} dV - \int_{\partial\mathcal{P}} \frac{h}{T} dA
\end{array} \tag{2.7}$$

where $\boldsymbol{b}$, $\boldsymbol{t}$, r, and T are the body force, surface traction, heat source, and absolute temperature, and h is the outward heat flux through the surface defined as $h := \boldsymbol{q} \cdot \boldsymbol{n}$.

2.3.1 Conservation of Mass

For closed systems without any mass exchange or internal mass production, the conservation of mass states that the total mass of a body $\mathcal{P}$ does not change during the motion. The global integral form is

$$\frac{dm}{dt} = 0. \tag{2.8}$$

Using the definition of m from (2.6), equation (2.8) can be rewritten as

$$\frac{d}{dt}\int_{\mathcal{P}} \rho dV = \int_{\mathcal{P}} \dot{\rho} dV = 0. \tag{2.9}$$

Using the localization theorem we have

$$\lim_{\mathcal{P}\to dV} \int_{\mathcal{P}} \dot{\rho} dV = 0 \qquad \Longrightarrow \qquad \dot{\rho} = 0. \tag{2.10}$$

2.3.2 Conservation of Linear Momentum

The principle of conservation of linear momentum, or Newton's second law of motion, can be stated as the time rate of linear momentum of a body part $\mathcal{P}$ equals the net force acting upon it. In the global integral form can be written as:

$$\frac{d\boldsymbol{I}}{dt} = \boldsymbol{F}. \tag{2.11}$$

Using the definitions in (2.6) and (2.7) we have:

$$\frac{d}{dt}\int_{\mathcal{P}} \rho \boldsymbol{v} dV = \int_{\mathcal{P}} (\dot{\rho}\boldsymbol{v} + \rho\dot{\boldsymbol{v}}) dV = \int_{\mathcal{P}} \rho \boldsymbol{b} dV + \int_{\partial\mathcal{P}} \boldsymbol{t} dA. \tag{2.12}$$

Using Cauchy's theorem and Gauss integral theorem the surface integral in (2.12) can be rewritten as:

$$\int_{\partial\mathcal{P}} \boldsymbol{t} dA = \int_{\partial\mathcal{P}} \boldsymbol{\sigma}\boldsymbol{n} dA = \int_{\mathcal{P}} \operatorname{div}(\boldsymbol{\sigma}) dV. \tag{2.13}$$

Substituting (2.13) back into (2.12) and using the result (2.10), we get

$$\int_{\mathcal{P}} (\rho\boldsymbol{a} - \operatorname{div}(\boldsymbol{\sigma}) - \rho\boldsymbol{b}) dV = 0. \tag{2.14}$$

Taking the limit we obtain

$$\lim_{\mathcal{P}\to dV}\int_{\mathcal{P}}(\rho\boldsymbol{a}-\mathrm{div}(\boldsymbol{\sigma})-\rho\boldsymbol{b})dV=0 \tag{2.15}$$

So, through the localization theorem the local differential form of conservation of linear momentum is achieved as follows

$$\rho\boldsymbol{a}=\mathrm{div}(\boldsymbol{\sigma})+\rho\boldsymbol{b}. \tag{2.16}$$

2.3.3 Conservation of Angular Momentum

The principle of conservation of angular momentum states that the time rate of total moment of linear momentum for a body part is equal to sum of the moments of forces acting on it. The global form is defined as

$$\frac{d\boldsymbol{D}_O}{dt}=\boldsymbol{M}_o. \tag{2.17}$$

Again, using the definitions in (2.6) and (2.7), (2.17) can be rewritten as

$$\frac{d}{dt}\int_{\mathcal{P}}\boldsymbol{x}\times\rho\boldsymbol{v}dV=\int_{\mathcal{P}}\boldsymbol{x}\times\rho\boldsymbol{b}dV+\int_{\partial\mathcal{P}}\boldsymbol{x}\times\boldsymbol{t}dA \tag{2.18}$$

Transforming the surface integral in (2.18) we have:

$$\int_{\partial\mathcal{P}}\boldsymbol{x}\times\boldsymbol{t}dA=\int_{\partial\mathcal{P}}\boldsymbol{x}\times\boldsymbol{\sigma}\boldsymbol{n}dA=\int_{\mathcal{P}}\boldsymbol{\epsilon}:\boldsymbol{\sigma}^TdV+\int_{\mathcal{P}}\boldsymbol{x}\times\mathrm{div}(\boldsymbol{\sigma})dV, \tag{2.19}$$

where, $\boldsymbol{\epsilon}$ is the permutaion symbol. Substituting (2.19) and using the conservation of mass (2.10) and linear momentum (2.16), the expression (2.18) simplifies to

$$\int_{\mathcal{P}}\boldsymbol{\epsilon}:\boldsymbol{\sigma}dV=0. \tag{2.20}$$

Taking the limit

$$\lim_{\mathcal{P}\to dV}\int_{\mathcal{P}}\boldsymbol{\epsilon}:\boldsymbol{\sigma}dV=0. \tag{2.21}$$

and using the localization theorem, we end up with

$$\boldsymbol{\epsilon}:\boldsymbol{\sigma}=0, \tag{2.22}$$

which implies:

$$\boldsymbol{\sigma}=\boldsymbol{\sigma}^T, \tag{2.23}$$

i.e. $\boldsymbol{\sigma}$ is symmetric. Therefore, the local form of conservation of angular momentum demands the stress tensor $\boldsymbol{\sigma}$ is symmetric.

2.3.4 Conservation of Energy

The principle of conservation of energy, which is also known as the first law of thermodynamics, states that heat and work can convert to each other. It does not put any constraint on the direction of the process. However, as we know, in reality heat dissipated during motion, as a result of friction for instance, is not recoverable and the process is irreversible. The second law of thermodynamics provides the restriction on irreversibility.
The first law of thermodynamics states that the time-rate of total energy is equal to the sum of the rate of work done by the external forces and the time change of heat content. It can be expressed as

$$\frac{d}{dt}(K+E) = P + Q. \tag{2.24}$$

From definitions in (2.6) and (2.7), we can rewrite (2.24) as

$$\frac{d}{dt}\left(\int_{\mathcal{P}} \frac{1}{2}\rho|\boldsymbol{v}|^2 dV + \int_{\mathcal{P}} \rho e dV\right) = \int_{\mathcal{P}} \rho \boldsymbol{b}\cdot\boldsymbol{v} dV + \int_{\partial\mathcal{P}} \boldsymbol{t}\cdot\boldsymbol{v} dA + \int_{\mathcal{P}} \rho r dV - \int_{\partial\mathcal{P}} h dA. \tag{2.25}$$

Transforming the surface integrals in (2.25) we have

$$\int_{\partial\mathcal{P}} \boldsymbol{t}\cdot\boldsymbol{v} dA = \int_{\partial\mathcal{P}} \boldsymbol{v}\cdot\boldsymbol{\sigma}\boldsymbol{n} dA = \int_{\mathcal{P}} (\nabla\boldsymbol{v} : \boldsymbol{\sigma} + \boldsymbol{v}\cdot \mathrm{div}(\boldsymbol{\sigma}))dV \tag{2.26}$$

$$\int_{\partial\mathcal{P}} h dA = \int_{\partial\mathcal{P}} \boldsymbol{q}\cdot\boldsymbol{n} dA = \int_{\mathcal{P}} \mathrm{div}(\boldsymbol{q}) dV \tag{2.27}$$

From (2.23) $\boldsymbol{\sigma} = \boldsymbol{\sigma}^T$, so $\nabla\boldsymbol{v} : \boldsymbol{\sigma} = \mathrm{sym}(\nabla\boldsymbol{v}) : \boldsymbol{\sigma} = \frac{d}{dt}\mathrm{sym}(\nabla\boldsymbol{u}) : \boldsymbol{\sigma} = \dot{\boldsymbol{\varepsilon}} : \boldsymbol{\sigma}$. Substituting all back into (2.25) and using the conservation of mass (2.10) and linear momentum (2.16), it simplifies to

$$\int_{\mathcal{P}} (\rho\dot{e} - \boldsymbol{\sigma} : \dot{\boldsymbol{\varepsilon}} - \rho r + \mathrm{div}(\boldsymbol{q}))dV = 0. \tag{2.28}$$

Taking the limit $\mathcal{P} \to dV$ and using the localization theorem, we get the local form of conservation of energy as below

$$\rho\dot{e} = \boldsymbol{\sigma} : \dot{\boldsymbol{\varepsilon}} + \rho r - \mathrm{div}(\boldsymbol{q}) \tag{2.29}$$

2.3.5 Conservation of Entropy

For an irreversible process, the principle of conservation of entropy, which is also referred to as the second law of thermodynamics, requires that the dissipation rate, i.e. the internal entropy production must be positive. It can be written as

$$\Gamma = \frac{dH}{dt} - S \geq 0. \tag{2.30}$$

Again, form definitions in (2.6) and (2.7) we obtain

$$\int_{\mathcal{P}} \rho\gamma dV = \frac{d}{dt}\int_{\mathcal{P}} \rho\eta dV - \int_{\mathcal{P}} \rho\frac{r}{T} dV + \int_{\partial\mathcal{P}} \frac{h}{T} dA \geq 0. \tag{2.31}$$

Transforming the surface integral into a volume integral

$$\int_{\partial\mathcal{P}} \frac{h}{T} dA = \int_{\partial\mathcal{P}} \frac{1}{T}\boldsymbol{q}\cdot\boldsymbol{n} dA = \int_{\mathcal{P}} (\frac{1}{T}\mathrm{div}(\boldsymbol{q}) - \frac{1}{T^2}\boldsymbol{q}\cdot\nabla T) dV, \tag{2.32}$$

and substituting it back into equation (2.31), taking the limit $\mathcal{P} \to dV$, and using the localization theorem result in

$$\rho\gamma = \rho\dot{\eta} - \frac{1}{T}(\rho r - \mathrm{div}(\boldsymbol{q})) - \frac{1}{T^2}\boldsymbol{q}\cdot\nabla T \geq 0, \tag{2.33}$$

which is the local form of conservation of entropy. Using the conservation of energy in (2.29) it can also be written in the following form:

$$\rho\gamma = \rho\dot{\eta} - \frac{1}{T}(\rho\dot{e} - \boldsymbol{\sigma} : \dot{\boldsymbol{\varepsilon}}) - \frac{1}{T^2}\boldsymbol{q}\cdot\nabla T \geq 0. \tag{2.34}$$

2.4 Thermodynamic Consistency

For a realistic material modeling, it is required that a constitutive model complies with the second law of thermodynamics. The rate of energy loss during a process, i.e. dissipation is defined by

$$D := T\rho\gamma \geq 0. \tag{2.35}$$

Using the result (2.34), we can write the dissipation as

$$D = \boldsymbol{\sigma} : \dot{\boldsymbol{\varepsilon}} - \rho\dot{e} + \rho T\dot{\eta} - \frac{1}{T}\boldsymbol{q}.\nabla T \geq 0. \tag{2.36}$$

The inequality in (2.36) is called the Clausius-Duhem Inequality. It can be split into two parts namely the local and conductive parts as:

$$D_{loc} = \boldsymbol{\sigma} : \dot{\boldsymbol{\varepsilon}} - \rho\dot{e} + \rho T\dot{\eta} \geq 0 \tag{2.37}$$

$$D_{con} = -\frac{1}{T}\boldsymbol{q}.\nabla T \geq 0. \tag{2.38}$$

The inequalities (2.37) and (2.38) are called the Clausius-Planck Inequality and Fourier Inequality, respectively. An alternative form of the Clausius-Planck Inequality can be written using the Helmholtz free energy function $\psi := e - T\eta$

$$D_{loc} = \boldsymbol{\sigma} : \dot{\boldsymbol{\varepsilon}} - \rho\dot{\psi} - \rho\eta\dot{T} \geq 0 \tag{2.39}$$

So, for a material model to be thermodynamically consistent, its constitutive relations must satisfy the Clausius-Duhem Inequality (2.36), or the latter two alternatives (2.39, 2.38), i.e. the Clausius-Planck and Fourier inequalities.

CHAPTER 3

FUNDAMENTALS OF LINEAR ELASTIC FRACTURE MECHANICS

In this chapter some basic concepts of linear elastic fracture mechanics are presented. This will give the reader some insight into the fundamental concepts of fracture analysis.

Fracture mechanics is the branch of mechanics that deals with the effects of cracks and how they propagate. In general, a cracked body consists of three zones (Figure 3.1)

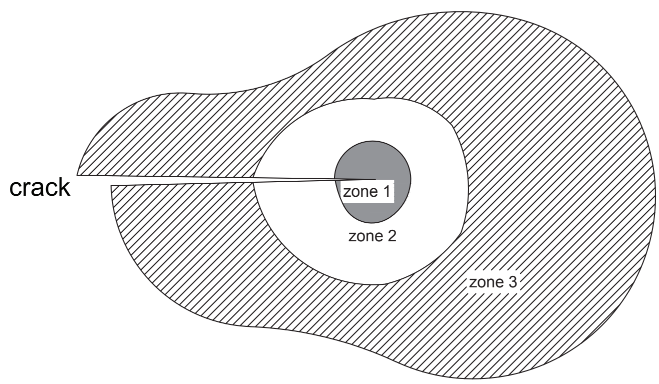

Figure 3.1: Zones around the crack tip

- **Zone 1, Fracture process zone:** It is around the crack tip and the material is damaged because of large stresses, and becomes discontinuous. It is very small and in classical fracture mechanics it is reduced to a point for two-dimensional cases and a line for three-dimensional problems.

- **Zone 2, Singular zone:** Here the mechanical fields are continuous, but different from the fields far from the crack. The stress field is asymptotic in the vicinity of the crack tip, and tends to very large values. So, the material becomes plastic near the crack tip and based on the size of the plastic zone the crack is considered as being ductile or brittle.

- **Zone 3, External zone:** This zone is far from singular zone around the crack tip and the mechanical fields vary little.

Fracture mechanics deals with determination of mechanical fields and energy around the crack tip and the evolution of a crack. So, first it is needed to model the singularity around the crack and then define criteria for crack propagation.
Linear elastic fracture mechanics is the most basic and simplest form that assumes the material is linear elastic. Fracture mechanics theories have evolved to deal with nonlinear behavior and dynamic effects, but all the developments are extensions of linear elastic fracture mechanics. Here we are only going to deal with some concepts of linear elastic fracture mechanics.

3.1 Modes of Fracture

There are three basic fracture modes that are illustrated in Figure 3.2

- **Mode I**: crack opening mode, where the displacement of the crack lips are normal to the crack plane.

- **Mode II**: in-plane shear mode, where the displacement of the crack lips are parallel to the crack extension direction.

- **Mode III**: out-of-plane shear mode, where the displacement of the crack lips are in the crack plane but perpendicular to crack extension.

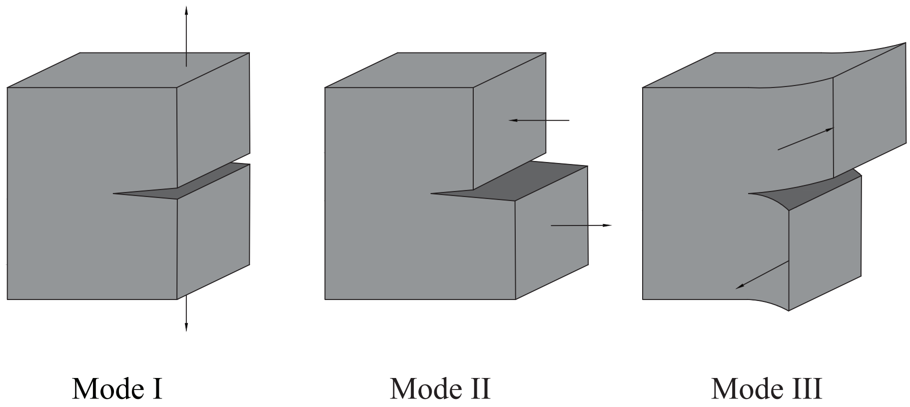

Figure 3.2: Three modes of fracture

3.2 Stress Concentration

Consider a plate with an elliptical hole under applied stress perpendicular to the major axis of the ellipse as in Figure 3.3. It is assumed that the plate dimensions are far

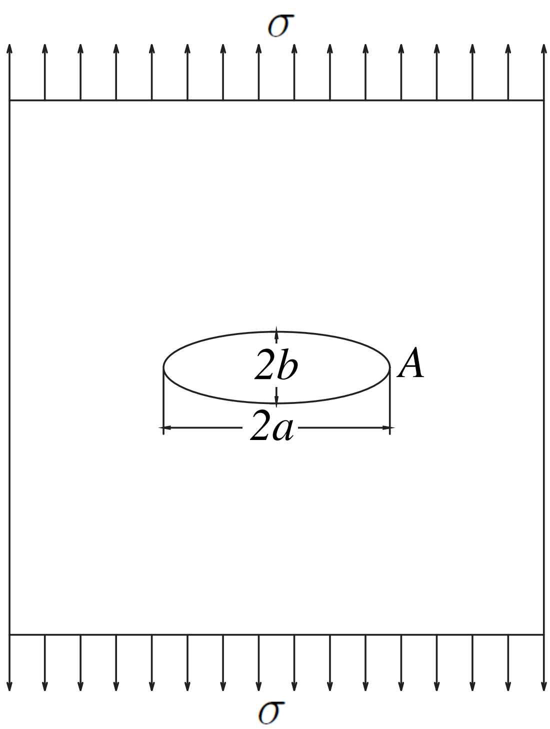

Figure 3.3: Plate with elliptical hole

greater than the size of the hole. Elasticity solution for the stress at the tip of the longer axis of the hole is

$$\sigma_A = \sigma(1 + \frac{2a}{b}) \tag{3.1}$$

The stress concentration factor K defined as the ratio σ_A/σ is then $1 + \frac{2a}{b}$, which for a circular hole equals to 3. It can be seen that for $a \gg b$, i.e. when the hole tends to a sharp crack, the stress value tends to infinity. However, cracks are not sharp in reality and the deformations at the crack tip are plastic, which causes the sharp crack tip to flatten.

3.3 The Griffith Energy Balance

Since the elasticity solutions give an infinite stress at the tip of a sharp crack, Griffith employed a thermodynamic approach to crack formation [37]. Consider a plate under remote stresses with a crack of length $2a$ assuming the plate width, much greater than $2a$ (Figure 3.4). In order for the crack to grow, enough energy must be available in

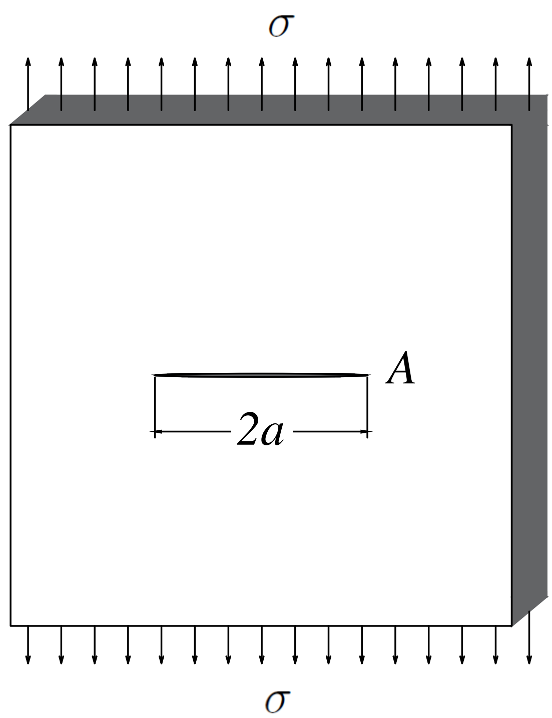

Figure 3.4: Plate with a through-thickness crack with a thickness B

the plate to provide the surface energy of material. For an incremental increase in the crack area dA in equilibrium conditions, the energy balance can be written as:

$$\frac{dE}{dA} = \frac{d\Pi}{dA} + \frac{dE_s}{dA} = 0, \tag{3.2}$$

where E is the total energy, Π is the potential, and E_s is the crack surface energy. The elasticity solution gives Π for the plate as

$$\Pi = \Pi_0 - \frac{\pi\sigma^2 a^2 B}{E}, \tag{3.3}$$

where, Π_0 is potential for an uncracked plate. Since crack formation creates two surfaces, the crack surface energy E_s is given as

$$E_s = 2\gamma_s A = 4aB\gamma_s, \tag{3.4}$$

with γ_s being the surface energy density, i.e. the energy needed to crate a unit crack surface. Substitution of E_e and E_s from (3.3) and (3.4) into the balance equation (3.2) gives the fracture stress as below

$$\sigma_f = \sqrt{\frac{2E\gamma_s}{\pi a}}. \tag{3.5}$$

3.4 Generalized Griffith equation

The fracture stress, given in (3.5), is for brittle materials. Griffith got a good agreement between fracture strengths from (3.5) and experimental results for glass. However, the Griffith equation does not hold for metals and gives underestimated values. So, Irwin [62] and Orowan [63] modified the expression in (3.5) to take into account plastic deformations

$$\sigma_f = \sqrt{\frac{2E(\gamma_e + \gamma_p)}{\pi a}}, \tag{3.6}$$

where γ_e and γ_p represent elastic and plastic surface energy densities, respectively. In general, the Griffith model can be extended to account for any kind of dissipation

$$\sigma_f = \sqrt{\frac{2E\gamma_f}{\pi a}}, \tag{3.7}$$

where γ_f is the fracture energy that can include any plastic, viscoelastic, or viscoplastic effects.

3.5 Energy Release Rate

Energy release rate G is defined as the available energy for an incremental crack growth

$$G = -\frac{d\Pi}{dA}. \tag{3.8}$$

Since G is the derivative of a potential, it is also called the crack driving force. From Equation (3.3) for a wide plate in Figure 3.4 we have

$$G = \frac{\pi\sigma^2 a}{E} \tag{3.9}$$

When the energy release rate reaches a critical value crack starts to grow

$$G_c = \frac{dE_c}{dA} = 2\gamma_f, \tag{3.10}$$

where G_c is the critical energy release rate and a measure of fracture toughness of the material. The potential energy for an elastic body is as

$$\Pi = E_e - W, \tag{3.11}$$

where E_e is the strain energy stored in the body and W is the work done by external forces.

3.6 Stability of Crack Growth

Crack grows if $G = 2\gamma_f$, where $2\gamma_f$ is the resistance to cracking R. Resistance curve or R curve is the plot of resistance against crack growth. The way G and R change with crack size determines the crack growth stability. The R curves for two types of material behavior are shown in Figure 3.5. For the flat R curve in Figure 3.5 (a), the material resistance remains constant with crack extension. When stress reaches σ_2 crack grows in an unstable manner, because the driving force keeps increasing with crack size while the resistance remains constant. For the rising R curve shown in Figure 3.5 (b) as long as the stress is smaller than σ_4 crack can grow a small amount stably, because the resistance increase is greater than the driving force. However, when the stress reaches σ_4 the driving force curve becomes tangent to the resistance curve and crack growth gets unstable, because the driving force changes more than

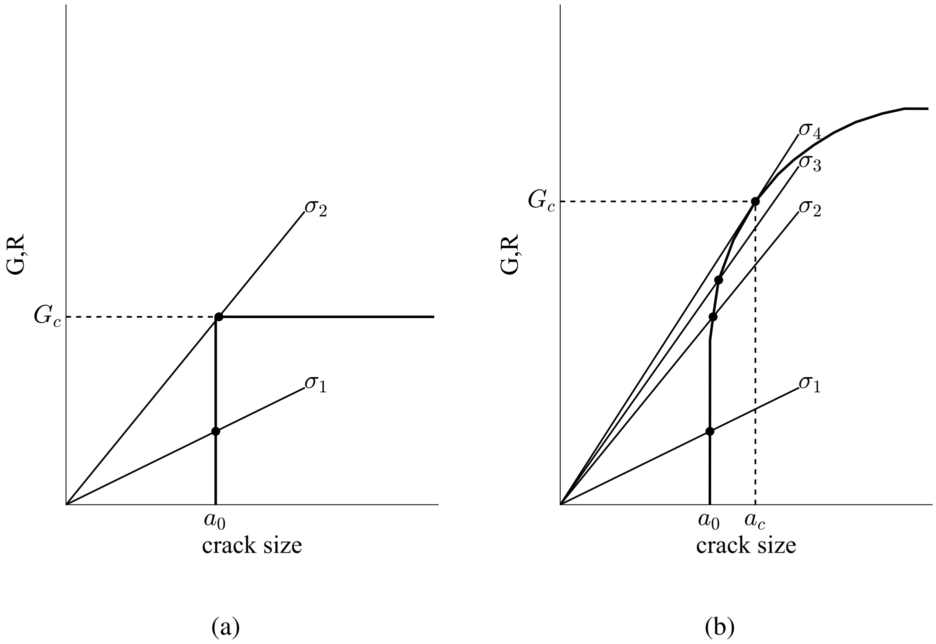

Figure 3.5: G and R curves for (a) a flat and (b) a rising R curve

the resistance.

The conditions for stable crack growth can then be expresses as

$$G = R \quad \text{and} \quad \frac{dG}{da} \leq \frac{dR}{da}, \tag{3.12}$$

and crack growth gets unstable if

$$\frac{dG}{da} > \frac{dR}{da}, \tag{3.13}$$

It is noted that for a flat resistance curve, it is possible to define a critical energy release rate G_c that signify the failure of the structure. However, in the case of a rising resistance curve, a critical value G_c cannot be determined clearly. The failure occurs when the driving force curve becomes tangent to the resistance, but the crack size at which this happens is also dependent on the shape of the G curve, which in turn is a function of the configuration.

The change of driving force G with crack size depends on the type of loading. Displacement-controlled loading usually results in a more stable crack growth than the load-controlled one. A typical case is illustrated in Figure 3.6.

The R curve's shape depends on the material behavior and also on the configuration. For an ideally brittle material the R curve is flat, but for the nonlinear behavior, it can take different shapes. For metals that are ductile materials, the R curve is usu-

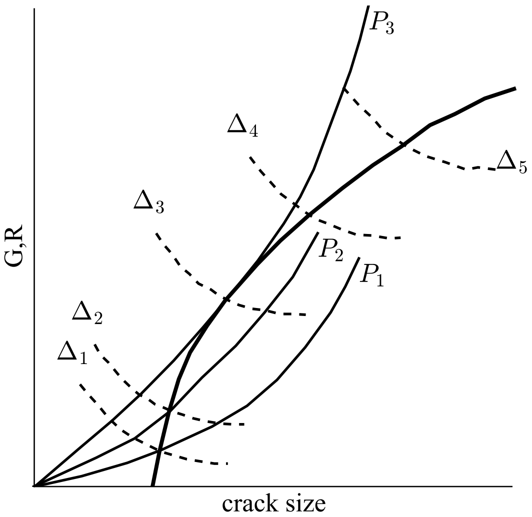

Figure 3.6: G and R curves for displacement and load control

ally a rising one. Since the plastic zone around the crack tip increases as the crack grows, the resistance of the body also increases. Cleavage fracture in metals can have a falling R curve. If the crack grows rapidly the plastic deformation is limited and that results in lesser resistance than when crack initiated. The size and geometry can also affect the R curve. For example, the R curve for cracking in a thin plate can be steeper than the one for cracking in a thick plate. Or, when crack approaches the boundary, the R curve can change as well.

3.7 Stress Analysis

For some crack geometries and loadings, analytic elasticity solutions are available. Westergaard, Irwin, and Williams, to name a few, are among the first people who derived such solutions. It can be shown that the stress field around a crack tip for a linear elastic material has a general form as given below:

$$\sigma_{ij} = \frac{K}{\sqrt{2\pi r}} f_{ij}(\theta) + \sum_{m=0}^{\infty} A_m r^{\frac{m}{2}} g_{ij,m}(\theta), \tag{3.14}$$

where r and θ are radius and the angle of the polar coordinate with the origin located at the crack tip as show in Figure 3.7, σ_{ij} are stress components, f_{ij} and $g_{ij,m}$ are functions of θ and A_m and k are constants. The expression (3.14) is singular at the crack tip, i.e. $r = 0$. As $r \to 0$ the first term tends to infinity, while the other terms

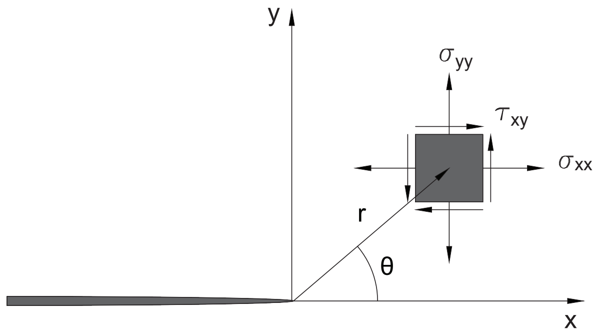

Figure 3.7: Coordinate system at the crack tip

remain finite, so near the crack tip stress varies proportional to $1/\sqrt{r}$.

3.8 Stress Intensity Factor

As mentioned earlier, at the vicinity of the crack tip the first term of the expression (3.14) governs and the stress is proportional to $1/\sqrt{r}$. The constants K and f_{ij} need to be determined for the specific loading at hand. K is the stress intensity factor. So, the asymptotic stress field at the crack tip for different modes can be written as

$$\lim_{r\to 0} \sigma_{ij}^{(I)} = \frac{K_I}{\sqrt{2\pi r}} f_{ij}^{(I)}(\theta) \tag{3.15a}$$

$$\lim_{r\to 0} \sigma_{ij}^{(II)} = \frac{K_{II}}{\sqrt{2\pi r}} f_{ij}^{(II)}(\theta) \tag{3.15b}$$

$$\lim_{r\to 0} \sigma_{ij}^{(III)} = \frac{K_{III}}{\sqrt{2\pi r}} f_{ij}^{(III)}(\theta) \tag{3.15c}$$

Since the material is linear elastic, for a mixed loading one can get the stress components by superposing individual stresses due to each mode

$$\sigma_{ij} = \sigma_{ij}^{(I)} + \sigma_{ij}^{(II)} + \sigma_{ij}^{(III)} \tag{3.16}$$

The expressions for nonzero stress fields at the crack tip for mode I are as follows

$$\sigma_{xx} = \frac{K_I}{\sqrt{2\pi r}} \cos(\frac{\theta}{2}) \left[1 - \sin(\frac{\theta}{2}) \sin(\frac{3\theta}{2})\right] \tag{3.17a}$$

$$\sigma_{yy} = \frac{K_I}{\sqrt{2\pi r}} \cos(\frac{\theta}{2}) \left[1 + \sin(\frac{\theta}{2}) \sin(\frac{3\theta}{2})\right] \tag{3.17b}$$

$$\tau_{xy} = \frac{K_I}{\sqrt{2\pi r}} \cos(\frac{\theta}{2}) \sin(\frac{\theta}{2}) \cos(\frac{3\theta}{2}) \tag{3.17c}$$

$$\sigma_{zz} = 0 \quad \text{for plane stress,} \quad \sigma_{zz} = \nu(\sigma_{xx} + \sigma_{yy}) \quad \text{for plane strain} \tag{3.17d}$$

The expressions for nonzero stress fields at the crack tip for mode II are as follows

$$\sigma_{xx} = -\frac{K_{II}}{\sqrt{2\pi r}} \sin(\frac{\theta}{2}) \left[2 + \cos(\frac{\theta}{2}) \cos(\frac{3\theta}{2})\right] \tag{3.18a}$$

$$\sigma_{yy} = \frac{K_{II}}{\sqrt{2\pi r}} \sin(\frac{\theta}{2}) \cos(\frac{\theta}{2}) \cos(\frac{3\theta}{2}) \tag{3.18b}$$

$$\tau_{xy} = \frac{K_{II}}{\sqrt{2\pi r}} \cos(\frac{\theta}{2}) \left[1 - \sin(\frac{\theta}{2}) \sin(\frac{3\theta}{2})\right] \tag{3.18c}$$

$$\sigma_{zz} = 0 \quad \text{for plane stress,} \quad \sigma_{zz} = \nu(\sigma_{xx} + \sigma_{yy}) \quad \text{for plane strain} \tag{3.18d}$$

Also for mode III we have

$$\tau_{xz} = -\frac{K_{III}}{\sqrt{2\pi r}} \sin(\frac{\theta}{2}) \tag{3.19a}$$

$$\tau_{yz} = \frac{K_{III}}{\sqrt{2\pi r}} \cos(\frac{\theta}{2}) \tag{3.19b}$$

The displacement fields for mode I are given as

$$u_x = \frac{K_I}{2\mu} \sqrt{\frac{r}{2\pi}} \cos(\frac{\theta}{2}) \left[\kappa - 1 + 2\sin^2(\frac{\theta}{2})\right] \tag{3.20a}$$

$$u_y = \frac{K_I}{2\mu} \sqrt{\frac{r}{2\pi}} \sin(\frac{\theta}{2}) \left[\kappa + 1 - 2\cos^2(\frac{\theta}{2})\right] \tag{3.20b}$$

The displacement fields for mode II are also as below

$$u_x = \frac{K_{II}}{2\mu} \sqrt{\frac{r}{2\pi}} \sin(\frac{\theta}{2}) \left[\kappa + 1 + 2\cos^2(\frac{\theta}{2})\right] \tag{3.21a}$$

$$u_y = -\frac{K_{II}}{2\mu} \sqrt{\frac{r}{2\pi}} \cos(\frac{\theta}{2}) \left[\kappa - 1 - 2\sin^2(\frac{\theta}{2})\right] \tag{3.21b}$$

The only nonzero displacement for mode III is the z component

$$u_z = \frac{K_{III}}{2\mu} \sqrt{\frac{r}{2\pi}} \sin(\frac{\theta}{2}) \tag{3.22}$$

The stress intensity factor determines the intensity, as the name suggests, of the singularity at the crack tip, i.e. stresses are proportional to K. If K is known, then all stresses, strains, and displacements can be determined at the vicinity of the crack tip.

3.9 Evaluation of Stress Intensity Factor

As mentioned in the previous section, the stress, strain, and displacement fields can be evaluated around the crack tip provided that the stress intensity factor be known. There exist analytical solutions for several simple cases. For more complex problems the stress intensity factor can be evaluated using experimental or numerical methods. Solutions for some simple cases are given here.

One case that has a closed-form solution is the through-thickness crack in an infinite plane with a remote tensile loading of mode I (Figure 3.4). It can be shown that the solution for K is as given below

$$K_I = \sigma\sqrt{\pi a} \tag{3.23}$$

For a mode II loading of the latter, i.e. remote tensile stresses are replaced by shear stress τ is similar

$$K_{II} = \tau\sqrt{\pi a} \tag{3.24}$$

Another related problem is a semi-infinite crack with an edge crack as shown in Figure 3.8

$$K_I = 1.12\sigma\sqrt{\pi a} \tag{3.25}$$

Another simple case with closed form solution is the infinite body with circular crack under remote tensile loading (Figure 3.9)

$$K_I = \frac{2}{\pi}\sigma\sqrt{\pi a} \tag{3.26}$$

Most closed-form solutions are for infinite medium, i.e. the dimensions of the body are far greater than the crack size. For the cases where the dimensions of the body are comparable to the crack size, the boundary conditions influence the crack tip fields. Usually for these problems there is no closed-form solutions possible, and the stress intensity factor needs to be evaluated employing either numerical or experimental methods. As an example, consider a plate of finite width $2W$ including a through-thickness crack under remote tensile loading. One approach is to assume an infinite plate with a repeating array of collinear cracks as illustrated in Figure 3.10. Then, the stress intensity factor is given by

$$K_I = \sigma\sqrt{\pi a}\sqrt{\frac{2W}{\pi a}\tan(\frac{\pi a}{2W})} \tag{3.27}$$

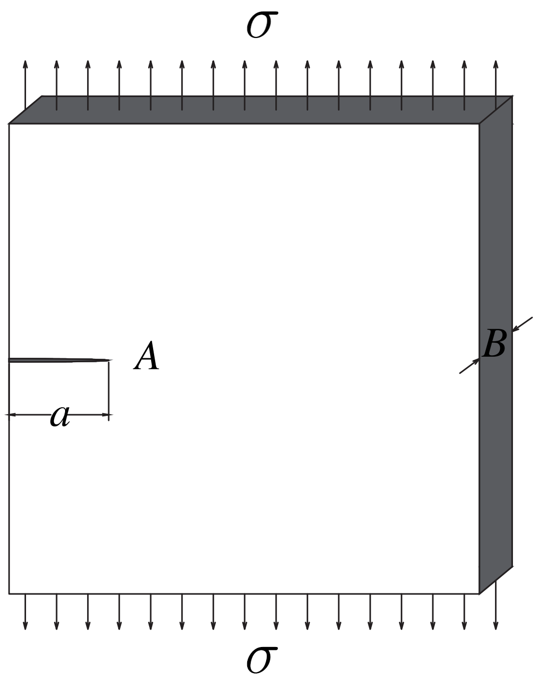

Figure 3.8: Edge-cracked semi-infinite plate under mode I loading

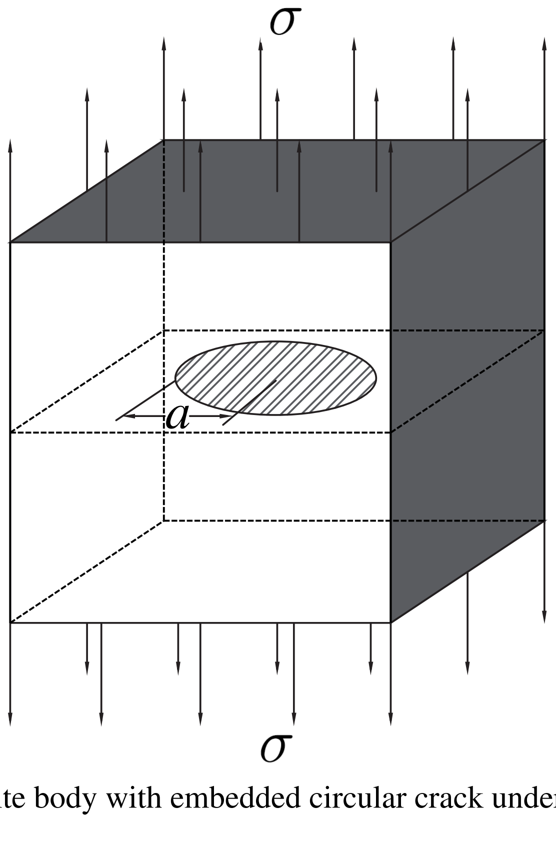

Figure 3.9: Infinite body with embedded circular crack under mode I loading

Better solutions are determined using the Finite Element Method, as given below

$$K_I = \sigma\sqrt{\pi a}\sqrt{\sec(\frac{\pi a}{2W})}\left[1 - 0.025(\frac{a}{W})^2 + 0.06(\frac{a}{W})^4\right]. \tag{3.28}$$

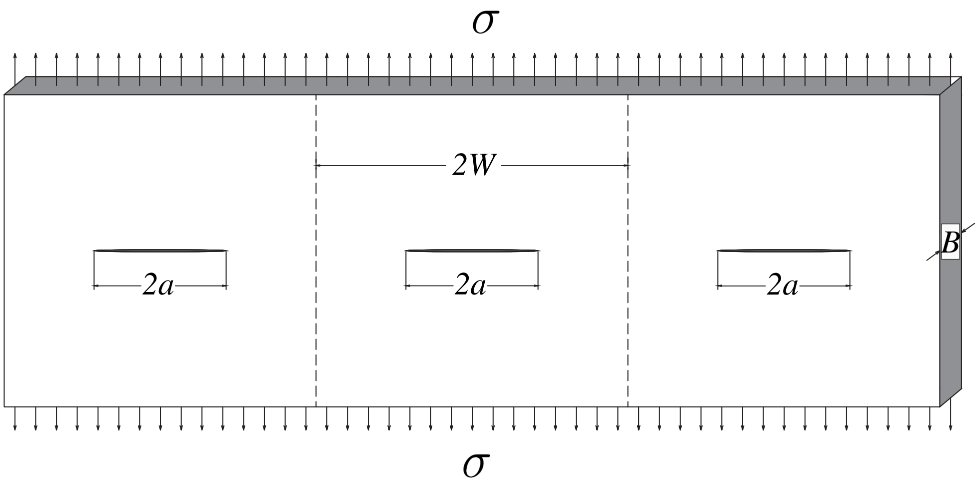

Figure 3.10: An infinite plate with collinear cracks under mode I loading

3.10 The Relation between K and G

The energy release rate, as defined before, is the change in energy due to crack growth, and the stress intensity factor is related to the stress field at the crack tip. For linear elastic materials, there is a unique relation between these two parameters. For the infinite plate with through-the-thickness crack in mode I loading in Figure 3.4, G and K are given by the relations (3.9) and (3.23), respectively. Using these equations, the relation between G and K for plane stress conditions is achieved as

$$G = \frac{K_I^2}{E} \tag{3.29}$$

For plane strain conditions E is replaced by $E/(1-\nu^2)$. In the following it will be shown that the latter relationship between K and G holds in general.
Assume a crack of length $a + \Delta a$ in mode I loading as shown in Figure 3.11 (a). We seek to evaluate the work required to close the crack by an amount Δa. This work must be equal to the energy released for the same amount of crack extension. So

$$dW_{closure} = GdA \tag{3.30}$$

Then, we can write

$$G = \lim_{\Delta A \to 0} \frac{\Delta W_{\text{closure}}}{\Delta A} \tag{3.31}$$

Plate thickness is B, so $A = aB$ and then we have

$$G = \frac{1}{B} \lim_{\Delta a \to 0} \frac{\Delta W_{\text{closure}}}{\Delta a} \tag{3.32}$$

The work is the area under force-displacement curve. So

$$\Delta W_{\text{closure}} = \int_0^{\Delta a} 2 \times \frac{1}{2} u_y dF = \int_0^{\Delta a} u_y(x,0)\sigma_{yy}(x,0) B dx \tag{3.33}$$

Substituting equations (3.17b) and (3.20b) for $r = \Delta a - x$ and $\theta = \pi$ and evaluating the integral, we end up with

$$\Delta W_{\text{closure}} = \frac{K_I(a+\Delta a)K_I(a)(\kappa+1)B\Delta a}{8\mu} \tag{3.34}$$

Finally, substituting $\Delta W_{\text{closure}}$ from (3.34) into (3.32) and taking the limit, we obtain the relation between G and K for mode I loading as

$$G = \frac{K_I^2(\kappa+1)}{8\mu}, \tag{3.35}$$

which substituting the definition of κ gives $G = K_I^2/E$ for plane stress and $G = K_I^2(1-\nu^2)/E$ for plane strain. Assuming self-similar crack growth for mixed-mode loading, using a similar approach, we can write

$$G = \frac{\kappa+1}{8\mu}(K_I^2 + K_{II}^2) + \frac{K_{III}^2}{2\mu} \tag{3.36}$$

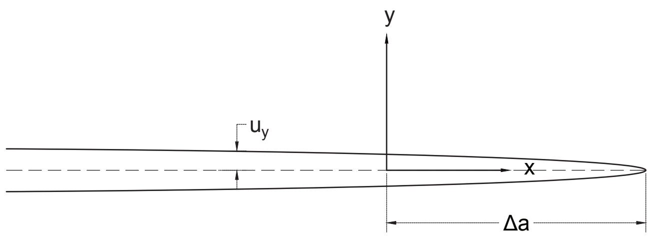

(a)

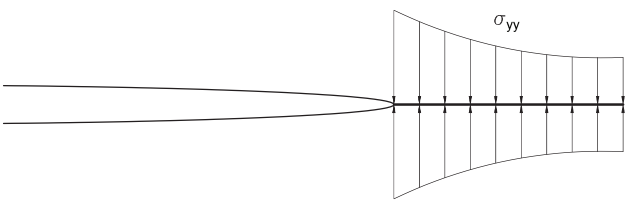

(b)

Figure 3.11: Crack before and after closure

3.11 Small-Scale Yielding

For a sharp crack, linear elastic solutions give infinite stresses at the crack tip. However, in reality crack tip has a finite radius, which results in finite stress values. Also due to large stresses at the crack tip, the material yields and undergoes inelastic deformations. For small-scale yieldings, simple corrections can be applied to linear elastic fracture mechanics. One such corrections is the Irwin approach. It is assumed that primary influence of loacalized plastic deformation on stress distribution for mode I problem is to translate the curve to the right by an amount such that the new area under added under stress curve equals the area between linear elastic stress curve and the yield stress σ_Y. The elastic stress distribution and the new corrected distribution is illustrated in Figure 3.12. With this assumption we can write

$$\int_0^{r_y} [\sigma_{yy}(x,0) - \sigma_Y]\, dx = \sigma_Y(r_p - r_y), \tag{3.37}$$

where r_y denotes the initial yielded zone radius and r_p is the new corrected plastic zone radius.Assuming plane stress conditions r_y is as below

$$r_y = \frac{K_I^2}{2\pi\sigma_Y^2}. \tag{3.38}$$

Using equation (3.17b) and (3.38) in (3.37) and solving for r_p we get

$$r_p = \frac{K_I^2}{\pi\sigma_Y^2} = 2r_y. \tag{3.39}$$

For plane strain conditions Irwin suggested that $\sqrt{3}\sigma_Y$ be used instead of σ_Y, so for plane strain we have

$$r_p = \frac{K_I^2}{3\pi\sigma_Y^2}. \tag{3.40}$$

Since the stress in the plastic zone is less than the elastic stress before correction, Irwin defined an effective crack length as

$$a_{\text{eff}} = a + r_y. \tag{3.41}$$

So, the effective stress intensity factor using a_{eff} instead off a becomes as follows

$$K_{\text{eff}} = \beta(a_{\text{eff}})\sigma\sqrt{\pi a_{\text{eff}}}, \tag{3.42}$$

where β is the geometry correction factor. For example the effective stress intensity factor for a through-thickness crack in an infinite plate in plane stress conditions is as

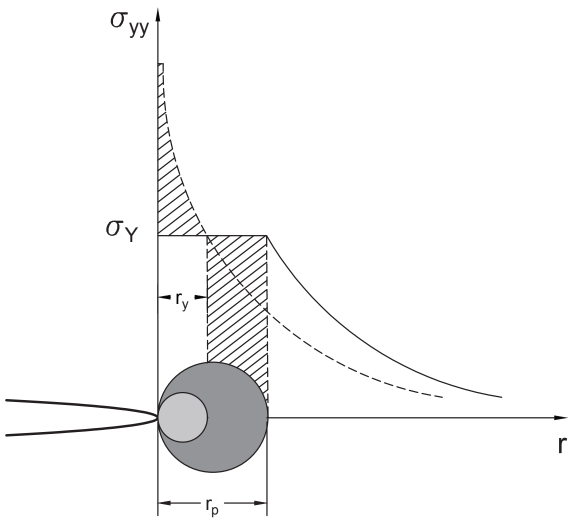

Figure 3.12: Irwin plastic zone correction

below

$$K_{\text{eff}} = \frac{\sigma\sqrt{\pi a}}{\sqrt{1 - \frac{1}{2}(\frac{\sigma}{\sigma_Y})^2}}. \tag{3.43}$$

CHAPTER 4

PHASE-FIELD FORMULATION AND FINITE ELEMENT IMPLEMENTATION

4.1 Phase-Field Method for Quasi-Brittle Fracture

In the Phase-Field Method we assume the fracture as one phase and the uncracked solid as another phase. Each phase is assigned with an energy expression in terms of the state variables and an order parameter d - also called the damage parameter here - that takes a specific value at each phase, e.g. 1 for fracture and 0 for the uncracked solid phase. The energy of each phase is written in a manner that facilitates smooth transition between phases and replaces the sharp interface with a smeared one. Then, the total energy of the body is written and minimized to get the governing differential equations.

4.1.1 Phase-Field Regularization of Fracture

Consider a one-dimensional body $\mathcal{B}$ along x axis with a crack at $x = a$. We define a scalar damage variable d that equals zero for undamaged state and one for cracked state. To smooth out the discontinuous damage field we can approximate d by a sine function as in [64]

$$d(x) = 1 - \sin(|x - a| / l) \quad \text{for} \quad -D_u \leq x \leq D_u, \tag{4.1}$$

where $D_u = \pi l/2$ is the ultimate half crack bandwidth. This is the solution of the following differential equation

$$1 - d - l^2 \frac{d^2 d}{dx^2} = 0 \quad \text{in} \quad \mathcal{B} \quad \text{with} \quad d = 1 \quad \text{at} \quad x = a \tag{4.2}$$

Variation of d along x axis for both sharp representation and the regularized sine form with different values of l are shown in Figures 4.1 (a) and (b). Now, let's consider a

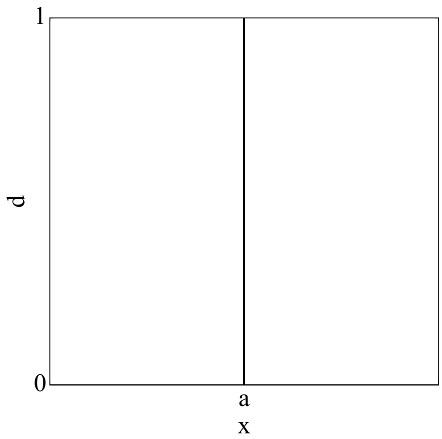

(a)

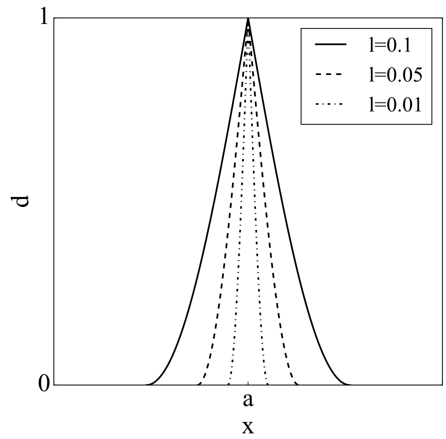

(b)

Figure 4.1: Phase-field approximation of a one-dimensional domain with (a) a sharp crack at $x = a$, (b) the phase-field approximations for different values of l

cracked body $\mathcal{B} \subset \mathbb{R}^D$ with boundary $\partial\mathcal{B}$ and the crack surface Γ where $\mathbb{R}^D$ denotes the D-dimensional space. The governing equation (4.2) can be extended to higher dimensions as

$$\begin{aligned} 1 - d - l^2 \nabla^2 d = 0 \quad & \text{in} \quad \mathcal{B} \\ d = 1 \quad & \text{on} \quad \Gamma \\ \nabla d \cdot \boldsymbol{n} = 0 \quad & \text{on} \quad \partial\mathcal{B}, \end{aligned} \tag{4.3}$$

The length scale parameter l controls the width of the smeared crack and $\boldsymbol{n}$ denotes the outward unit normal to the boundary $\partial\mathcal{B}$. Smaller values of l give a more accurate representation of the crack and for $l \to 0$ a sharp crack is achieved. The above-introduced boundary value problem (4.3) is the Euler equation of the minimization problem

$$d = \text{Arg}\{\inf_{d \in S_d} \Gamma_l(d)\}, \tag{4.4}$$

where $S_d = \{d \mid d(\boldsymbol{x}, t) = 1 \quad \forall \boldsymbol{x} \in \Gamma\}$.

$$\Gamma_l(d) = \int_{\mathcal{B}} \gamma(d, \nabla d) dV \tag{4.5}$$

represents the crack surface with $\gamma(d, \nabla d)$ being the crack surface density as

$$\gamma(d, \nabla d) = \frac{1}{\pi l}(2d - d^2) + \frac{l}{\pi}|\nabla d|^2. \tag{4.6}$$

In Figure 4.2, numerical solutions for the boundary value problem (4.3) for a two-dimensional square plate of unit sides with an edge crack for different length scales l are given.

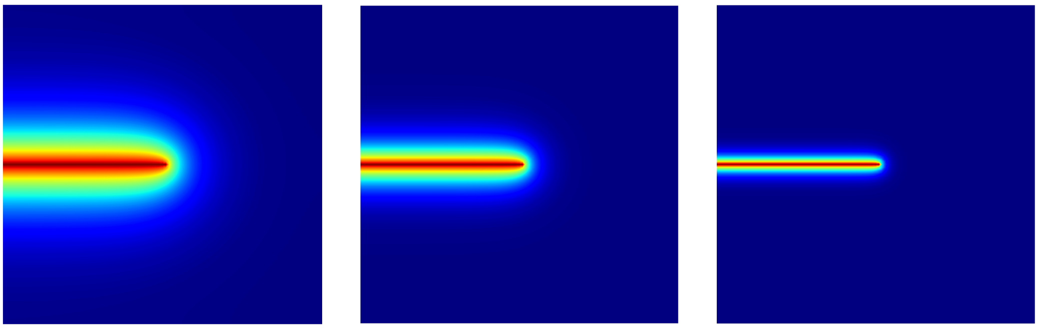

(a) (b) (c)

Figure 4.2: Phase-field approximation of a two-dimensional domain with a crack for different values of l (a) $l = 0.1$ (b) $l = 0.05$ (c) $l = 0.02$

4.1.1.1 Comparison with Common Exponential Regularization

A common regularization used widely in the Phase-Field models for brittle fracture is the exponential approximation [52]

$$d(x) = \exp(-|x - a|/l) \tag{4.7}$$

This is the solution of the following differential equation

$$d - l^2 \frac{d^2 d}{dx^2} = 0 \quad \text{in} \quad \mathcal{B} \quad \text{with} \quad d = 1 \quad \text{at} \quad x = a. \tag{4.8}$$

Extension of the above equation to the three dimension reads

$$\begin{aligned} d - l^2 \nabla^2 d &= 0 \quad \text{in} \quad \mathcal{B} \\ d &= 1 \quad \text{on} \quad \Gamma \\ \nabla d \cdot \boldsymbol{n} &= 0 \quad \text{on} \quad \partial\mathcal{B}, \end{aligned} \tag{4.9}$$

which results in a crack surface density of the form

$$\gamma(d, \nabla d) = \frac{1}{2l}d^2 + \frac{l}{2}|\nabla d|^2. \tag{4.10}$$

Variation of d along x axis for both sharp representation and the regularized exponential form with different values of l are shown in Figures 4.3 (a) and (b) for one-dimensional domain with a crack at $x = a$. Comparing Figures 4.1 and 4.3, one

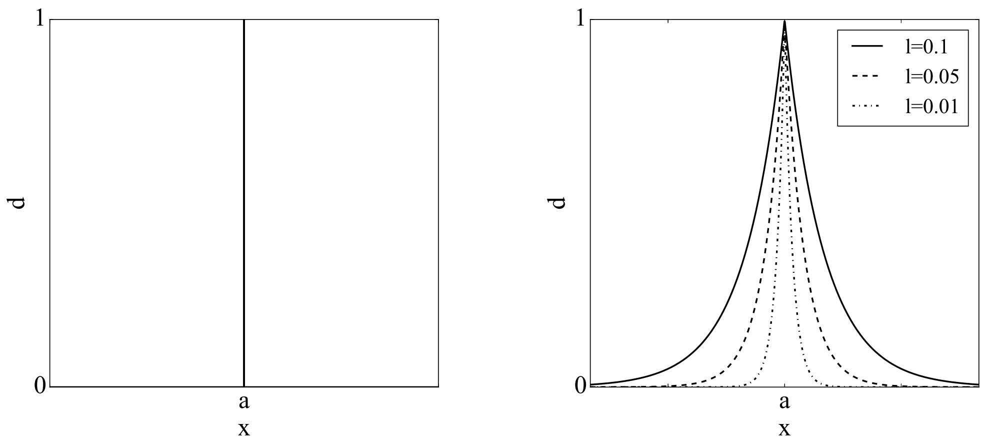

(a) (b)

Figure 4.3: Phase-field approximation of a one-dimensional domain for exponential regularization

immediate advantage of the new sine regularization over the exponential one can be seen, i.e. the new sine model gives a better localized representation of fracture. Also, as will be seen in the following sections, the crack geometry given by the expression (4.6) provides the capability of incorporating the tensile strength of the material into the model, whereas the crack density function (4.10) gives a zero tensile strength. This has two main consequences. One is that in the new sine model, damaging starts after stresses reaching the tensile strength, while in the exponential model damage starts from the very beginning of loading. Another consequence is that the material response in the sine model is independent of the length scale l. This means that the new model is fully capable of realistic modeling of material behavior. This is a great advantage over the old exponential model, in which the material behavior depends heavily on the length scale.

4.1.2 Variational Approach to Fracture

Total energy of a cracked body can be written as [65, 36]

$$E(\boldsymbol{u}, d) = E_e(\boldsymbol{u}, d) + E_f(d), \tag{4.11}$$

in which E_e represents the elastic energy stored in the bulk body and E_f is the fracture energy. Assuming an isotropic linear elastic behavior for the material, the elastic energy stored in the body E_e in (4.11) can be expressed as

$$E_e(\boldsymbol{u}, d) = \int_{\mathcal{B}} \psi(\boldsymbol{\varepsilon}(\boldsymbol{u}), d) dV, \tag{4.12}$$

with the free energy density ψ defined as

$$\psi(\boldsymbol{\varepsilon}, d) = g(d)\psi_0(\boldsymbol{\varepsilon}) \tag{4.13}$$

for isotropic damage, with ψ_0 being the free energy of intact material. However, compressive strength of brittle materials like concrete is much greater than their tensile strength, and damage occurs only in tension. So, we decompose the energy into compressive and tensile parts and require the damage to grow only in tension. Also, assuming the damaged zones are able to carry compressive loads, we only degrade the tensile energy

$$\psi(\boldsymbol{\varepsilon}, d) = g(d)\psi_0^+(\boldsymbol{\varepsilon}) + \psi_0^-(\boldsymbol{\varepsilon}), \tag{4.14}$$

where ψ_0^+ and ψ_0^- represent tensile and compressive parts of the free energy, respectively. $g(d)$ is the degradation function. For an unbroken state we have $\psi = \psi_0$ and for a fully broken state the identity $\psi = \psi_0^-$ holds since all tensile energy is released. Therefore, we need a degradation function such that: $g(0) = 1$ and $g(1) = 0$.

For a given phase-field regularized crack geometry $\Gamma(d)$ with the crack surface density $\gamma(d, \nabla d)$, the total fracture energy E_f in (4.11) can be written as

$$E_f(d) = \int_{\mathcal{B}} g_f \gamma(d, \nabla d) dV, \tag{4.15}$$

where g_f is Griffith's critical energy release rate.
Substituting E_e and E_f from (4.12) and (4.15) into (4.11) we get the total energy for the phase-field model

$$E_l(\boldsymbol{\varepsilon}, d, \nabla d) = \int_{\mathcal{B}} \psi(\boldsymbol{\varepsilon}, d) dV + \int_{\mathcal{B}} g_f \gamma(d, \nabla d) dV. \tag{4.16}$$

In the variational approach, it is assumed that the total potential energy needs to be minimized at any time during loading [36]. The total potential energy is the sum of the internal stored energy and the work done by external loads. So, adding the external potential to the energy in (4.16) we get the total potential Π as

$$\Pi(\boldsymbol{\varepsilon}, d, \nabla d) = \int_{\mathcal{B}} \psi(\boldsymbol{\varepsilon}, d) dV + \int_{\mathcal{B}} g_f \gamma(d, \nabla d) dV - \int_{\mathcal{B}} \boldsymbol{b} \cdot \boldsymbol{u}\, dV - \int_{\partial\mathcal{B}} \boldsymbol{t} \cdot \boldsymbol{u}\, dA \quad (4.17)$$

So, in order to minimize the total potential energy Π in (4.17), we set its variation to zero

$$\begin{aligned} \delta\Pi(\boldsymbol{\varepsilon}, d, \nabla d) = & \int_{\mathcal{B}} \left(\frac{\partial\psi}{\partial\boldsymbol{\varepsilon}} : \delta\boldsymbol{\varepsilon} + \frac{\partial\psi}{\partial d}\delta d\right) dV \\ & + \int_{\mathcal{B}} g_f \left(\frac{\partial\gamma}{\partial d}\delta d + \frac{\partial\gamma}{\partial\nabla d} \cdot \delta\nabla d\right) dV \\ & - \int_{\mathcal{B}} \boldsymbol{b} \cdot \delta\boldsymbol{u}\, dV - \int_{\partial\mathcal{B}} \boldsymbol{t} \cdot \delta\boldsymbol{u}\, dA = 0, \end{aligned} \quad (4.18)$$

where $\boldsymbol{b}$ is the body force and $\boldsymbol{t}$ is the traction acting upon the boundary. Performing integration by parts using relations $\boldsymbol{\sigma} : \delta\boldsymbol{\varepsilon} = \mathrm{div}(\boldsymbol{\sigma}\delta\boldsymbol{u}) - \mathrm{div}(\boldsymbol{\sigma}) \cdot \delta\boldsymbol{u}$ and $\nabla d \cdot \delta\nabla d = \mathrm{div}(\delta d \nabla d) - \nabla^2 d \delta d$, and also using the Gauss integral theorem, we end up with

$$\begin{aligned} \delta\Pi(\boldsymbol{\varepsilon}, d, \nabla d) = & -\int_{\mathcal{B}} [\mathrm{div}(\boldsymbol{\sigma}) + \boldsymbol{b}] \cdot \delta\boldsymbol{u}\, dV + \int_{\partial\mathcal{B}} (\boldsymbol{\sigma}\boldsymbol{n} - \boldsymbol{t}) \cdot \delta\boldsymbol{u}\, dA \\ & + \int_{\mathcal{B}} \left[\frac{2g_f}{\pi l}(1-d) - \frac{2g_f l}{\pi}\nabla^2 d + g'(d)\psi_0^+\right] \delta d\, dV \\ & + l \int_{\partial\mathcal{B}} (\nabla d \cdot \boldsymbol{n}) \delta d\, dA = 0. \end{aligned} \quad (4.19)$$

For arbitrary $\delta\boldsymbol{u}$ and δd, we get the governing differential equations from the volume integrals in (4.19) as

$$\mathrm{div}\,(\boldsymbol{\sigma}) + \boldsymbol{b} = \boldsymbol{0}, \quad (4.20)$$

$$\frac{2g_f}{\pi l}(1 - d - l^2\nabla^2 d) + g'(d)\psi_0^+ = 0, \quad (4.21)$$

The surface integrals in (4.19) gives the natural boundary conditions as

$$\boldsymbol{\sigma}\boldsymbol{n} = \boldsymbol{t} \quad \text{on} \quad \partial\mathcal{B} \quad (4.22)$$

$$\nabla d \cdot \boldsymbol{n} = 0 \quad \text{on} \quad \partial\mathcal{B} \quad (4.23)$$

where the stress tensor definition $\boldsymbol{\sigma} := \partial\psi/\partial\boldsymbol{\varepsilon}$ is used. As it is seen in (4.21), the term $g'(d)\psi_0^+$ acts as a thermodynamic driving force for damage evolution. Further requirements for the degradation function can be deduced here. In order for the damage to grow from an unbroken state we require $g'(0) < 0$ so that the driving force is greater than zero. Also, to ensure that damage stops growing further after reaching the fully broke state, the driving force needs to be zero when $d = 1$. So, it is needed that $g'(1) = 0$. Following Wu [64], the degradation function $g(d)$ is chosen as below, which satisfies all the requirements and provides the flexibility to achieve the desired cohesive behavior.

$$g(d) = \frac{1}{1+\phi(d)} = \frac{(1-d)^p}{(1-d)^p + Q(d)}, \tag{4.24}$$

where $\phi(d)$ and $Q(d)$ are as below

$$\phi(d) = \frac{Q(d)}{(1-d)^p} \tag{4.25}$$

$$Q(d) = a_1 d + a_1 a_2 d^2 + a_1 a_2 a_3 d^3 \tag{4.26}$$

In the following section the parameters p, a_1, a_2, and a_3 are determined for any desired cohesive behavior.

4.1.2.1 The Exponential Model

For the exponential regularization of the crack surface the governing differential equation for damage evolution takes the following form.

$$\frac{g_f}{l}(d - l^2\nabla^2 d) + g'(d)\psi_0^+ = 0 \tag{4.27}$$

As mentioned before, one disadvantage of this model is that the results are dependent on the length scale parameter l. This is apparent in the above equation. Obviously using a smaller length scale l is equivalent to using a larger fracture energy g_f, and thus it results in a tougher material response. A remedy has been proposed in [66] through simple modifications to the evolution equation, such as the following

$$d - l^2\nabla^2 d = (1-d)\zeta < \sum_{i=1}^{3}(\frac{<\sigma_0^i>_+}{f_t})^2 - 1 >_+, \tag{4.28}$$

where $< x >_+$ is defined as $< x >_+ = (x + |x|)/2$, and σ_0^i is the $i\text{th}$ elastic principal stress. As it can be seen the equation is mainly the same with only a different driving function. Using $< \sigma_0^i >_+$ in the driving function provides an alternative way to accommodate tension-compression splitting. the main part of the driving function $< \sum_{i=1}^{3}(\frac{< \sigma_0^i >_+}{f_t})^2 - 1 >_+$ provides a threshold so that damage can only evolve when a failure criterion is satisfied, i.e. when $\sum_{i=1}^{3}(\frac{< \sigma_0^i >_+}{f_t})^2 - 1 > 0$. The coefficient ζ is used to magnify the driving force, so that damage evolve rapidly as soon as the failure criterion is met. Therefore ζ must be large enough. The modified model removes the dependency of the results on the length scale l, however the model is still restricted to ideally brittle behavior. On the contrary, the new sine model of Wu [64] is capable of modeling brittle as well as cohesive fracture, which will be shown through the numerical examples of Chapter 5.

4.1.2.2 Alternative Tension-Compression Splitting Scheme

Similar to the modified equation (4.28) for the exponential model, Wu [64] proposed a driving function as given below

$$y = \frac{\sigma_{eq}^2}{2E}, \quad \sigma_{eq} = \frac{1}{1+\beta_c}(\beta_c < \max(\sigma_0^{\mathrm{i}}) >_+ + \sqrt{3\mathrm{J}_2}), \tag{4.29}$$

in which J_2 denotes the second invariant of the deviatoric stress tensor, and $\beta_c = f_c/f_t - 1$ with the ratio of uniaxial compressive strength to tensile strength f_c/f_t. He used this modified energy instead of ψ_0^+ in (4.21).

4.1.3 Determination of Parameters for Cohesive Fracture

Here, a one-dimensional problem is used to determine the parameters for a softening behavior. Finding relations for the stress and crack opening, we can use maximum crack opening, tensile strength, and initial slope of the softening curve for a specific cohesive law to determine the unknown parameters [64]. Consider a bar of length $2L$ with a crack at $x = 0$. The bar is subjected to displacement u in opposite directions at both ends. For a linear elastic behavior, from (4.21) we can write

$$\frac{2g_f}{\pi l}(1 - d - l^2\frac{\partial^2 d}{\partial x^2}) + g'(d)\frac{\sigma_0^2}{2E} = 0, \tag{4.30}$$

Using the relations $\sigma = g(d)\sigma_0$ and $g(d) = \dfrac{1}{1+\phi(d)}$ it can be rewritten as

$$\frac{2g_f}{\pi l}(1 - d - l^2\frac{\partial^2 d}{\partial x^2}) - \phi'(d)\frac{\sigma^2}{2E} = 0, \tag{4.31}$$

Multiplying the above by $\partial d/\partial x$ and integrating from $x = 0$ to $x = L$, knowing that $d(x = L) = \dfrac{\partial d}{\partial x}|_{x=L} = 0$,and $\phi(x = L) = \phi(d = 0) = 0$ we have:

$$\frac{g_f}{\pi l}[2d - d^2 - (l\frac{\partial d}{\partial x})^2] - \phi(d)\frac{\sigma^2}{2E} = 0, \tag{4.32}$$

For a given displacement u^*, d attains its maximum value d^* at $x = 0$. Also, $\dfrac{\partial d}{\partial x}|_{x=0} = 0$, so the stress can be written by evaluating (4.32) at $x = 0$ as below:

$$\sigma = \sqrt{\frac{2Eg_f}{\pi l}\frac{2d^* - {d^*}^2}{\phi(d^*)}} \tag{4.33}$$

So, we have a relation for stress. Evaluating the stress at the onset of damage yields the tensile strength f_t, so we have:

$$f_t = \lim_{d^*\to 0} \sigma = \lim_{d^*\to 0} \sqrt{\frac{2Eg_f}{\pi l}\frac{2d^* - {d^*}^2}{\phi(d^*)}} = \sqrt{\frac{4Eg_f}{\pi l a_1}} \tag{4.34}$$

Using the stress-strain constitutive equation we can find a relation for the crack opening w as follows. The stress-strain relation for the one-dimensional bar reads

$$\sigma = g(d)E\varepsilon \tag{4.35}$$

So, for ε we can write

$$\varepsilon = \frac{\sigma}{E}\frac{1}{g(d)}. \tag{4.36}$$

Integrating the strain from 0 to L gives us the displacement at the end of the bar

$$u = \int_0^L \varepsilon\, dx = \frac{\sigma}{E}\int_0^L \frac{1}{g(d)}\, dx = \frac{\sigma}{E}[L + \int_0^L \phi(d)]\, dx = \frac{\sigma}{E}L + \frac{w}{2}, \tag{4.37}$$

where w is the displacement jump. So, w can be written as

$$w = \frac{2\sigma}{E}\int_0^L \phi(d)\, dx \tag{4.38}$$

Inserting (4.33) into (4.32), $\partial d/\partial x$ is determined as

$$\frac{\partial d}{\partial x} = -\frac{1}{l}\sqrt{2d - d^2 - \frac{2d^* - {d^*}^2}{\phi(d^*)}\phi(d)}. \tag{4.39}$$

Using (4.39) for changing integration variable from x to d in (4.38), the displacement jump w can be rewritten as below

$$w = \frac{2\sigma}{E}\int_0^{d^*} \frac{l\phi(\beta)}{\sqrt{2\beta - \beta^2 - \dfrac{2d^* - d^{*2}}{\phi(d^*)}\phi(\beta)}}\, d\beta \tag{4.40}$$

Using relations (4.40) and (4.33) we can find the maximum jump w_c and the initial slope k_0 through the following

$$w_c = \lim_{d^* \to 1} w(d^*), \tag{4.41}$$

$$k_0 = \lim_{d^* \to 0} \frac{\partial \sigma}{\partial w}. \tag{4.42}$$

The evaluation of the above expressions results in

$$w_c = \begin{cases} 0 & p < 2 \\ \dfrac{2g_f}{f_t}\sqrt{2(1 + a_2 + a_2 a_3)} & p = 2 \\ +\infty & p > 2 \end{cases}, \tag{4.43}$$

$$k_0 = -\frac{f_t^2}{16 g_f}(2a_2 + 2p + 1)^{3/2}. \tag{4.44}$$

Consequently, a_1, a_2, and a_3 are determined from (4.34), (4.43), and (4.44)

$$a_1 = \frac{4Eg_f}{\pi l f_t^2} \tag{4.45}$$

$$a_2 = \frac{1}{2}[(-\frac{16 g_f k_0}{f_t^2})^{2/3} + 1] - (p + 1) \tag{4.46}$$

$$a_3 = \begin{cases} 0 & p > 2 \\ \dfrac{1}{a_2}[\dfrac{1}{2}(\dfrac{w_c f_t}{2g_f})^2 - (1 + a_2)] & p = 2 \end{cases} \tag{4.47}$$

4.1.3.1 Cohesive Fracture models

Here for some common cohesive laws, we determine the corresponding degradation function and compare the resulting approximated softening with the original ones.

Linear Softening

The linear cohesive law can be expressed as:

$$\sigma(w) = f_t \max(1 - \frac{f_t}{2g_f} w, 0). \tag{4.48}$$

So, for the initial slope k_0 and the ultimate crack opening w_c we have

$$k_0 = -\frac{f_t^2}{2g_f}, \quad w_c = \frac{2g_f}{f_t} \tag{4.49}$$

Substituting the above into equations (4.46) and (4.47), we obtain

$$p = 2, \quad a_2 = -\frac{1}{2}, \quad a_3 = 0. \tag{4.50}$$

The resulting softening curve is shown in Figure 4.4.

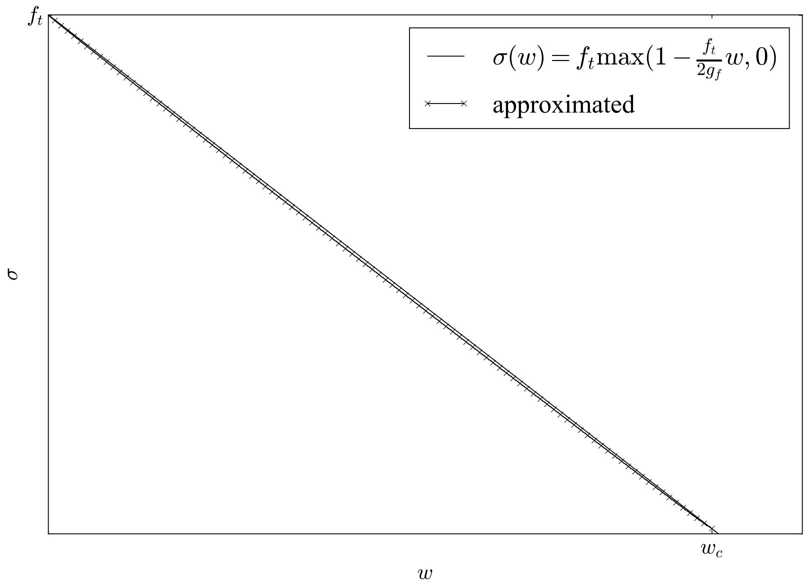

Figure 4.4: Linear softening

Exponential Softening

The exponential softening law reads

$$\sigma(w) = f_t \exp(-\frac{f_t}{g_f} w) \tag{4.51}$$

Therefore, the initial slope k_0 and ultimate crack opening w_c are found as

$$k_0 = -\frac{f_t^2}{g_f}, \quad w_c = \infty \tag{4.52}$$

Choosing $p = 5/2$, equations (4.46) and (4.47) yield

$$a_2 = 2^{5/3} - 3 \approx 0.1748, \quad a_3 = 0. \tag{4.53}$$

The approximated softening curve is shown in Figure 4.5.

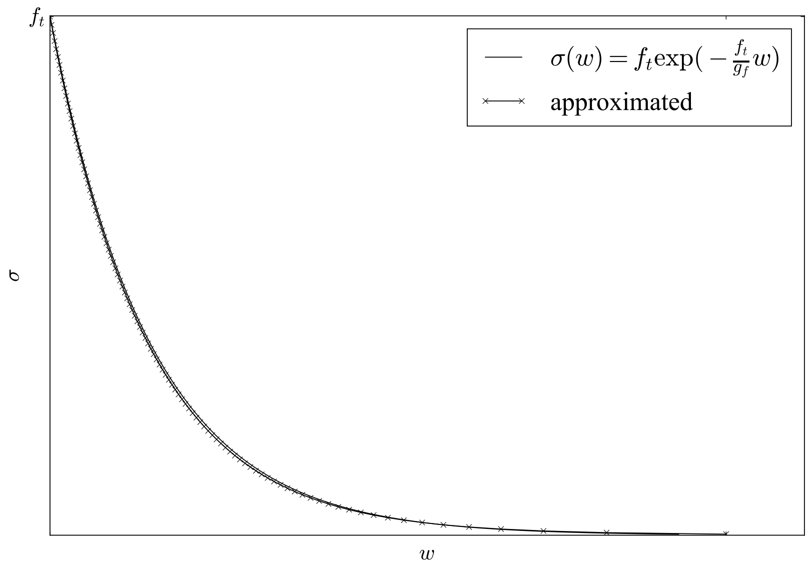

Figure 4.5: Exponential softening

Cornelissen's Softening

The softening law proposed by Cornelissen et al. [67] for concrete is expressed as

$$\sigma(w) = f_t[(1.0 + \eta_1^3 r^3)\exp(-\eta_2 r) - r(1.0 + \eta_1^3)\exp(-\eta_2)], \tag{4.54}$$

where $r := w/w_c$ is the normalized crack opening. For typical values of $\eta_1 = 3.0$ and $\eta_2 = 6.93$ for concrete we have

$$k_0 = -1.3546\frac{f_t^2}{g_f}, \quad w_c = 5.1361\frac{g_f}{f_t} \tag{4.55}$$

So, the expressions (4.46) and (4.47) result in

$$p = 2, \quad a_2 = 1.3868, \quad a_3 = 0.6567. \tag{4.56}$$

The resulting softening curve is shown in Figure 4.6.

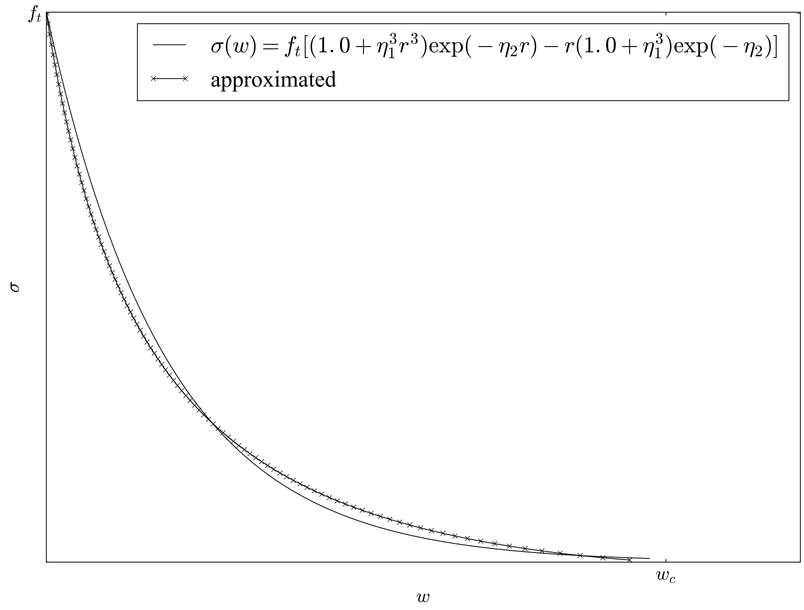

Figure 4.6: Cornelissen's softening

4.1.4 Crack Irreversibility

Since cracks cannot heal in the absence of particular agents designed for this purpose, we need to make sure that they can only grow. Therefore, it is required that

$$\dot{\gamma} = \delta_d \gamma(d, \nabla d)\dot{d} \geq 0. \tag{4.57}$$

From equation (4.18) we have

$$\frac{\partial \psi(\boldsymbol{\varepsilon}, d)}{\partial d} + g_f \delta_d \gamma(d, \nabla d) = 0, \tag{4.58}$$

If $\dot{d} = 0$ then from equation (4.57) we have $\dot{\gamma} = 0$. This means there is no crack growth. Now, if $\dot{d} \neq 0$ from equation (4.58) we get $\delta_d \gamma = -g'(d)\psi_0^+ / g_f \geq 0$. Therefore, from equation (4.57) it is required that $\dot{d} > 0$. Consequently, it can be written

$$\dot{d} \geq 0, \tag{4.59}$$

which means the damage variable d must grow to ensure irreversible crack propagation. From (4.21), the driving function for evolution of d is $-g'(d)\psi_0^+$. With increasing ψ_0^+ damage grows. However, if ψ_0^+ drops damage is going to reverse. Therefore using a history term of maximum energy at all steps ensures irreversible damage evolution [53]

$$\mathcal{H}(\boldsymbol{\varepsilon}(\boldsymbol{x},t)) = \max\{\psi_0^+(\boldsymbol{\varepsilon}(\boldsymbol{x},\tau)) \mid \tau \in [0,t]\} \tag{4.60}$$

Substituting ψ_0^+ in equation (4.21) with $\mathcal{H}(\boldsymbol{\varepsilon})$ from (4.60) we end up with

$$\frac{2g_f}{\pi l}(1 - d - l^2\nabla^2 d) + g'(d)\mathcal{H}(\boldsymbol{\varepsilon}) = 0. \tag{4.61}$$

4.2 Finite Element Formulation

Considering the displacement vector $\boldsymbol{u}$ and the damage variable d as primary unknown fields of the problem, and with their virtual counterparts $\delta\boldsymbol{u}$ and δd, we formulate the weak forms of the governing differential equations using the Galerkin Method. For (4.20) we can write

$$G^u(\delta\boldsymbol{u},\boldsymbol{u},d) = \int_{\mathcal{B}} \delta\boldsymbol{u}\cdot[\mathrm{div}\,(\boldsymbol{\sigma}) + \boldsymbol{b}]\,dV = 0 \tag{4.62}$$

Through integration by parts using $\delta\boldsymbol{u}\cdot\mathrm{div}\,(\boldsymbol{\sigma}) = \mathrm{div}\,(\delta\boldsymbol{u}\boldsymbol{\sigma}) - \delta\boldsymbol{\varepsilon} : \boldsymbol{\sigma}$ and using the Gauss theorem $\int_{\mathcal{B}} \mathrm{div}\,(\delta\boldsymbol{u}\boldsymbol{\sigma})\,dV = \int_{\partial\mathcal{B}} \delta\boldsymbol{u}\boldsymbol{\sigma}\cdot\boldsymbol{n}\,dA$ knowing $\boldsymbol{\sigma}\cdot\boldsymbol{n} = \boldsymbol{t}$, we end up with

$$G^u(\delta\boldsymbol{u},\boldsymbol{u},d) = \int_{\mathcal{B}} (\delta\boldsymbol{\varepsilon} : \boldsymbol{\sigma} - \delta\boldsymbol{u}\cdot\boldsymbol{b})\ dV - \int_{\partial\mathcal{B}_t} \delta\boldsymbol{u}\cdot\boldsymbol{t}\ dA = 0. \tag{4.63}$$

Similarly for Equation (4.61) we have

$$G^d(\delta d,\boldsymbol{u},d) = \int_{\mathcal{B}} \delta d[\frac{2g_f}{\pi l}(1 - d - l^2\nabla^2 d) + g'(d)\mathcal{H}(\boldsymbol{\varepsilon})]\,dV = 0 \tag{4.64}$$

Again integrating by parts using $\delta d\nabla^2 d = \mathrm{div}\,(\delta d\nabla d) - \nabla(\delta d)\cdot\nabla d$ and using the Gauss theorem knowing that $\nabla d\cdot\boldsymbol{n} = 0$ on $\partial\mathcal{B}$ we obtain

$$G^d(\delta d,\boldsymbol{u},d) = \int_{\mathcal{B}} \{\frac{2g_f}{\pi} l\nabla\delta d\cdot\nabla d + \delta d[\frac{2g_f}{\pi l}(1-d) - 2(1-d)\mathcal{H}(\boldsymbol{\varepsilon})]\}\ dV = 0 \tag{4.65}$$

The weak forms (4.63) and (4.65) are coupled nonlinear equations. So, before Finite Element discretization, we linearize them as follows

$$\mathrm{Lin}\,G^u(\delta\boldsymbol{u},\boldsymbol{u},d)|_{\tilde{\boldsymbol{u}},\tilde{d}} = G^u(\delta\boldsymbol{u},\tilde{\boldsymbol{u}},\tilde{d}) + \Delta G^u(\delta\boldsymbol{u},\tilde{\boldsymbol{u}},\tilde{d};\Delta\boldsymbol{u},\Delta d) = 0 \tag{4.66}$$

$$\mathrm{Lin}\,G^d(\delta d,\boldsymbol{u},d)\big|_{\tilde{\boldsymbol{u}},\tilde{d}} = G^d(\delta d,\tilde{\boldsymbol{u}},\tilde{d}) + \Delta G^d(\delta d,\tilde{\boldsymbol{u}},\tilde{d};\Delta\boldsymbol{u},\Delta d) = 0 \tag{4.67}$$

The incremental terms ΔG^u and ΔG^d are derived using the Gâteaux derivative. For ΔG^u we have

$$\Delta G^u = \int_{\mathcal{B}} (\delta \boldsymbol{\varepsilon} : \mathbb{C}^{uu} : \Delta \boldsymbol{\varepsilon} + \delta \boldsymbol{\varepsilon} : \boldsymbol{C}^{ud} \Delta d) \ dV, \tag{4.68}$$

in which tangents $\mathbb{C}^{uu}$ and $\boldsymbol{C}^{ud}$ are defined as

$$\mathbb{C}^{uu} := \frac{\partial \boldsymbol{\sigma}}{\partial \boldsymbol{\varepsilon}} \quad \text{and} \quad \boldsymbol{C}^{ud} := \frac{\partial \boldsymbol{\sigma}}{\partial d}. \tag{4.69}$$

For ΔG^d we have

$$\Delta G^d = \int_{\mathcal{B}} \left[\frac{2g_f}{\pi} l \nabla(\delta d) \Delta(\nabla d) + \delta d \left(-\frac{2g_f}{\pi l} + g''(d) \mathcal{H}(\boldsymbol{\varepsilon}) \right) \Delta d \right] \ dV \tag{4.70}$$

Now, we discretize the whole domain $\mathcal{B}$ into finite elements of volume $\mathcal{B}_e^h$. In each element domain $\mathcal{B}_e^h$ the displacements $\boldsymbol{u}$ and damage variable d and their virtual counterparts, $\delta \boldsymbol{u}$ and δd, are approximated using the Finite Element interpolations as

$$\boldsymbol{u}_e^h = \sum_{i=1}^{n_{en}} \boldsymbol{N}_i^u \boldsymbol{U}_i^e , \quad d_e^h = \sum_{i=1}^{n_{en}} N_i^d d_i^e \tag{4.71}$$

$$\delta \boldsymbol{u}_e^h = \sum_{i=1}^{n_{en}} \boldsymbol{N}_i^u \delta \boldsymbol{U}_i^e , \quad \delta d_e^h = \sum_{i=1}^{n_{en}} N_i^d \delta d_i^e \tag{4.72}$$

where n_{en} is the number of nodes per element, d_i^e is the element damage variable at node i and N_i^d is the corresponding shape function. $\boldsymbol{U}_i^e$ and $\delta \boldsymbol{U}_i^e$ are vectors of displacements and their virtual counterparts, and $\boldsymbol{N}_i^u$ is the corresponding matrix of shape functions all associated with node i. For a two-dimensional problem we have

$$\boldsymbol{U}_i^e = \begin{bmatrix} u_1^e \\ u_2^e \end{bmatrix} , \quad \delta \boldsymbol{U}_i^e = \begin{bmatrix} \delta u_1^e \\ \delta u_2^e \end{bmatrix} , \quad \boldsymbol{N}_i^u = \begin{bmatrix} N_i^u & 0 \\ 0 & N_i^u \end{bmatrix} \tag{4.73}$$

The strains $\boldsymbol{\varepsilon} = \mathrm{sym}(\nabla \boldsymbol{u})$ and gradient of damage variable ∇d as well as their virtual counterparts $\delta \boldsymbol{\varepsilon}$ and $\nabla(\delta d)$ are therefore approximated by the following interpolations:

$$\boldsymbol{\varepsilon}_e^h = \sum_{i=1}^{n_{en}} \boldsymbol{B}_i^u \boldsymbol{U}_i^e , \quad \nabla d_e^h = \sum_{i=1}^{n_{en}} \boldsymbol{B}_i^d d_i^e \tag{4.74}$$

$$\delta \boldsymbol{\varepsilon}_e^h = \sum_{i=1}^{n_{en}} \boldsymbol{B}_i^u \delta \boldsymbol{U}_i^e , \quad \nabla(\delta d)_e^h = \sum_{i=1}^{n_{en}} \boldsymbol{B}_i^d \delta d_i^e \tag{4.75}$$

where $\boldsymbol{B}_i^u$ and $\boldsymbol{B}_i^d$ are matrices of shape function derivatives associated with node i, which for a two-dimensional problem are defined as

$$\boldsymbol{B}_i^u = \begin{bmatrix} \frac{\partial N_i^u}{\partial x_1} & 0 \\ 0 & \frac{\partial N_i^u}{\partial x_2} \\ \frac{\partial N_i^u}{\partial x_2} & \frac{\partial N_i^u}{\partial x_1} \end{bmatrix}, \quad \boldsymbol{B}_i^d = \begin{bmatrix} \frac{\partial N_i^d}{\partial x_1} \\ \frac{\partial N_i^d}{\partial x_2} \end{bmatrix} \tag{4.76}$$

Substituting the Finite Element discretizations (4.71), (4.72), (4.74), and (4.75) into the linearized weak forms (4.66) and (4.67) and assembling for all elements results in the following system of iterative equations

$$\begin{bmatrix} \tilde{\boldsymbol{R}}^u \\ \tilde{\boldsymbol{R}}^d \end{bmatrix} + \begin{bmatrix} \tilde{\boldsymbol{K}}^{uu} & \tilde{\boldsymbol{K}}^{ud} \\ \tilde{\boldsymbol{K}}^{du} & \tilde{\boldsymbol{K}}^{dd} \end{bmatrix} \begin{bmatrix} \Delta \boldsymbol{U} \\ \Delta \boldsymbol{D} \end{bmatrix} = \begin{bmatrix} \boldsymbol{0} \\ \boldsymbol{0} \end{bmatrix} \tag{4.77}$$

where $\Delta \boldsymbol{U} = \boldsymbol{U} - \tilde{\boldsymbol{U}}$, and $\Delta \boldsymbol{D} = \boldsymbol{D} - \tilde{\boldsymbol{D}}$, in which $\tilde{\boldsymbol{U}}$ and $\tilde{\boldsymbol{D}}$ are the values of the global vectors $\boldsymbol{U}$ and $\boldsymbol{D}$ from the previous iteration. $\tilde{\boldsymbol{R}}^u$ and $\tilde{\boldsymbol{R}}^d$ are the values of global residual vectors $\boldsymbol{R}^u$ and $\boldsymbol{R}^d$ evaluated at previous iterations $\tilde{\boldsymbol{U}}$ and $\tilde{\boldsymbol{D}}$. Also, $\tilde{\boldsymbol{K}}^{uu}$, $\tilde{\boldsymbol{K}}^{ud}$, $\tilde{\boldsymbol{K}}^{du}$, and $\tilde{\boldsymbol{K}}^{dd}$ are the values of global stiffness matrices $\boldsymbol{K}^{uu}$, $\boldsymbol{K}^{ud}$, $\boldsymbol{K}^{du}$, and $\boldsymbol{K}^{dd}$ evaluated at previous iterations $\tilde{\boldsymbol{U}}$ and $\tilde{\boldsymbol{D}}$. The aforementioned global residual vectors and stiffness matrices are defined as below

$$\boldsymbol{R}_I^u = \mathop{\mathsf{A}}_{e=1}^{n_{el}} \left\{ \int_{\mathcal{B}_e^h} \left(\boldsymbol{B}_i^{uT} \boldsymbol{\sigma} - \boldsymbol{N}_i^{uT} \boldsymbol{b} \right) \, dV - \int_{\partial \mathcal{B}_t^e} \boldsymbol{N}_i^{eT} \boldsymbol{t} \, dA \right\} \tag{4.78}$$

$$R_J^d = \mathop{\mathsf{A}}_{e=1}^{n_{el}} \left\{ \int_{\mathcal{B}_e^h} \left\{ \frac{2 g_f}{\pi} l \boldsymbol{B}_j^{dT} \nabla d + N_j^{dT} \left[\frac{2 g_f}{\pi l} (1-d) + g'(d) \mathcal{H} \right] \right\} \, dV \right\} \tag{4.79}$$

$$\boldsymbol{K}_{IJ}^{uu} = \mathop{\mathsf{A}}_{e=1}^{n_{el}} \left\{ \int_{\mathcal{B}_e^h} \boldsymbol{B}_i^{uT} \mathbb{C}^{uu} \boldsymbol{B}_j^u \, dV \right\} \tag{4.80}$$

$$\boldsymbol{K}_{IL}^{ud} = \mathop{\mathsf{A}}_{e=1}^{n_{el}} \left\{ \int_{\mathcal{B}_e^h} \boldsymbol{B}_i^{uT} \boldsymbol{C}^{ud} N_l^d \, dV \right\} \tag{4.81}$$

$$\boldsymbol{K}_{KJ}^{du} = \mathop{\mathsf{A}}_{e=1}^{n_{el}} \left\{ \int_{\mathcal{B}_e^h} g'(d) c N_k^{dT} \boldsymbol{\sigma}_0 \boldsymbol{B}_j^u \, dV \right\} \tag{4.82}$$

$$K_{KL}^{dd} = \mathop{\mathsf{A}}_{e=1}^{n_{el}} \left\{ \int_{\mathcal{B}_e^h} \left[\frac{2 g_f}{\pi} l \boldsymbol{B}_k^{dT} \boldsymbol{B}_l^d + \left(-\frac{2 g_f}{\pi l} + g''(d) \mathcal{H} \right) N_k^{dT} N_l^d \right] \, dV \right\} \tag{4.83}$$

where

$$c = \begin{cases} 1 & \text{for } \Psi_0^+ > \tilde{\mathcal{H}}, \\ 0 & \text{otherwise,} \end{cases} \tag{4.84}$$

and $\tilde{\mathcal{H}}$ denotes the free energy history from previous iteration. The assembly operator A adds up the the contributions of local values at element nodes $i, j, k, l = 1, ..., n_{en}$ to their global counterparts at nodes $I, J, K, L = 1, ..., n_{nd}$ in the Finite Element mesh with n_{nd} number of nodes.

In order to solve the system of iterative Finite Element equations (4.77), one can use a staggered scheme, to decrease the computational cost

$$\boldsymbol{R}^u + \boldsymbol{K}^{uu}\Delta\boldsymbol{U} = \boldsymbol{0} \quad \text{with } \boldsymbol{D} = \boldsymbol{D}(t_n) \tag{4.85}$$

$$\boldsymbol{R}^d + \boldsymbol{K}^{dd}\Delta\boldsymbol{D} = \boldsymbol{0} \tag{4.86}$$

So, the solutions for displacement and damage fields are obtained through successive solution of the above equations. However, it should be noted that the crack evolution speed is going to be affected, which could be controlled through adaptive time stepping [53].

We implemented our formulation by adding user material and element codes to the Finite Element program FEAP [68]. Also, the Finite Element meshes for the numerical examples are generated using the mesh generation program Gmsh [69].

4.3 Specific Constitutive Relations

Maximum shrinkage evolution in Figure 2.2 is assumed for the matrix phase and is applied uniformly throughout using the following

$$\boldsymbol{\varepsilon} = \operatorname{sym}(\nabla\boldsymbol{u}) - \varepsilon_{sh}\mathbf{1}, \tag{4.87}$$

where ε_{sh} is the shrinkage strain and $\mathbf{1}$ is the identity tensor. For aggregates no shrinkage is assumed, so, strains are defined as

$$\boldsymbol{\varepsilon} = \operatorname{sym}(\nabla\boldsymbol{u}) \tag{4.88}$$

As mentioned before, the free energy of the bulk material is decomposed into compressive and tensile parts as

$$\psi(\boldsymbol{\varepsilon}, d) = g(d)\psi_0^+(\boldsymbol{\varepsilon}) + \psi_0^-(\boldsymbol{\varepsilon}), \tag{4.89}$$

The material for both matrix and aggregates is assumed to be linear elastic. In order to take into account aging of concrete, the material properties for the matrix phase are assumed to evolve with time. Here we use aging model from Andiç's thesis [70]. The material properties are assumed to vary according to the following aging equations

$$E = E_f \chi^{1/3} \tag{4.90}$$

$$\nu = 0.18\text{sin}(\frac{\pi\xi}{2}) + 0.5\text{exp}(-10\xi) \tag{4.91}$$

$$g_f = g_{f,f}\chi \tag{4.92}$$

$$f_t = f_{t,f}\chi^{2/3} \tag{4.93}$$

where subscript f denotes the final value of the corresponding property. Also, χ is the aging variable and ξ is the degree of hydration, which are determined through the following relations

$$\dot{\xi} = \frac{A_\xi}{\eta_\xi}\text{exp}(-\frac{E_a}{R\theta}) \tag{4.94}$$

$$\dot{\chi} = \lambda_\theta \lambda_\xi \dot{\xi} \tag{4.95}$$

where A_ξ, η_ξ, λ_θ, and λ_ξ are defined as

$$A_\xi = \kappa_\xi(\frac{A_{\xi 0}/k_\xi}{\xi_f} + \xi)(\xi_f - \xi) \tag{4.96}$$

$$\lambda_\theta = (\frac{\theta_{\max} - \theta}{\theta_{\max} - \theta_r})^{n_\theta} \tag{4.97}$$

$$\lambda_\xi = A_f\xi + B_f \tag{4.98}$$

The values of all the parameters used are given in Table 4.1. The resulting evolution of properties are depicted in Figure 4.7. Lamé parameters λ and μ are then obtained

Table 4.1: Values of the parameters used in aging relations

parameter	unit	value
ξ_f	-	0.75
$\kappa_\xi/\eta_{\xi 0}$	$10^8\mathrm{hr}^{-1}$	0.32
η	-	6.5
$A_{\xi 0}/\kappa_\xi$	10^{-5} -	1.00
E_a/R	10^3 -	5.00
θ	K	293
θ_r	K	293
$\theta_{\max}$	K	393
n_θ	-	0.4
A_f,B_f	-	0.47, 1.16

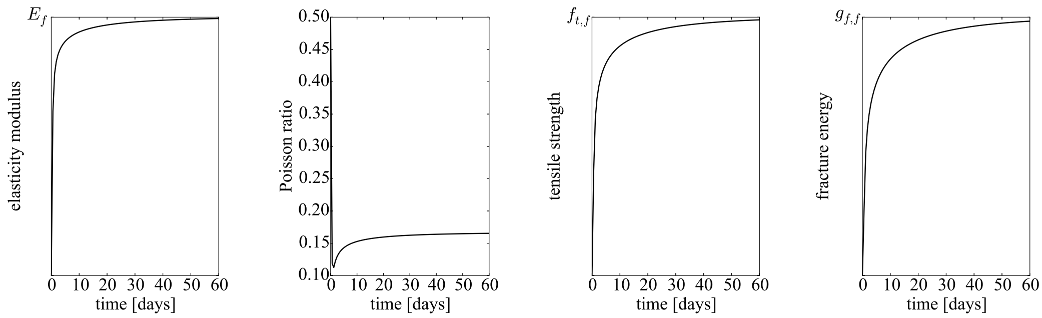

(a) (b) (c) (d)

Figure 4.7: Evolution of material properties with time (a) elasticity modulus E (b) Poisson ratio ν (c) tensile strength f_t (d) fracture energy g_f

using the following relations

$$\lambda = \frac{E\nu}{(1+\nu)(1-2\nu)}; \quad \mu = \frac{E}{2(1+\nu)} \tag{4.99}$$

Compressive and tensile parts of the free energy ψ_0^- and ψ_0^+ are then defined as [53]

$$\psi_0^+(\boldsymbol{\varepsilon}) = \frac{\lambda}{2}\left\langle \mathrm{tr}(\boldsymbol{\varepsilon})\right\rangle_+^2 + \mu \mathrm{tr}(\boldsymbol{\varepsilon}_+{}^2) \tag{4.100}$$

$$\psi_0^-(\boldsymbol{\varepsilon}) = \frac{\lambda}{2}\left\langle \mathrm{tr}(\boldsymbol{\varepsilon})\right\rangle_-^2 + \mu \mathrm{tr}(\boldsymbol{\varepsilon}_-{}^2), \tag{4.101}$$

where $\boldsymbol{\varepsilon}_+$ and $\boldsymbol{\varepsilon}_-$ are defined using the spectral decomposition of the strain tensor $\boldsymbol{\varepsilon} = \sum_{i=1}^{D} \epsilon_i \boldsymbol{n}_i \otimes \boldsymbol{n}_i$ where ϵ_i's are the eigenvalues and $\boldsymbol{n}_i$'s are the eigenvectors

$$\boldsymbol{\varepsilon}_+ = \sum_{i=1}^{D} < \epsilon_i >_+ \boldsymbol{n}_i \otimes \boldsymbol{n}_i, \quad \boldsymbol{\varepsilon}_- = \sum_{i=1}^{D} < \epsilon_i >_- \boldsymbol{n}_i \otimes \boldsymbol{n}_i \tag{4.102}$$

and $< x >_+ = (x + |x|)/2$ and $< x >_- = (x - |x|)/2$.

Then, the stresses $\boldsymbol{\sigma}$ and tangents $\mathbb{C}^{uu}$ and $\boldsymbol{C}^{ud}$ are defined as

$$\boldsymbol{\sigma} = g(d)[\lambda < \mathrm{tr}(\boldsymbol{\varepsilon}) >_+ \mathbf{1} + 2\mu\boldsymbol{\varepsilon}_+] + [\lambda < \mathrm{tr}(\boldsymbol{\varepsilon}) >_- \mathbf{1} + 2\mu\boldsymbol{\varepsilon}_-] \tag{4.103}$$

$$\mathbb{C}^{uu} = \frac{\partial \boldsymbol{\sigma}}{\partial \boldsymbol{\varepsilon}} = g(d)[\lambda \frac{< \mathrm{tr}(\boldsymbol{\varepsilon}) >_+}{\mathrm{tr}(\boldsymbol{\varepsilon})} \mathbf{1} \otimes \mathbf{1} + 2\mu\mathbb{P}_+] + [\lambda \frac{< \mathrm{tr}(\boldsymbol{\varepsilon}) >_-}{\mathrm{tr}(\boldsymbol{\varepsilon})} \mathbf{1} \otimes \mathbf{1} + 2\mu\mathbb{P}_-] \tag{4.104}$$

$$\boldsymbol{C}^{ud} = \frac{\partial \boldsymbol{\sigma}}{\partial d} = g'(d)[\lambda < \mathrm{tr}(\boldsymbol{\varepsilon}) >_+ \mathbf{1} + 2\mu\boldsymbol{\varepsilon}_+] \tag{4.105}$$

where $\mathbb{P}_+ = \dfrac{\partial \boldsymbol{\varepsilon}_+}{\partial \boldsymbol{\varepsilon}}$ and $\mathbb{P}_- = \dfrac{\partial \boldsymbol{\varepsilon}_-}{\partial \boldsymbol{\varepsilon}}$ are positive and negative projection tensors. Using the formulations given in [71, 72] we have

$$\begin{aligned} \mathbb{P}_+ = &\sum_i \sum_j \frac{\partial < \epsilon_i >_+}{\partial \epsilon_j} \boldsymbol{n}_i \otimes \boldsymbol{n}_i \otimes \boldsymbol{n}_j \otimes \boldsymbol{n}_j \\ &+ \sum_i \sum_{j \neq i} \frac{1}{2} \frac{< \epsilon_i >_+ - < \epsilon_j >_+}{\epsilon_i - \epsilon_j} \boldsymbol{n}_i \otimes \boldsymbol{n}_j \otimes (\boldsymbol{n}_i \otimes \boldsymbol{n}_j + \boldsymbol{n}_j \otimes \boldsymbol{n}_i), \end{aligned} \tag{4.106}$$

$$\mathbb{P}_- = \mathbb{I} - \mathbb{P}_+, \tag{4.107}$$

where $\mathbb{I}$ is the fourth-order identity tensor. The above expression is valid for distinct eigenvalues. In case of identical eigenvalues, i.e. if $\epsilon_i = \epsilon_j$ the second term in (4.106) is zero, and it simplifies to

$$\mathbb{P}_+ = \sum_i \sum_j \frac{\partial < \epsilon_i >_+}{\partial \epsilon_j} \boldsymbol{n}_i \otimes \boldsymbol{n}_i \otimes \boldsymbol{n}_j \otimes \boldsymbol{n}_j \tag{4.108}$$

CHAPTER 5

NUMERICAL EXAMPLES

In this chapter we aim to validate our implementation of the phase-field method for both brittle and quasi-brittle fracture through numerical benchmark examples. We then apply the method to the cracking problem of pole sections undergoing shrinkage strains. In Section 5.1, we verify our implementation of the Phase-Field Model for brittle fracture proposed by Miehe et al. [53]. Then, in Section 5.1.1, we study the convergence of the results for different mesh sizes. Then in sections 5.1.2 and 5.1.3 we compare our solutions with solutions given in Miehe et al. [53] for two benchmark problems. Next, in Section 5.2, we verify our implementation of Wu's model [64] for quasi-brittle fracture in a similar fashion. First, in section 5.2.3 we show the convergence of the results with different mesh sizes. Thereafter, in Sections 5.2.2 and 5.2.4, we verify our solution of two benchmark problems from [64] and [73] comparing to their corresponding solutions. Later, in Section 5.3, we analyze a homogeneous macroscopic pole section undergoing differential shrinkage strains according to [1]. Finally, we conclude the chapter by solving cracking problem of mesoscopic pole sections undergoing shrinkage in Section 5.4. First, in Section 5.4.1, we analyze a pole section with segregated aggregates according to [1]. Afterward, in Section 5.4.2, we analyze pole sections with different aggregate gradings to see the effect of grading as compared to segregation.

5.1 Phase-Field method for Brittle Fracture

In this section the numerical implementation of the exponential model proposed in [53] is verified using numerical examples. The damage evolution equation 4.61 is used.

5.1.1 Convergence Study

First, we analyze convergence of the solution with the mesh size. For this purpose, we consider a crack propagation of the single-edge notched plate in tension in reference [53] for different mesh sizes. The lower edge is fixed and the upper edge is subjected to vertical displacement u (Figure 5.1). The displacement u is imposed in increments of $\Delta u = 1 \times 10^{-5}\text{mm}$ for the first 500 steps and $\Delta u = 1 \times 10^{-6}\,\text{mm}$ for the remaining steps. Material properties are $\lambda = 121.15\,\text{kN/mm}^2$, $\mu = 80.77\,\text{kN/mm}^2$, and $g_f = 2.7 \times 10^{-3}\,\text{kN/mm}$. The length scale value of $0.02\,\text{mm}$ is chosen. In order to achieve a good approximation of crack surface, element size h around the crack need to be small enough. According to Miehe et al. [52] it is needed that $h < l/2$. Linear triangular elements with three different sizes around the crack path are used. The geometry and boundary conditions along with the results for different element sizes are shown in Figure 5.1. As it is seen the results are independent of mesh size and converge as the mesh size is refined.

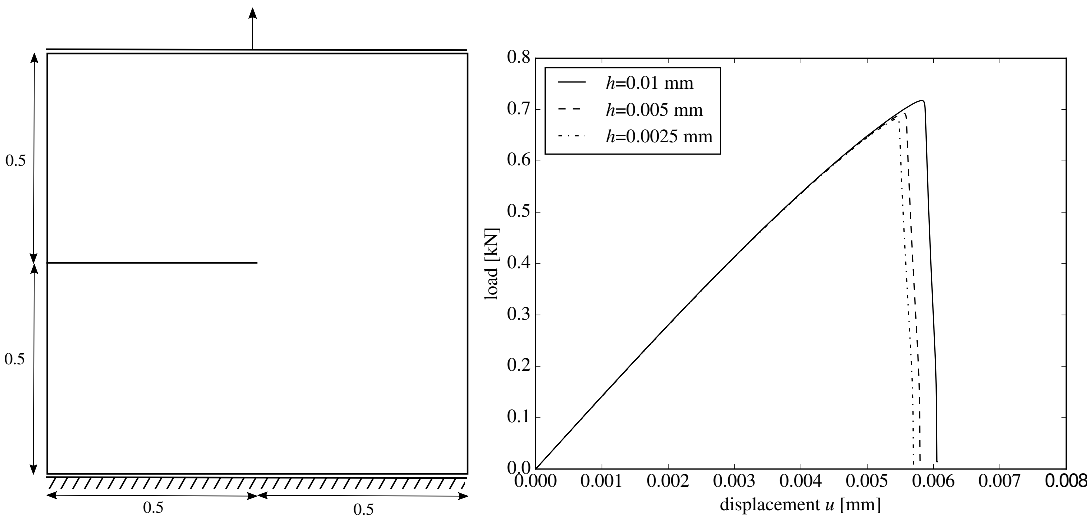

Figure 5.1: Convergence study. Single-edge notched plate in tension

5.1.2 Single-Edge-Notched Plate in Tension

As the first benchmark example, we solve the same problem of the plate in tension in the previous convergence study. The same displacement increments are used as before, and a mesh with about 30000 linear triangular elements with critical element size of $h = 0.003\,\mathrm{mm}$ around the crack path. The length scale value used is $0.015\mathrm{mm}$. The load-displacement curve and damage pattern are shown in Figure 5.2, where the blue-colored regions are intact ($d = 0$) while the red-colored regions correspond to the broken state ($d = 1$). This conventions holds for all the phase-field contour plots in the following illustrations. It is seen that the results are in good agreement with those in [53].

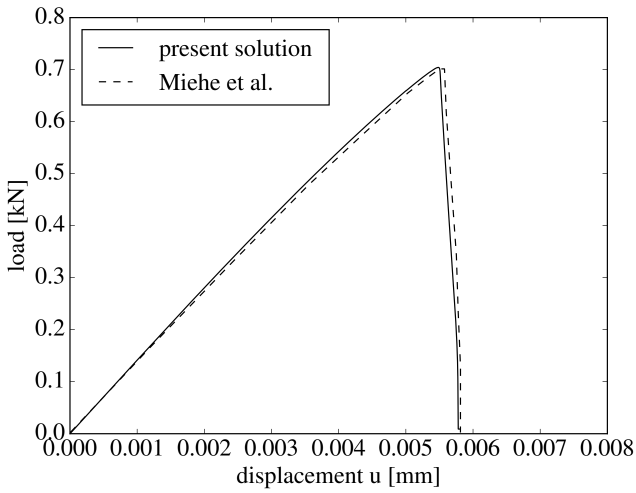

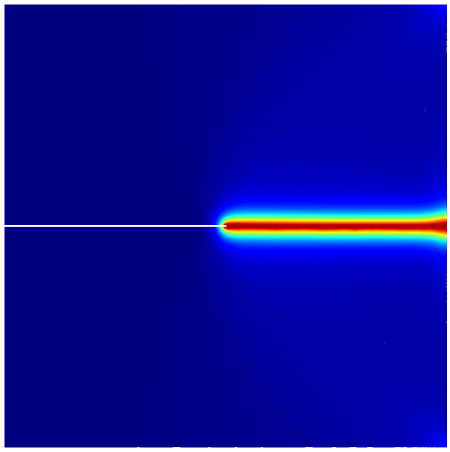

Figure 5.2: Load-displacement curve and damage pattern for the tension test

5.1.3 Single-Edge-Notched Plate in shear

The second example is the same notched plate in the previous example in shear loading [53]. The lower edge is fixed and the upper edge is subjected to horizontal displacement u. The displacement increments of $\Delta u = 1 \times 10^{-5}\,\mathrm{mm}$ are used. A mesh consisting of about 45000 linear triangular elements is used, with critical element size of $h = 0.003\,\mathrm{mm}$ around the crack path. Also, the right and left edges are prevented from vertical displacement. The geometry and boundary conditions are shown in Figure 5.3. All the properties are the same as the previous example. The load-displacement curve and damage pattern are shown in Figure 5.4. The results are in good agreement with those in [53] again.

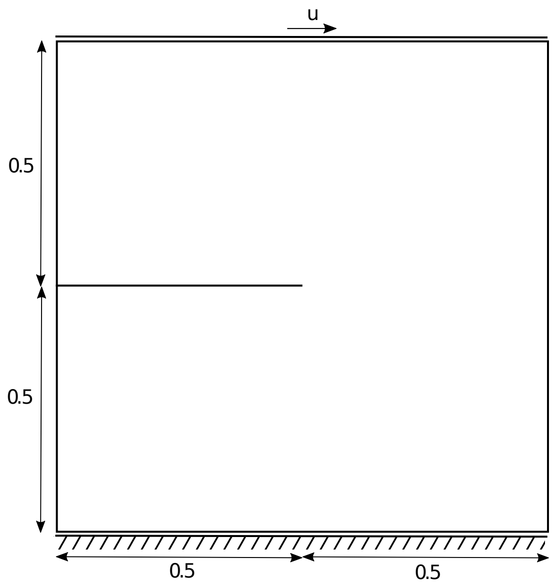

Figure 5.3: Single-edge notched plate in shear

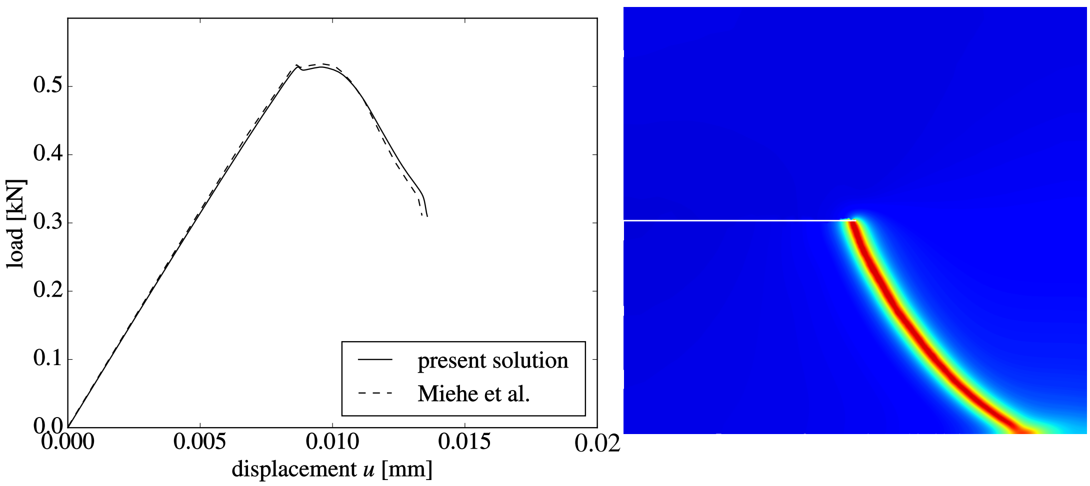

Figure 5.4: Load-displacement curve and damage pattern for the shear test

5.2 Phase-Field method for Quasi-Brittle Fracture

In this section the numerical implementation of the new sine model for cohesive fracture proposed in [64] is verified using the selected numerical examples.

5.2.1 Convergence Study 1

To study the convergence with mesh size, we consider the three-point bending problem from [73] for different element sizes. The beam is simply supported and loaded on the top edge at the center with displacement u, which is imposed in increments $\Delta u = 1 \times 10^{-4}\,\mathrm{mm}$. Material properties are $E = 100\,\mathrm{MPa}$, $\nu = 0.0$, $f_t = 1.0\,\mathrm{MPa}$, and $g_f = 0.1\ \mathrm{N/mm}$. The length scale value of $0.2\ \mathrm{mm}$ has been used. Here, the damage evolution equation (4.61) is used. The geometry and boundary conditions and the resulting load-displacement curves for different element sizes are shown in Figure 5.5. It is seen that the solutions are independent of the mesh size.

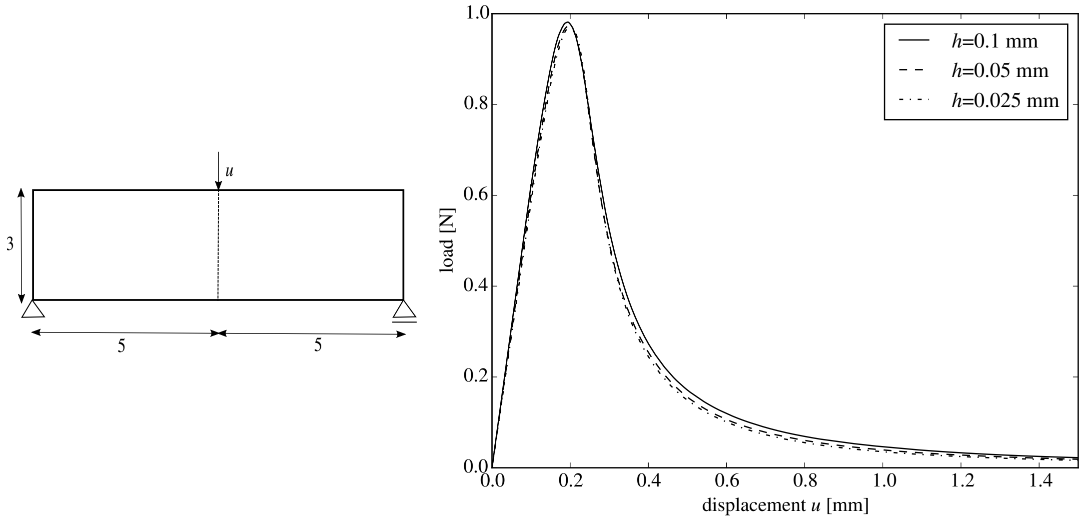

Figure 5.5: Convergence study 1 (all dimensions are in mm, and depth = 1.0 mm.)

5.2.2 Three-Point Bending Test 1

The beam bending problem is solved and compared to the results of Wells and Sluys [73]. They solved using the Finite Element method with new enriched shape function to incorporate the discontinuity at the crack. Length scale value is chosen as $l = 0.1\mathrm{mm}$. A mesh of about 30000 Linear triangular elements with size of $h = 0.05\,\mathrm{mm}$ is used. Again, the damage evolution equation (4.61) is employed. The load-displacement curve and damage patterns are given in Figure 5.6.

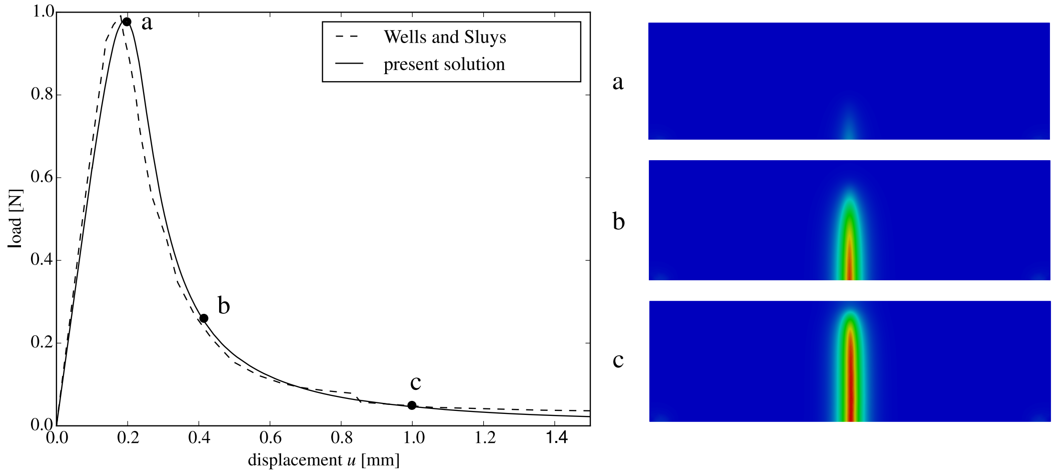

Figure 5.6: Load-displacement curve and damage patterns for the three-point bending test 1

5.2.3 Convergence Study 2

In the second convergence study, we consider the three-point notched beam bending problem from [64] for different element sizes. Material properties are $E = 2.0 \times 10^4\,\mathrm{MPa}$, $\nu = 0.2$, $f_t = 2.4\,\mathrm{MPa}$, and $g_f = 0.113\,\mathrm{N/mm}$. The length scale is chosen as $l = 2.5\,\mathrm{mm}$. The beam geometry and loading is given in Figure 5.7 along with the resulting load-displacement curves for different element sizes. It is seen that the solutions converge as finer meshes are used.

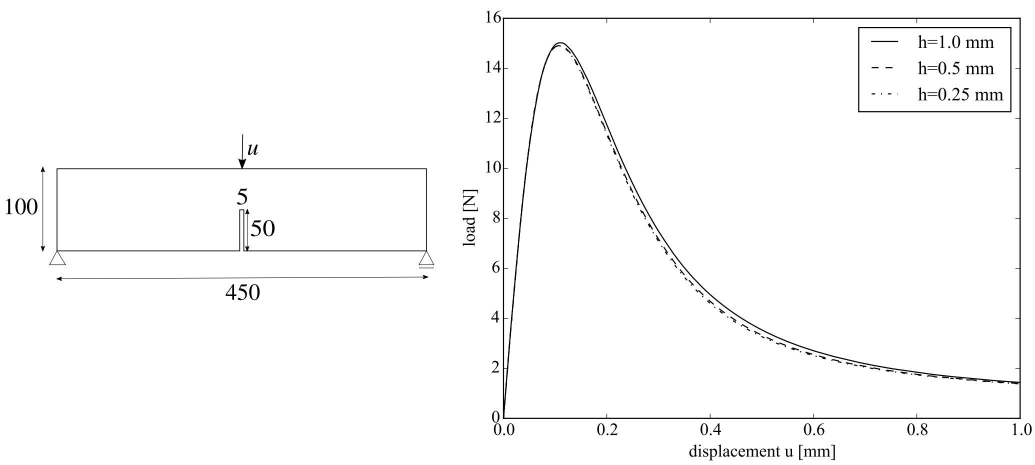

Figure 5.7: Convergence study 2 (all dimensions are in mm, and depth = 100 mm.)

5.2.4 Three-Point Bending Test 2

The three-point notched beam bending is solved and compared with Wu's solution [64]. The beam geometry and loading is given in Figure 5.7. A length scale of value $l = 2.5\,\mathrm{mm}$ is used. A mesh of about 120000 linear triangular elements is generated with critical element size of $h = 1.0\,\mathrm{mm}$ around the crack path. The evolution equation (4.61) is used, with driving energy (ψ_0^+) in (4.60) substituted by y in (4.29). The load-displacement curve and damage patterns are given in Figure 5.8.

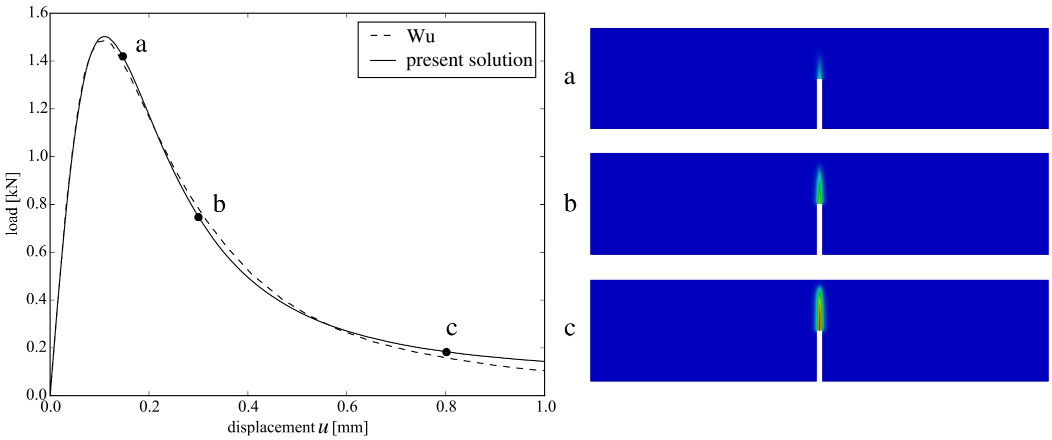

Figure 5.8: Load-displacement curve and damage patterns for three-point bending test 2

In the following examples, the method is applied to solve the crack propagation in pole sections under shrinkage. In all the following examples, the evolution equation (4.61) is used with the energy ψ_0^+ in (4.60) substituted by the reference energy y in (4.29) proposed by Wu [64].

5.3 Macroscopic Analysis of the Pole Section

Here we analyze a homogeneous pole section under shrinkage. Due to symmetry only a quarter of the section is analyzed. The geometry and boundary conditions are depicted in Figure 5.9. Final material properties are chosen as: $E_f = 30\mathrm{GPa}$, $g_{f,f} = 0.1\mathrm{N/mm}$, and $f_{t,f} = 4.0\mathrm{MPa}$. The length scale value is set to $l = 1\,\mathrm{mm}$. Aging is taken into account using (4.90)-(4.93) for material properties, with the parameters defined in Table 4.1. f_t and g_f are assigned to each element with a random variation of about one percent to facilitate damage localization at multiple locations. This random variation is depicted in Figure 5.10. Shrinkage strains are imposed as

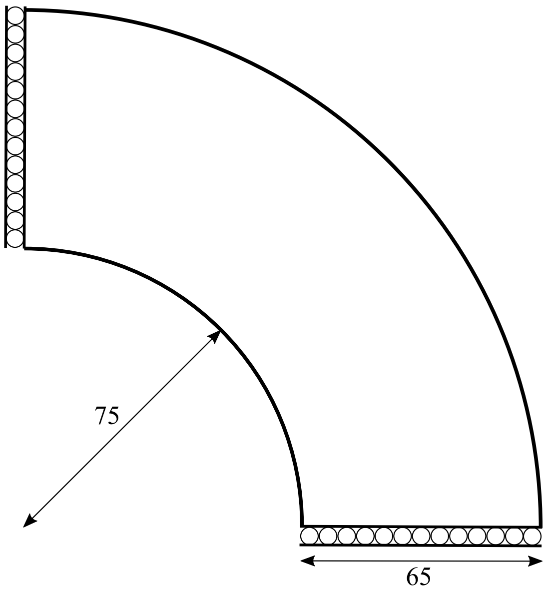

Figure 5.9: Pole section geometry and boundary conditions. All dimensions are given in millimeters.

Figure 5.10: Spatial variation of f_t and g_f

$$\varepsilon_{sh} = \varepsilon_{sh,f}(r) f(t), \tag{5.1}$$

where $\varepsilon_{sh,f}$ is the final shrinkage strain and $f(t)$ is the time variation of shrinkage. The final shrinkage value $\varepsilon_{sh,f}$ is assumed to vary quadratically with distance from the outermost wall of the pole with minimum shrinkage of -0.00025 reaching its maximum value of -0.0024 at the innermost wall as shown in Figure 5.12. The time evolution of shrinkage $f(t)$ is shown in Figure 5.11. A mesh with about 120000 linear triangular elements of size $h = 0.5\,\mathrm{mm}$ is used and the analysis is conducted in 1000 steps. Results for a linear elastic analysis are shown in Figure 5.13 and for crack propagation are shown in Figure 5.15. The resultant reaction moment is drawn against maximum shrinkage strains at the inside wall in Figure 5.14.

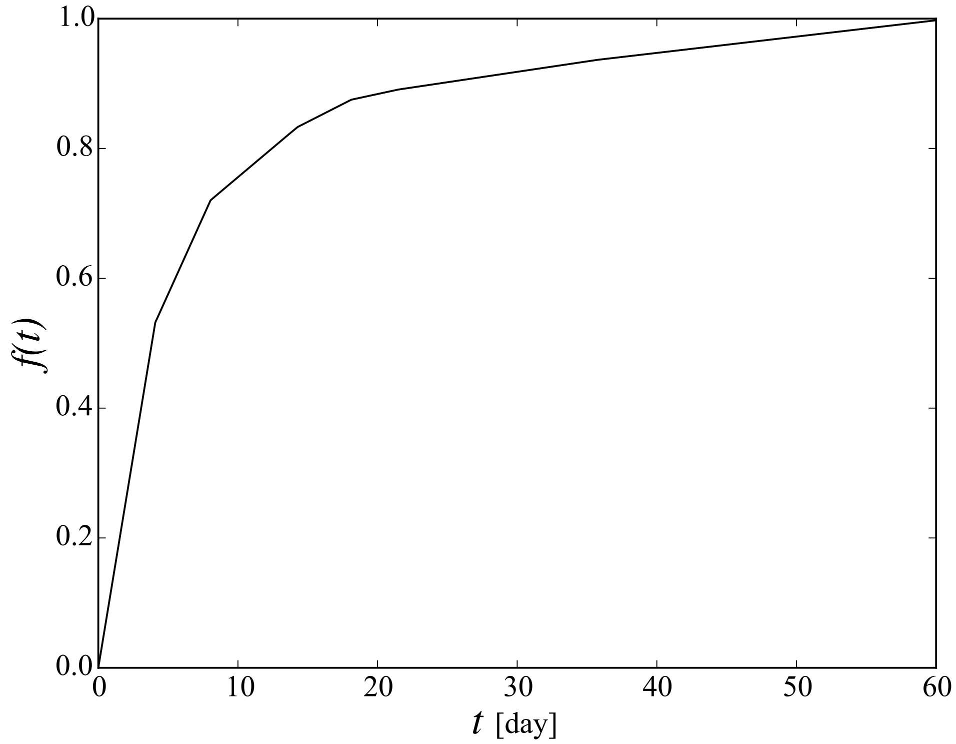

Figure 5.11: Time variation of shrinkage

The linear elastic analysis results in Figure 5.13 show unrealistically high stress values on the interior wall. On the other hand, the stress values drop to values lower than the tensile strength, which is $4.0\,\mathrm{MPa}$ here. However, the crack propagation analysis results in a crack that extends close to the outer surface as is shown in Figure 5.15 (a). It simply shows that using a mere linear elastic analysis, it is not possible to predict the extent of cracking. This is due to the fact that as the crack grows, the stresses in the inner cracked layers are relieved, and there will be new stress distribution over the section. So, the tensile stresses in the layers ahead of the crack will make the

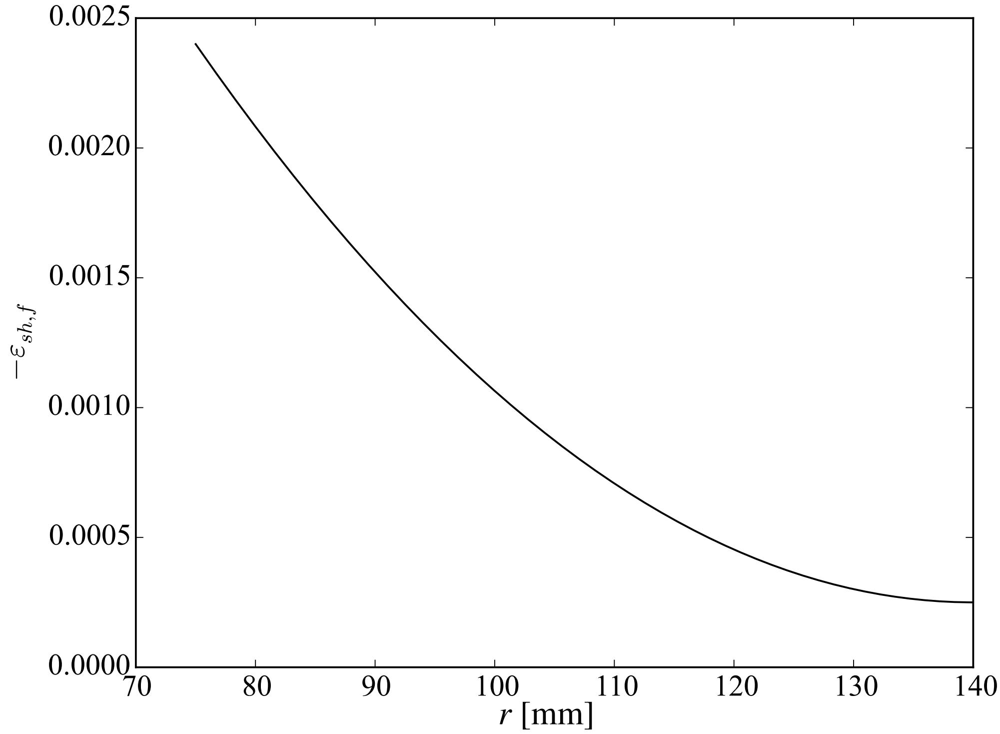

Figure 5.12: Spatial variation of shrinkage in terms of radius

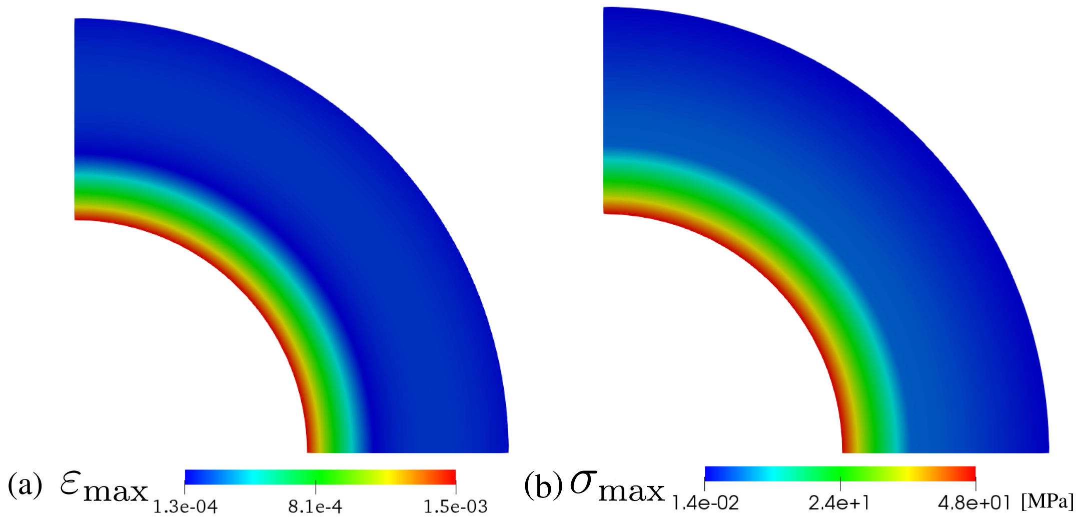

Figure 5.13: (a) Maximum principal strains and (b) maximum principal stresses $\sigma_{\max}$ for linear elastic analysis for differential shrinkage

crack go further until the stresses drop below the tensile strength. It should also be noted that the crack reaches almost the outer surface here, which does not agree with experimental observations (See Figure 1.4). It seems to be due to the exaggerated difference in shrinkage strains through the section given by [1], as shown in Figure

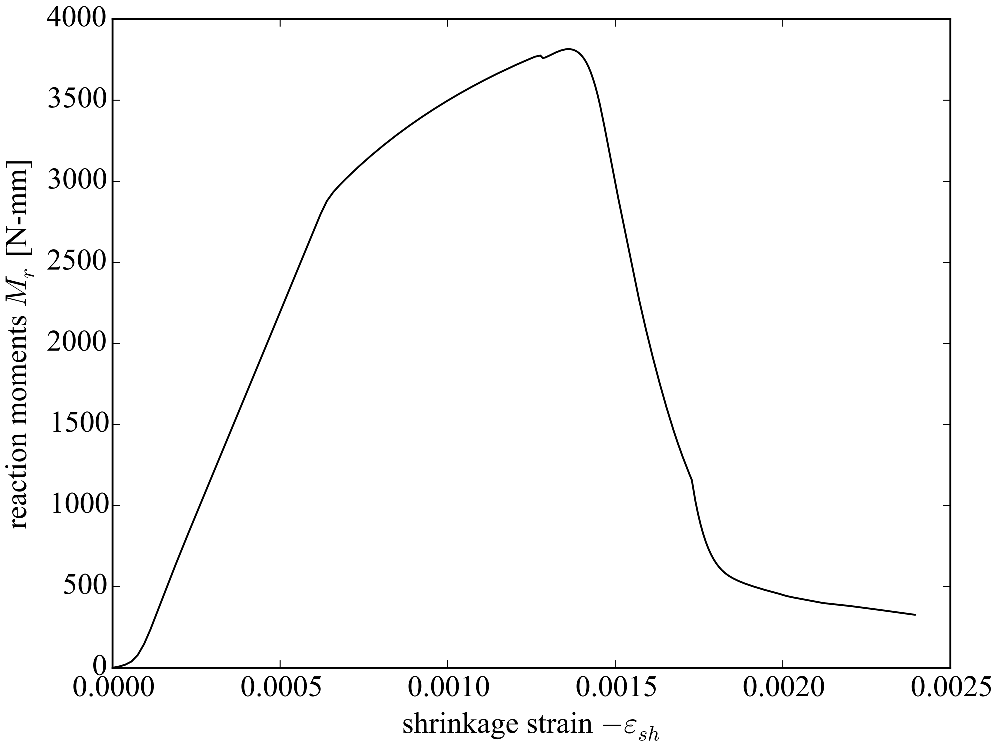

Figure 5.14: The resultant reaction moment vs. maximum shrinkage strains at the inside wall for macroscopic model

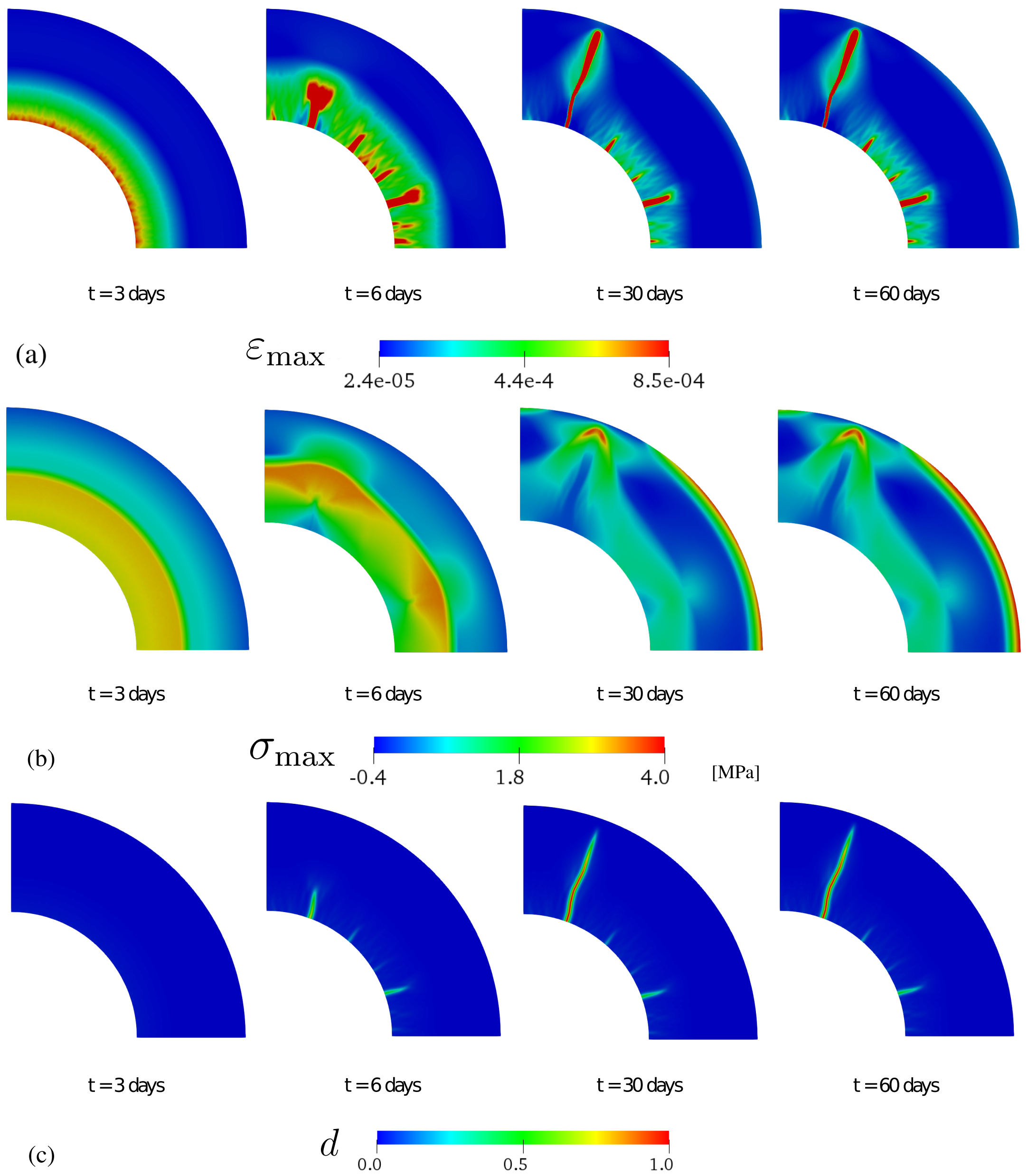

Figure 5.15: (a) Maximum principal strains, (b) maximum principal stresses and (c) damage contours for crack propagation for differential shrinkage

1.3. The measurements of shrinkage strains in segments, given by [1] and shown in Figure 1.2, seem to be insufficient to accurately predict the shrinkage strains in the corresponding pole section. Obviously, considering the number of segments and their small sizes compared to the dimensions of the pole section, the strain measurements are not a good representative of the strains in the whole section.

5.4 Mesoscopic Analysis of the Pole Section

In this section we study different pole sections to investigate the effect of aggregate grading and segregation on shrinkage-induced cracking. The same material properties are used in all the following examples, which are given in Table 5.1. In all the examples the length scale value of $l = 1\,\mathrm{mm}$ is used. The maximum shrinkage from Figure 1.2, i.e. -0.0024, is assigned to the matrix phase. Due to segregation the inner segment constitutes mostly paste and fines, and the maximum shrinkage is assumed to represent the shrinkage in the matrix phase.

Table 5.1: Material properties used in numerical analyses

phase	E[GPa]	ν	f_t[MPa]	g_f[N/mm]
aggregates	75.0	0.2	10.0	0.06
matrix	25.0	from (4.91)	4.0	0.05

5.4.1 Effect of Segregation

In the first example a segregated section is modeled according to the variation of aggregates given in Figure 2.1. A uniform final shrinkage strain of $\varepsilon_{sh,f} = -0.0024$ is assigned to the matrix phase using (5.1) with the time evolution $f(t)$ according to Figure 5.11 and the crack propagation in the section is investigated. The section is given in Figure 5.16. A mesh with about 140000 linear triangular elements of size $h = 0.5\,\mathrm{mm}$ is used and the analysis is conducted in 1000 steps. Maximum principal stress and strain contours for a linear elastic analysis are given in Figure 5.17. The results for crack propagation are also given in Figure 5.18. The resultant reaction moment plotted against shrinkage strain is provided in Figure 5.19.

Comparing the results of the linear elastic analysis and the crack propagation in Figures 5.17 and 5.18, respectively, it is seen that the locations of maximum stress concentration in linear elastic analysis and crack initiation are not the same. This shows the linear elastic analysis is insufficient. The reason is that, as damage grows, the strains and stresses change and redistribute. As a result, damage growth might hap-

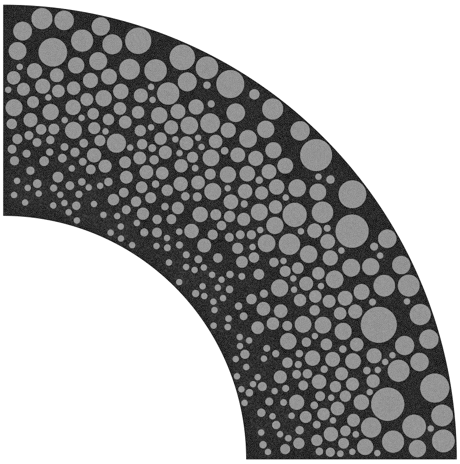

Figure 5.16: Segregated section

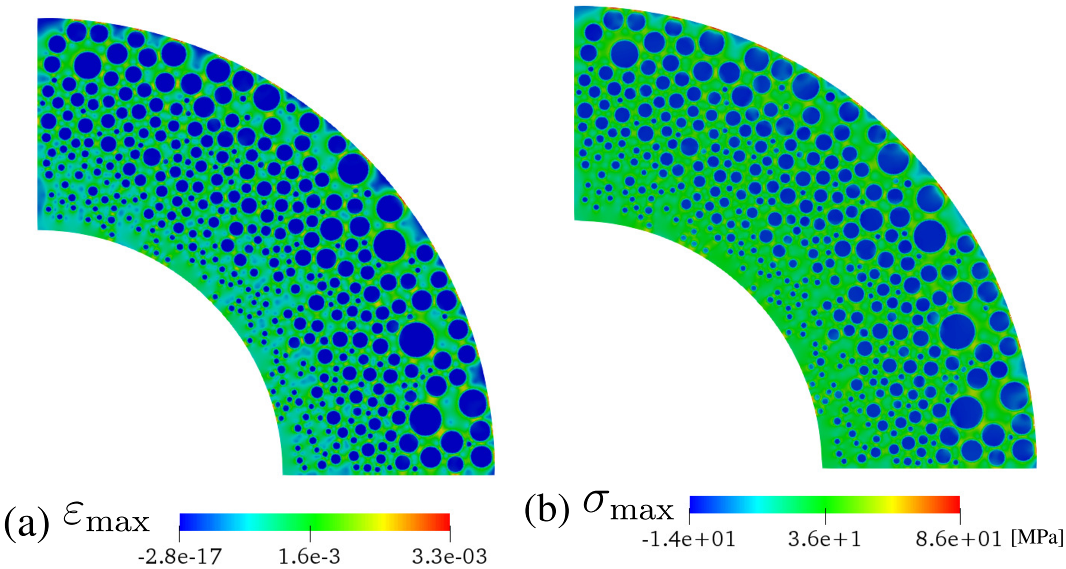

Figure 5.17: (a) Maximum principal strains and (b) maximum principal stresses for linear elastic analysis of the segregated section

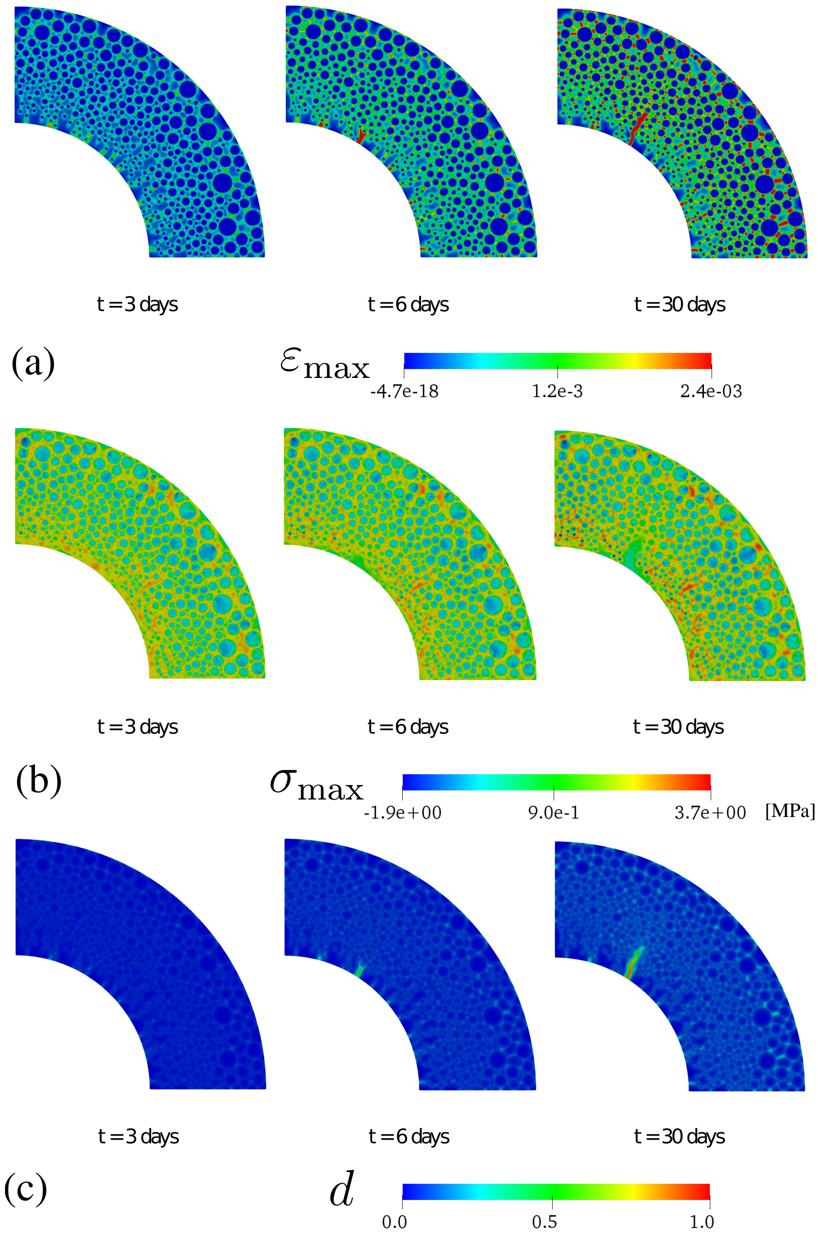

Figure 5.18: (a) Maximum principal strains, (b) maximum principal stresses and (c) damage contours for crack propagation of the segregated section

pen at different locations that cannot be predicted beforehand. The final damage contour in Figure 5.18 (c) shows that crack does not extend too deep through the section, which is in agreement with the experimental observations (See Figure 1.4).

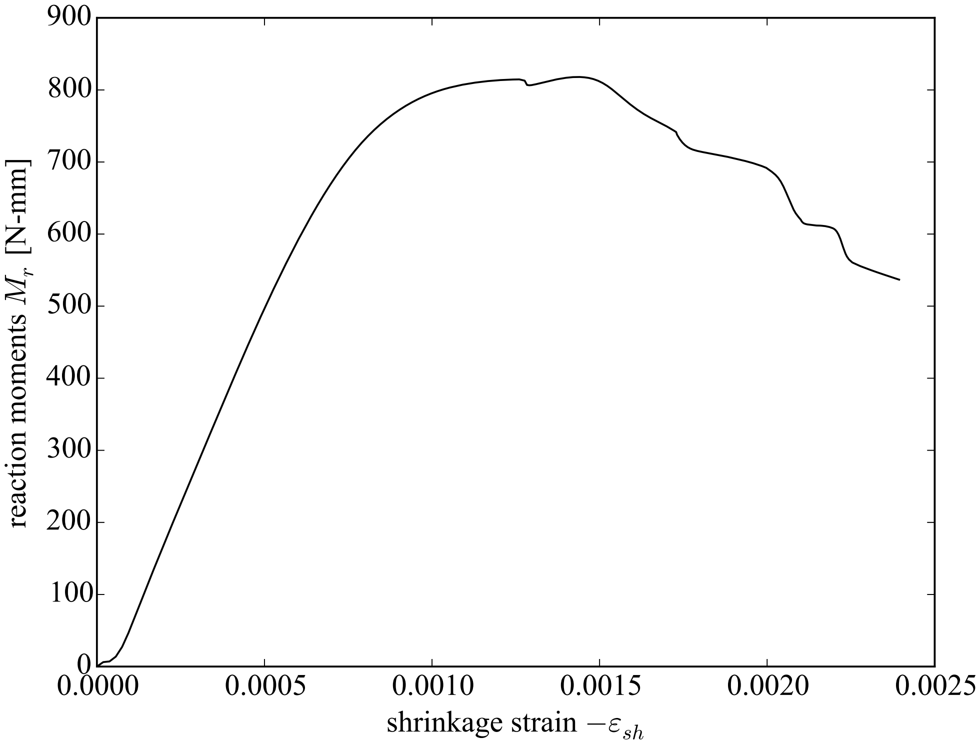

Figure 5.19: The resultant reaction moment vs. shrinkage strains for segregated section

5.4.2 Effect of Aggregate Grading

In this section we will investigate if the aggregate grading has a significant effect on cracking in pole sections. To this end we analyze three samples of well, gap, and poor gradings. The shrinkage imposed and the material properties are the same as for the segregated section in the previous example.

Well-graded Section

A well-graded section shown in Figure 5.20 is analyzed here. A mesh with about 150000 linear triangular elements of size $h = 0.5\,\mathrm{mm}$ is used and the analysis is conducted in 1000 steps. The results of a linear elastic analysis are given in Figure 5.21, and for the crack propagation analysis in Figure 5.22.

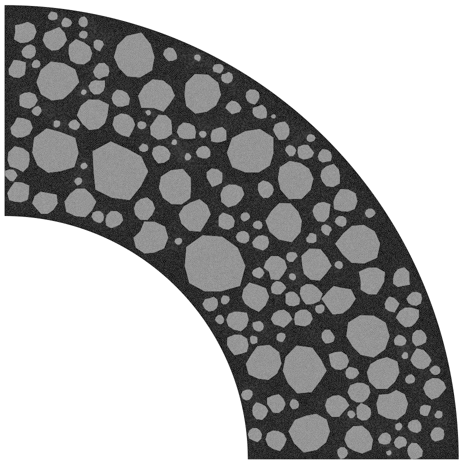

Figure 5.20: Well-graded section

The stress contours from the linear elastic analysis in Figure 5.21 (b) show unrealistically high values. Also, the stresses are higher than the tensile strength in most of the section. However, crack propagation analysis results in Figure 5.22 show very low damage values, and the damage does not even reach a full crack at any point. Similar to the previous examples, as damage starts to grow, strains relieve and new stresses form. Also, the load-bearing capacity of the material decreases as damage grows due to degradation of material properties. This, in turn, results in a redistribution of

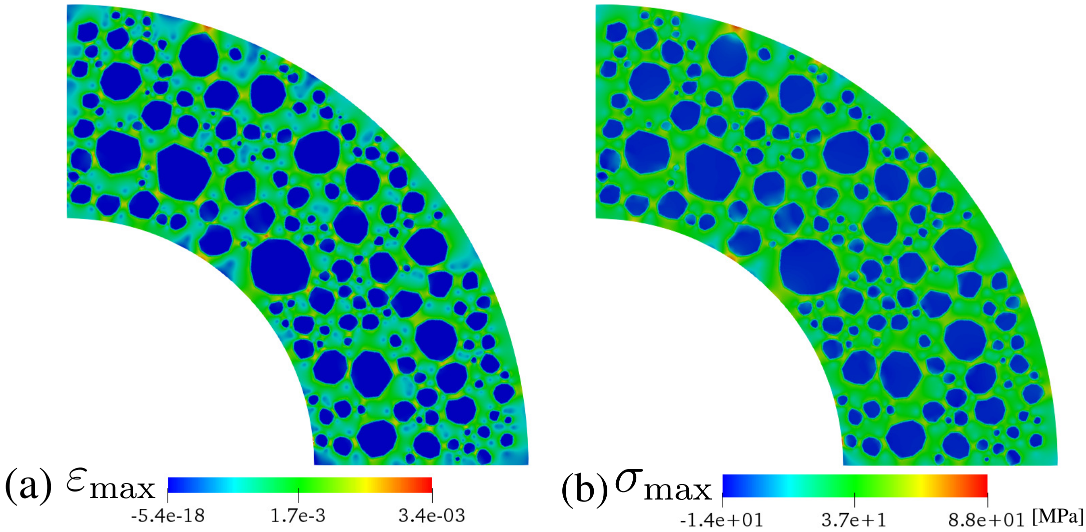

Figure 5.21: (a) Maximum principal strains and (b) maximum principal stresses for linear elastic analysis of the well-graded section

stresses.

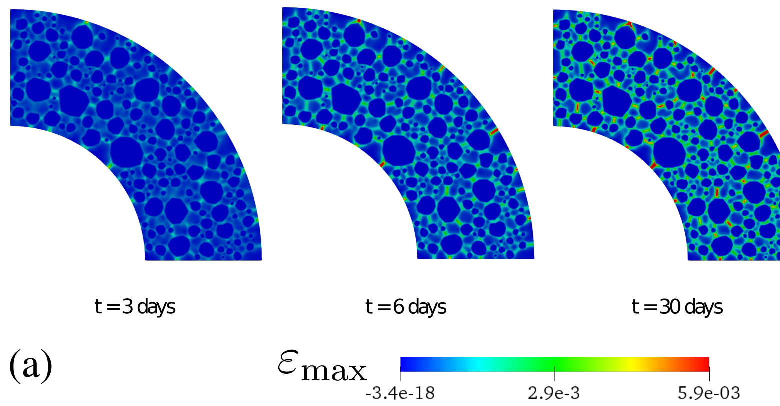

(a)

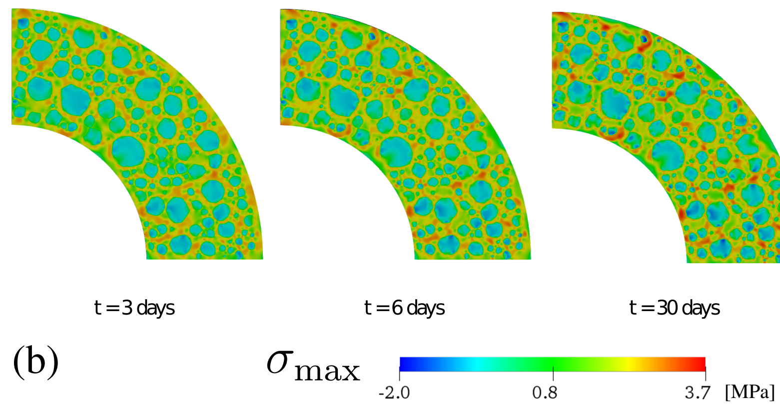

(b)

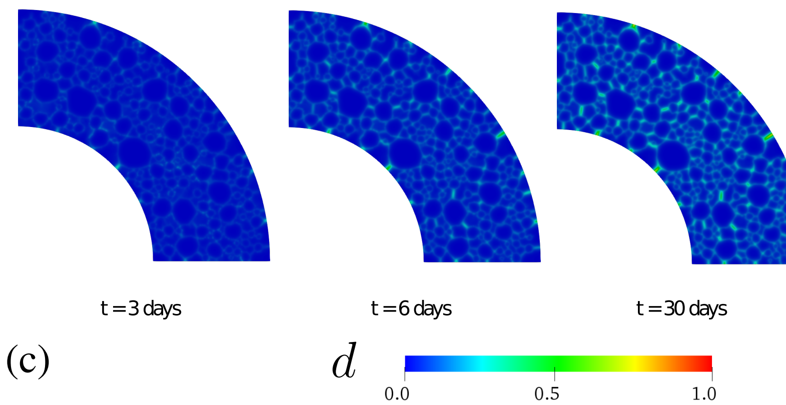

(c)

Figure 5.22: (a) Maximum principal strains, (b) maximum principal stresses and (c) damage contours for crack propagation of the well-graded section

Gap-graded Section

A gap-graded section is given in Figure 5.23 and analyzed. A mesh with about 180000 linear triangular elements of size $h = 0.5\,\mathrm{mm}$ is used and the analysis is conducted in 1000 steps. The results of a linear elastic analysis are given in Figure 5.24, and for the crack propagation analysis in Figure 5.25.

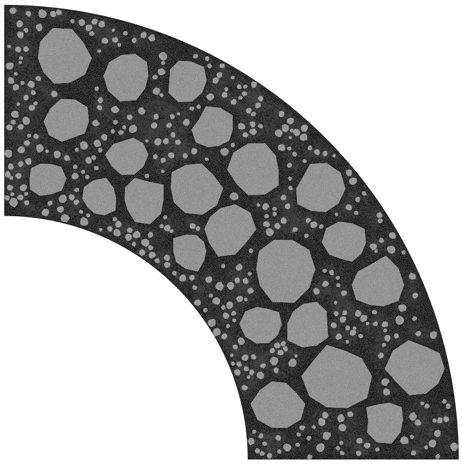

Figure 5.23: Gap-graded section

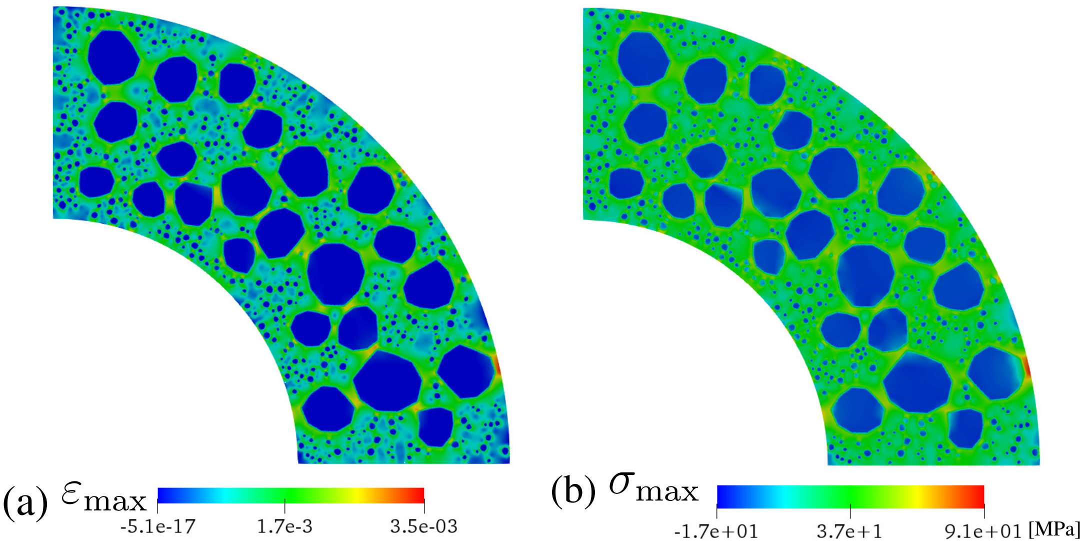

Figure 5.24: (a) Maximum principal strains and (b) maximum principal stresses for linear elastic analysis of the gap-graded section

Similar to the well-graded section in the previous example, here, damage grows very little over the whole section, as shown in Figure 5.25 (c), despite the high stress values predicted by a linear elastic analysis in Figure 5.24 (b).

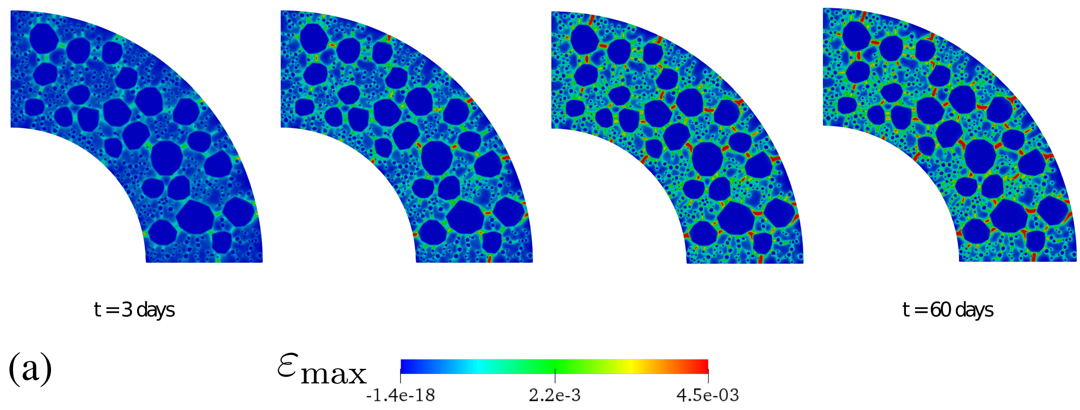

(a)

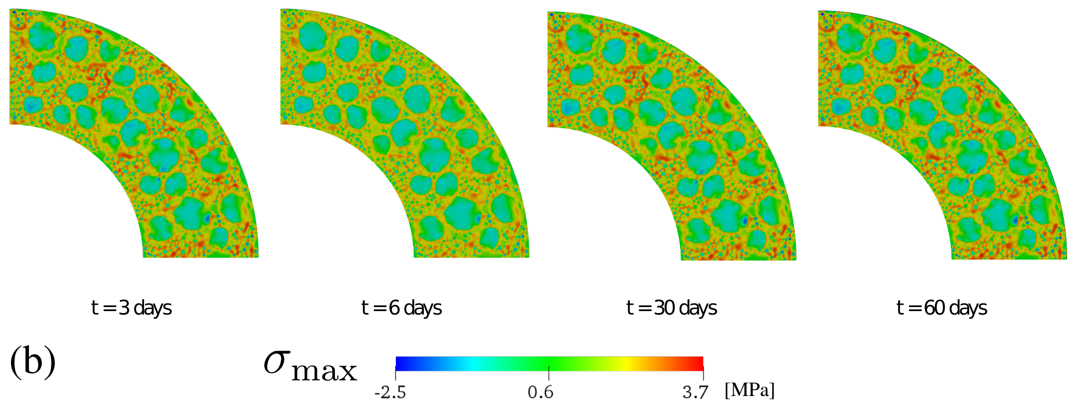

(b)

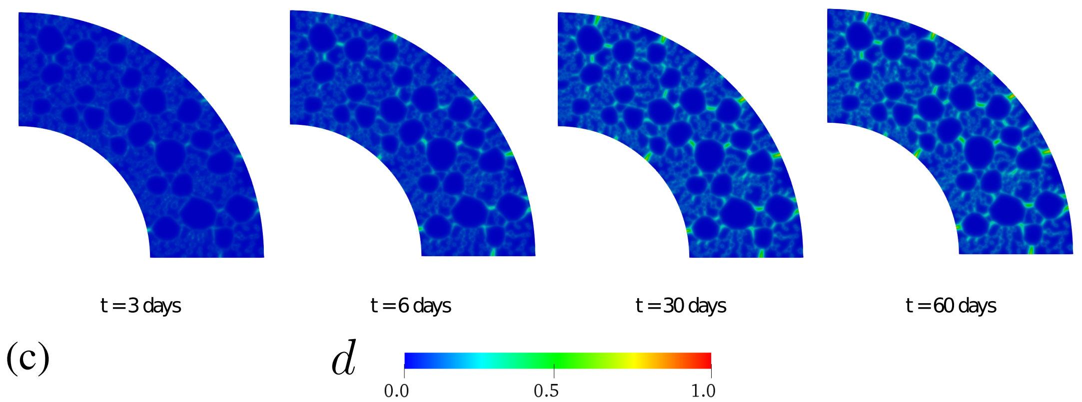

(c)

Figure 5.25: (a) Maximum principal strains, (b) maximum principal stresses and (c) damage contours for crack propagation of the gap-graded section

Poorly-graded Section

A poorly-graded section is shown in Figure 5.26. A mesh with about 130000 linear triangular elements of size $h = 0.5\,\mathrm{mm}$ is used and the analysis is conducted in 1000 steps. The results of a linear elastic analysis are given in Figure 5.28, and for the crack propagation analysis in Figure 5.29.

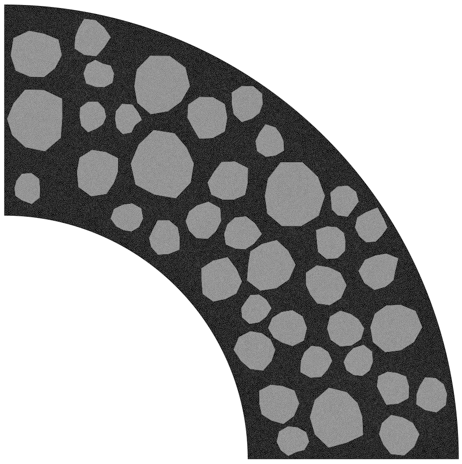

Figure 5.26: Poorly-graded section

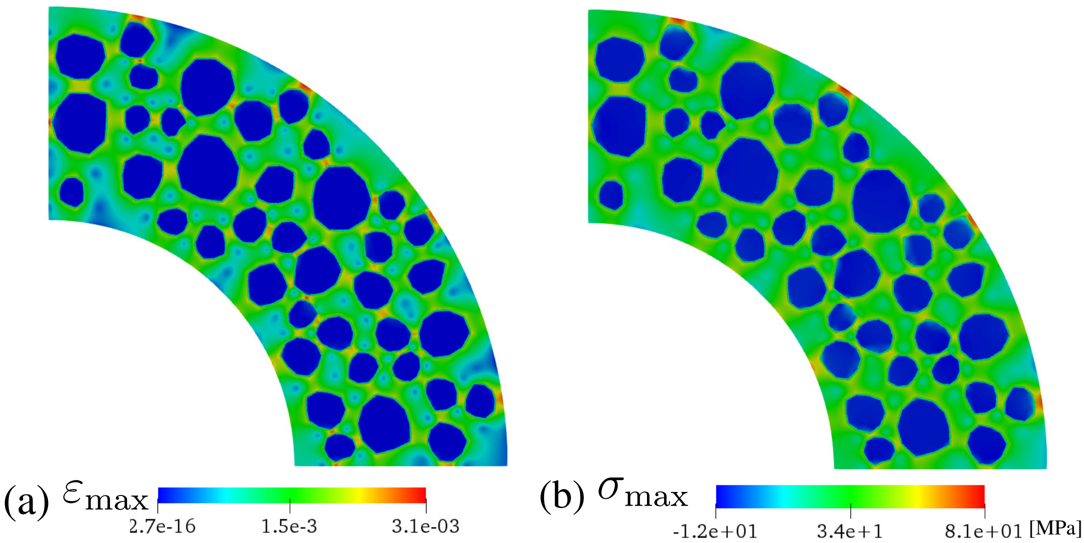

Figure 5.28: (a) Maximum principal strains and (b) maximum principal stresses for linear elastic analysis of the poorly-graded section

Comparing the results of the poorly-graded section with the gap-graded and well-graded sections in the previous examples, this is the worst of the three cases. Of all the gradings, the poorly-graded section show some surface cracks formed under srinkage, as seen in Figure 5.29 (c). Still, similar to the previous cases, the damaging is far less critical than what expected from the stress distribution from a linear elastic

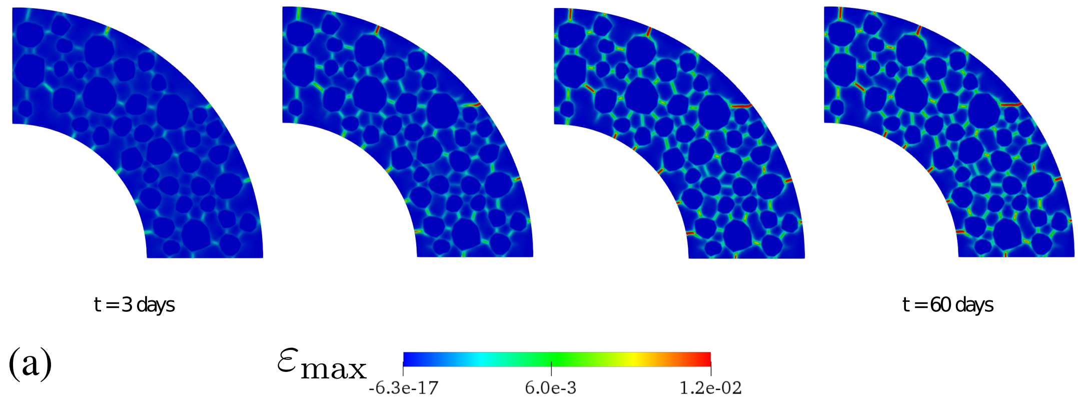

(a)

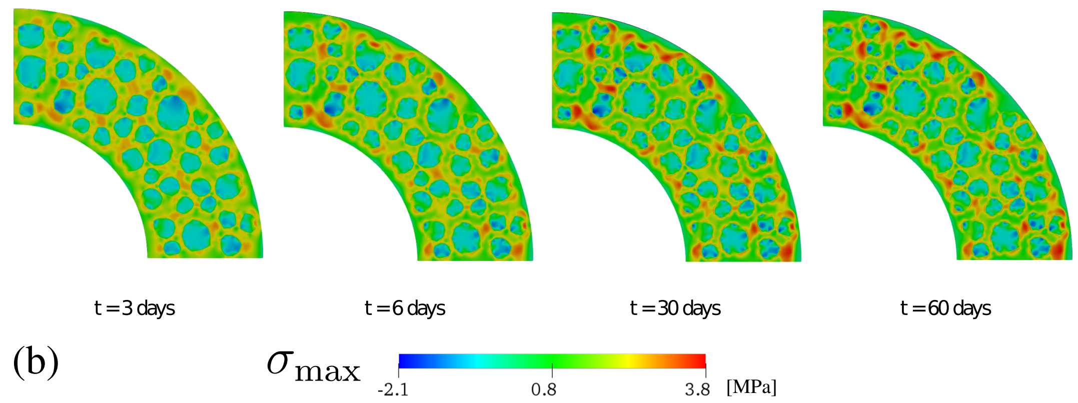

(b)

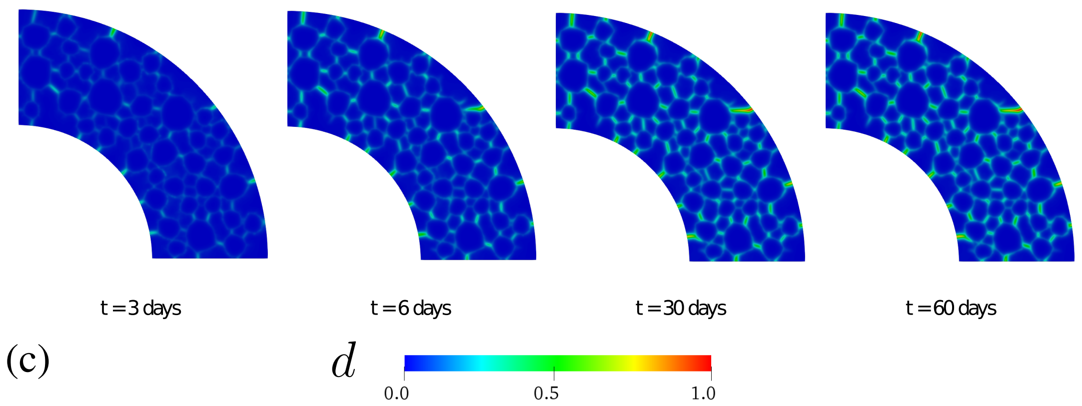

(c)

Figure 5.29: (a) Maximum principal strains, (b) maximum principal stresses and (c) damage contours for crack propagation of the poorly-graded section

analysis given in Figure 5.28 (b).

Comparing the damage patterns of non-segregated sections with various gradings with the segregated section, one can see the phenomenon of cracking initiated on the inside and extending towards the outside is a symptomatic pattern only seen in the segregated section. This confirms that segregation of aggregates and the resulting differential shrinkage is the main contributor to the extensive cracking in the poles, and should be avoided at all costs.

CHAPTER 6

CONCLUSIONS AND OUTLOOK

In this thesis, we investigated cracking in spun-cast poles due to shrinkage. Using the new Phase-Field model for quasi-brittle fracture proposed by Wu [64] and the Finite Element Method to model crack propagation we carried out several numerical simulations to study cracking of pole sections due to shrinkage. To our best knowledge, this is one of the first works on the numerical modeling of differential-shrinkage-induced cracking in spun-cast concrete poles incorporating hardening in the model. The cracking observed in segregated models agrees qualitatively with experimental observations of Dilger et al. [1]. It is seen that the differential shrinkage causes cracking from the inside that propagates radially through the thickness. Also, we studied the effect of aggregate grading on cracking in section without segregation. Simulations with well-graded, gap-graded, and poorly-graded sections displayed no significant cracking in general compared to the segregated section. So, it can be said that the main reason for cracking in the poles is the segregation of aggregates. Also, the difference between linear elastic analysis and crack propagation with aging shows the importance of aging and cracking in redistribution of strains and stresses. It is then insufficient to rely on the results of a simple linear elastic analysis to analyze risk of damaging and zones of stress concentration. The simulations clearly display the competence of the new phase-field model for studying crack propagation in concrete.

Our study was limited to a linear elastic material behavior and prescribed uniform shrinkage strains in mesoscale models. A future study with a coupled diffusion analysis for modeling shrinkage regarding moisture transport through the cracking section would be useful. Also, early-age concrete behaves in a more viscoplastic rather than linear elastic manner, and therefore, a more realistic constitutive model would be of great interest. Moreover, ITZ (Interface Transition Zone) should be taken into account. Also, the effect of reinforcement on cracking of the pole can be studied. The Phase-Field Method for quasi-brittle fracture proposed by Wu [64] is a new model and can be implemented to numerous problems. It can be used in modeling any fracturing problem in concrete and also other quasi-brittle materials, such as asphalt and rock.

REFERENCES

[1] W. H. Dilger, A. Ghali, and S. Krishna Mohan Rao, "Improving the durability and performance of spun-cast concrete poles," *PCI journal*, vol. 41, no. 2, pp. 68–90, 1996.

[2] J. Newman and B. Choo, *Advanced Concrete Technology 2: Concrete Properties*. Elsevier Science, 2003.

[3] R. I. Gilbert and G. Ranzi, *Time-dependent behaviour of concrete structures*. CRC Press, 2010.

[4] P. Monteiro, *Concrete: Microstructure, Properties, and Materials*. McGraw-Hill Publishing, 2006.

[5] Z. Li, *Advanced concrete technology*. John Wiley & Sons, 2011.

[6] W. H. Dilger and S. Krishna Mohan Rao, "High performance concrete mixtures for spun-cast concrete poles," *PCI journal*, vol. 42, pp. 82–97, 1997.

[7] J.-K. Kim and C.-S. Lee, "Prediction of differential drying shrinkage in concrete," *Cement and Concrete Research*, vol. 28, no. 7, pp. 985–994, 1998.

[8] C. de Sa, F. Benboudjema, M. Thiery, and J. Sicard, "Analysis of microcracking induced by differential drying shrinkage," *Cement and Concrete Composites*, vol. 30, no. 10, pp. 947–956, 2008.

[9] A. E. Idiart, C. M. López, and I. Carol, "Modeling of drying shrinkage of concrete specimens at the meso-level," *Materials and structures*, vol. 44, no. 2, pp. 415–435, 2011.

[10] M. Briffaut and F. Benboudjema, "Numerical analysis of cracking induced by drying shrinkage in concrete using a mesoscopic approach: influence of aggregates restraint and skin effect," in *Mechanics and Physics of Creep, Shrinkage, and Durability of Concrete: A Tribute to Zdeňk P. Bažant*, pp. 243–250, 2013.

[11] M. Briffaut, F. Benboudjema, J. M. Torrenti, and G. Nahas, "A thermal active restrained shrinkage ring test to study the early age concrete behaviour of massive structures," *Cement and concrete research*, vol. 41, no. 1, pp. 56–63, 2011.

[12] H. Beushausen and M. Alexander, "Failure mechanisms and tensile relaxation of bonded concrete overlays subjected to differential shrinkage," *Cement and concrete research*, vol. 36, no. 10, pp. 1908–1914, 2006.

[13] L. Ruiz-Ripoll, B. Barragán, S. Moro, and J. Turmo, "Digital imaging methodology for measuring early shrinkage cracking in concrete," *Strain*, vol. 49, no. 3, pp. 267–275, 2013.

[14] V. Korsun, N. Vatin, A. Korsun, and D. Nemova, "Heterogeneous shrinkage of high-strength concrete by the volume of large-size structural elements," in *Applied mechanics and materials*, vol. 723, pp. 445–450, Trans Tech Publications, 2015.

[15] H. Beushausen, "A parameter study on the age at cracking of bonded concrete overlays subjected to restrained shrinkage," *Materials and Structures*, vol. 49, no. 5, pp. 1905–1916, 2016.

[16] S. Tang, S. Wang, T. Ma, C. Tang, C. Bao, X. Huang, and H. Zhang, "Numerical study of shrinkage cracking in concrete and concrete repair systems," *International Journal of Fracture*, vol. 199, no. 2, pp. 229–244, 2016.

[17] V. Dey, R. Kachala, A. Bonakdar, N. Neithalath, and B. Mobasher, "Quantitative 2d restrained shrinkage cracking of cement paste with wollastonite microfibers," *Journal of Materials in Civil Engineering*, vol. 28, no. 9, p. 04016082, 2016.

[18] W. Dong, X. Zhou, and Z. Wu, "A fracture mechanics-based method for prediction of cracking of circular and elliptical concrete rings under restrained shrinkage," *Engineering Fracture Mechanics*, vol. 131, pp. 687–701, 2014.

[19] L. E. Bryne, A. Ansell, and J. Holmgren, "Investigation of restrained shrinkage cracking in partially fixed shotcrete linings," *Tunnelling and Underground Space Technology*, vol. 42, pp. 136–143, 2014.

[20] W. Dong, X. Zhou, Z. Wu, and G. Kastiukas, "Effects of specimen size on assessment of shrinkage cracking of concrete via elliptical rings: Thin vs. thick," *Computers & Structures*, vol. 174, pp. 66–78, 2016.

[21] J. Liu, Z. Zhao, S. Deng, and N. Liang, "A simple method to simulate shrinkage-induced cracking in cement-based composites by lattice-type modeling," *Computational Mechanics*, vol. 43, no. 4, pp. 477–492, 2009.

[22] P. Grassl, H. S. Wong, and N. R. Buenfeld, "Influence of aggregate size and volume fraction on shrinkage induced micro-cracking of concrete and mortar," *Cement and concrete research*, vol. 40, no. 1, pp. 85–93, 2010.

[23] A. Idiart, J. Bisschop, A. Caballero, and P. Lura, "A numerical and experimental study of aggregate-induced shrinkage cracking in cementitious composites," *Cement and Concrete Research*, vol. 42, no. 2, pp. 272–281, 2012.

[24] I. Maruyama and H. Sasano, "Strain and crack distribution in concrete during drying," *Materials and structures*, vol. 47, no. 3, pp. 517–532, 2014.

[25] M. Malbois, A. Darquennes, C. De Sa, and F. Benboudjema, “Experimental study on the effects of aggregates restraint on the delayed behavior of cementitious materials,” in *CONCREEP 10*, pp. 1167–1176, 2015.

[26] K. Shin, Y. Choi, and K. Lee, “Meso-scale numerical investigation of tensile and shrinkage behaviours of concrete,” *Materials Research Innovations*, vol. 19, no. sup1, pp. S1–139, 2015.

[27] E. Lee, S. Park, and Y. Kim, “Drying shrinkage cracking of concrete using dune sand and crushed sand,” *Construction and Building Materials*, vol. 126, pp. 517–526, 2016.

[28] I. Maruyama, H. Sasano, and M. Lin, “Impact of aggregate properties on the development of shrinkage-induced cracking in concrete under restraint conditions,” *Cement and Concrete Research*, vol. 85, pp. 82–101, 2016.

[29] T. Rabczuk, “Computational methods for fracture in brittle and quasi-brittle solids: State-of-the-art review and future perspectives,” *ISRN Applied Mathematics*, 2013.

[30] A. Ingraffea and V. Saouma, “Numerical modelling of discrete crack propagation in reinforced and plain concrete,” *Fracture Mechanics of concrete*, pp. 171–225, 1985.

[31] X.-P. Xu and A. Needleman, “Numerical simulations of fast crack growth in brittle solids,” *Journal of the Mechanics and Physics of Solids*, vol. 42, no. 9, pp. 1397–1434, 1994.

[32] G. T. Camacho and M. Ortiz, “Computational modelling of impact damage in brittle materials,” *International Journal of solids and structures*, vol. 33, no. 20-22, pp. 2899–2938, 1996.

[33] N. Moës, J. Dolbow, and T. Belytschko, “A Finite Element Eethod for crack growth without remeshing,” *International Journal for Numerical Methods in Engineering*, vol. 46, no. 1, pp. 131–150, 1999.

[34] R. Peerlings, R. De Borst, W. Brekelmans, and J. De Ṽree, “Gradient enhanced damage for quasi-brittle materials,” *International Journal for Numerical Methods in Engineering*, vol. 39, no. 19, pp. 3391–3403, 1996. cited By 485.

[35] G. Pijaudier-Cabot and Z. P. Bazant, “Nonlocal damage theory,” *Journal of Engineering Mechanics*, vol. 113, no. 10, pp. 1512–1533, 1987.

[36] G. Francfort and J.-J. Marigo, “Revisiting brittle fracture as an energy minimization problem,” *Journal of the Mechanics and Physics of Solids*, vol. 46, no. 8, pp. 1319–1342, 1998.

[37] A. A. Griffith, “The phenomena of rupture and flow in solids,” *Philosophical transactions of the royal society of london. Series A, containing papers of a mathematical or physical character*, vol. 221, pp. 163–198, 1921.

[38] T. Belytschko, Y. Lu, and L. Gu, “Crack propagation by element-free galerkin methods,” *Engineering Fracture Mechanics*, vol. 51, no. 2, pp. 295–315, 1995.

[39] T. Belytschko and M. Tabbara, “Dynamic fracture using element-free galerkin methods,” *International Journal for Numerical Methods in Engineering*, vol. 39, no. 6, pp. 923–938, 1996.

[40] M. Fleming, Y. Chu, B. Moran, T. Belytschko, Y. Lu, and L. Gu, “Enriched element-free galerkin methods for crack tip fields,” *International journal for numerical methods in engineering*, vol. 40, no. 8, pp. 1483–1504, 1997.

[41] B. Rao and S. Rahman, “An efficient meshless method for fracture analysis of cracks,” *Computational mechanics*, vol. 26, no. 4, pp. 398–408, 2000.

[42] B. N. Rao and S. Rahman, “Mesh-Free Simulation in Elastic-Plastic Fracture Mechanics,” in *New and Emerging Computational Methods: Applications to Fracture, Damage, and Reliability*, vol. 2002, pp. 103–123, ASME, 2002.

[43] B. Rao and S. Rahman, “An enriched meshless method for non-linear fracture mechanics,” *International Journal for Numerical Methods in Engineering*, vol. 59, no. 2, pp. 197–223, 2004.

[44] R. Brighenti, “Application of the element-free galerkin meshless method to 3-d fracture mechanics problems,” *Engineering Fracture Mechanics*, vol. 72, no. 18, pp. 2808–2820, 2005.

[45] T. Rabczuk, S. Bordas, and G. Zi, “A three-dimensional meshfree method for continuous multiple-crack initiation, propagation and junction in statics and dynamics,” *Computational Mechanics*, vol. 40, no. 3, pp. 473–495, 2007.

[46] H. Hosseini-Toudeshky and M. Musivand-Arzanfudi, “Fracture analysis using parametric meshless galerkin method,” *Fatigue & Fracture of Engineering Materials & Structures*, vol. 31, no. 1, pp. 49–66, 2008.

[47] N. Liu, X. He, S. Li, and G. Wang, “Meshless simulation of brittle fracture,” *Computer Animation and Virtual Worlds*, vol. 22, no. 2-3, pp. 115–124, 2011.

[48] N. Sagaresan, “Modeling fracture of concrete with a simplified meshless discrete crack method,” *KSCE Journal of Civil Engineering*, vol. 16, no. 3, pp. 417–425, 2012.

[49] S.-W. Yang, P. R. Budarapu, D. R. Mahapatra, S. P. Bordas, G. Zi, and T. Rabczuk, “A meshless adaptive multiscale method for fracture,” *Computational Materials Science*, vol. 96, pp. 382–395, 2015.

[50] A. Karma, D. Kessler, and H. Levine, "Phase-Field Model of mode III dynamic fracture," *Physical Review Letters*, vol. 87, no. 4, p. 045501, 2001.

[51] C. Kuhn and R. Müller, "A continuum Phase Field Model for fracture," *Engineering Fracture Mechanics*, vol. 77, no. 18, pp. 3625–3634, 2010.

[52] C. Miehe, F. Welschinger, and M. Hofacker, "Thermodynamically consistent Phase-Field models of fracture: Variational principles and multi-field FE implementations," *International Journal for Numerical Methods in Engineering*, vol. 83, no. 10, pp. 1273–1311, 2010.

[53] C. Miehe, M. Hofacker, and F. Welschinger, "A Phase Field Model for rate-independent crack propagation: Robust algorithmic implementation based on operator splits," *Computer Methods in Applied Mechanics and Engineering*, vol. 199, no. 45–48, pp. 2765—-2778, 2010.

[54] C. Kuhn and R. Müller, "A new Finite Element technique for a Phase Field Model of brittle fracture," *Journal of Theoretical and Applied Mechanics*, vol. 49, no. 4, pp. 1115–1133, 2011.

[55] M. Borden, C. Verhoosel, M. Scott, T. Hughes, and C. Landis, "A Phase-Field description of dynamic brittle fracture," *Computer Methods in Applied Mechanics and Engineering*, vol. 217–220, pp. 77–95, 2012.

[56] M. Hofacker and M. C., "Continuum Phase Field modeling of dynamic fracture: variational principles and staggered fe implementation," *International Journal of Fracture*, vol. 178, no. 1–2, pp. 113–129, 2012.

[57] C. Verhoosel and R. de Borst, "A Phase-Field Model for cohesive fracture," *International Journal for Numerical Methods in Engineering*, vol. 96, no. 1, pp. 43–62, 2013.

[58] J. Vignollet, S. May, and C. de Bors, R.tand. Verhoose, "Phase-Field Models for brittle and cohesive fracture," *Meccanica*, vol. 49, pp. 2587—-2601, 2014.

[59] M. Borden, T. Hughes, C. Landis, and C. Verhoosel, "A higher-order Phase-Field Model for brittle fracture: Formulation and analysis within the isogeometric analysis framework," *Computer Methods in Applied Mechanics and Engineering*, vol. 273, pp. 100—-118, 2014.

[60] T. Tanfener, "Finite Element Analyses of differential shrinkage-induced cracking in centrifugally cast concrete poles," Master's thesis, Middle East Technical University, Turkey, 2012.

[61] I. Völgyi, G. Farkas, and S. Nehme, "Concrete strength tendency in the wall of cylindrical spun-cast concrete elements," *Periodica Polytechnica Civil Engineering*, vol. 54, no. 1, pp. 23–30, 2010.

[62] G. R. Irwin, “Fracture dynamics,” *Fracturing of metals*, vol. 152, 1948.

[63] E. Orowan, “Fracture and strength of solids,” *Reports on progress in physics*, vol. 12, no. 1, p. 185, 1949.

[64] J.-Y. Wu, “A unified Phase-Field theory for the mechanics of damage and quasi-brittle failure,” *Journal of the Mechanics and Physics of Solids*, vol. 103, pp. 72–99, 2017.

[65] T. Nguyen, J. Yvonnet, Q.-Z. Zhu, M. Bornert, and C. Chateau, “A Phase Field Method to simulate crack nucleation and propagation in strongly heterogeneous materials from direct imaging of their microstructure,” *Engineering Fracture Mechanics*, vol. 139, pp. 18 – 39, 2015.

[66] C. Miehe, M. Hofacker, L.-M. Schaenzel, and F. Aldakheel, “Phase Field modeling of fracture in multi-physics problems. part ii. coupled brittle-to-ductile failure criteria and crack propagation in thermo-elastic–plastic solids,” *Computer Methods in Applied Mechanics and Engineering*, vol. 294, pp. 486–522, 2015.

[67] H. Cornelissen, D. Hordijk, and H. Reinhardt, “Experimental determination of crack softening characteristics of normalweight and lightweight concrete,” *Heron*, vol. 31, no. 2, pp. 45–56, 1986.

[68] R. L. Taylor, “FEAP - Finite Element Analysis Program,” 2014.

[69] C. Geuzaine and J.-F. Remacle, “Gmsh: A 3-d finite element mesh generator with built-in pre-and post-processing facilities,” *International journal for numerical methods in engineering*, vol. 79, no. 11, pp. 1309–1331, 2009.

[70] H. I. Andiç, “Coupled thermomechanical analysis of concrete hardening,” Master’s thesis, Middle East Technical Uuniversity, 2015.

[71] C. Miehe, “Computation of isotropic tensor functions,” *Communications in Numerical Methods in Engineering*, vol. 9, pp. 889–896, nov 1993.

[72] C. Miehe and M. Lambrecht, “Algorithms for computation of stresses and elasticity moduli in terms of Seth-Hill’s family of generalized strain tensors,” *Communications in Numerical Methods in Engineering*, vol. 17, pp. 337–353, apr 2001.

[73] G. Wells and L. Sluys, “A new method for modelling cohesive cracks using Finite Elements,” *International Journal for Numerical Methods in Engineering*, vol. 50, no. 12, pp. 2667–2682, 2001.